Small scale and large scale specimen fatigue resistance similarity of welded joints in steel marine structures

Weld modeling aspects

Marine technology

Zhiwei Xing

Delft University of Technology

TU Delft

Small scale and large scale specimen fatigue resistance similarity of welded joints in steel marine structures

Weld modeling aspects

by

Zhiwei Xing

Student Name	Student Number
Zhiwei Xing	5519977

Chair:	Dr. ir. J.H. den Besten, TU Delft
Supervisor:	Dr. ir. J.H. den Besten, TU Delft
Other committee:	Dr. A. (Apostolos) Grammatikopoulos
	Ir. R.L.G. (Ruben) Slange
Project Duration:	July, 2023 - October, 2024
Faculty:	Faculty of 3ME, Delft

Cover:	Typical FPSO from SBM[34]
Style:	TU Delft Report Style, with modifications by Daan Zwaneveld

TU Delft

Small scale and large scale specimen fatigue resistance similarity of welded joints in steel marine structures

Weld modeling aspects

by

Zhiwei Xing

This thesis (MT.24/45.011.M) is classified as confidential in accordance with the general conditions for projects performed by the TU Delft. Monday October 28, 2024 at 13:00 (CET).

Student number:	5519977
Chair:	Dr. ir. J.H. den Besten, TU Delft
Supervisor:	Dr. ir. J.H. den Besten, TU Delft
Other committee:	Dr. A. (Apostolos) Grammatikopoulos
	Ir. R.L.G. (Ruben) Slange
Project Duration:	July, 2023 - October, 2024
Faculty:	Faculty of 3ME, Delft

TU Delft

Preface

This thesis marks the end of my journey towards earning my Master's degree in TU Delft Marine Technology focusing on marine steel structures fatigue analysis, and also indicates the outcome in 15 months. This road to study was far from smooth sailing. Courses "Fatigue strength of Marine Structures" from Dr.J.H.den.Besten and "Ultimate Strength of Marine Structures" from Dr.C.L.Walters ignited my interest in structural engineering and finite element method. However, lack of knowledge background in mechanics cost me more time and energy in the research process to complement foundations. Fortunately, some people helped me when I was struggling and frustrated, which allowed my research to move forward and to have a full understanding of the topic. Here I would like to express appreciation to them who guided and supported me.

First, I would like to thank Dr.J.H.den Besten, the chair of the committee and supervisor of my project. He provided crucial suggestions at the beginning of each stage and offered detailed feedback at the end. Meanwhile, he held the post of my daily supervisor at the outset. He consistently provided timely and detailed responses to my questions, even when some were basic or repetitive. I understand how exceptionally valuable this was, especially considering the challenges of being a busy professor and a father caring for a baby. Once, my poor research plan and slow progress caused him concern. He asked whether I was enjoying the thesis work and feeling satisfied with it. At that time, my answer was no, but now I can confidently say that this has been one of the most meaningful things I have ever done, and I am truly satisfied with it.

I would like to thank Mr.Ruben Slange, my friend, and also another committee member. He joined my project in the final three months, substituting from Henk den Besten as my daily supervisor. He assisted me in reviewing the simulation results and modifying the relevant code. Ruben's involvement also provided a lower threshold for asking questions for me, allowed him to share his expertise and experience, and provided his feedback. His participation resolved many long-standing academic issues that had troubled me and was crucial for the progress of my research.

I would like to thank Mr.Shangru Liu, my friend, and also a structural engineer. He guided my FEM modeling with his industry experience, particularly in developing solid models within ANSYS Workbench. While solid modeling and analysis may seem straightforward, unexpected minor issues often arise during implementation. His assistance transformed me from a greenhand who often stared at a simple FEM problem into someone capable of independently resolving almost all related issues in my thesis work.

I would like to thank Mr.Xinmiao Liu, my friend, and also a PhD student at TU Eindhoven. He provided significant assistance regarding fatigue analysis approaches. He patiently helped me reinforce my understanding of the fundamentals of fatigue analysis methods and other mechanical principles. He was always willing to answer my spontaneous questions and engage in discussions about his understanding, even when many of these questions were often meaningless.

Finally, I would like to thank my father and my mother. Despite residing on the opposite side of the Eurasian continent, their mental support helped me overcome countless difficulties. As an international student, my deferred graduation has put a lot of financial burden on them, but they have never put any pressure on me and just quietly supported me behind the scenes. Apart from that, I would like to thank all of my friends for their encourage and supports.

Zhiwei Xing
Delft, October 2024

Abstract

In marine structures, fatigue is typically the dominant limit state. The fatigue resistance of welded joints in steel marine structures is a critical aspect of ensuring the structural integrity and safety of the components. To determine the structural response, finite element method is necessary to evaluate structural stress. For thin-wall structures, shell element model is usually preferred to solid element model, because the former can save time in calculations. In order to study the effect of weld modeling in shell model, the structural stress levels of the shell model in both the as-welded and unwelded cases are investigated respectively, using the solid element model results for reference purposes. The first chapter is the introduction and the second chapter is literature survey of state-of-the-art research. Chapter 3 and chapter 4 focus on the structural stress estimation with respect to frame-stiffener structure and stiffener-plate structure. The traction forces based procedure is clarified and applied to evaluate HS structural stress. In consequence, the preliminary conclusion on the influence of weld modeling on the structural stress of the shell model is obtained.

Apart from that, fatigue resistance data for arc-welded joints are typically derived from small-scale specimens. However, structural aspects can affect fatigue resistance characteristics. Therefore, to validate whether the fatigue resistance observed in small-scale specimens accurately represents that of full-scale structure, similarity research is necessary. In Chapter 5, the effective notch stress of large-scale specimens is evaluated. Fatigue failure criteria are discussed to derive the appropriate lifetime. Finally, the LSS fatigue resistance data evaluated by the effective notch concept are substituted into SSS fatigue resistance scatter band, to validate the similarity between SSS and LSS.

Contents

Nomenclature

Abbreviations

Abbreviation	Definition
BB	Bi-linear Basquin
BC	Boundary condition
BRFL	Bi-linear random fatigue limit
DOF	Degrees of freedom
DS	Double sided
ENS	Effective notch stress
ENSC	Effective notch stress concept
ES	Element size
FEA	Finite element analysis
FEM	Finite element method
FPSO	Floating production storage and offloading
FSM	Frame-stiffener model
GRFL	Generalized random fatigue limit
HCF	High cycle fatigue
HP	Holland profile
HS	Hot spot
HSS	Hot spot stress
IIW	International Institute of Weld
LSS	Large scale specimen
MCF	Medium cycle fatigue
NSC	Nominal stress concept
ORFL	Odinary random fatigue limit
PDE	Partial differential equation
PWHT	Post weld heat treatment
SCF	Stress concentration factor
SOF	Stiffener on frame
SPM	Stiffener-plate model
SS	Single sided
SSS	Small scale specimen

Symbols

Symbol	Definition
A	Cross-section area
C_{bm}	Line force induced weld load carrying stress coefficient
C_{bb}	Bending moment induced weld load carrying stress coefficient
C_{bw}	Weld load carrying stress coefficient
F	Applied load
F_i	Nodal force
F_x	X-direction Nodal force in Global coordinate system
F_y	Y-direction Nodal force in Global coordinate system
F'_x	X-direction Nodal force in local coordinate system
F'_y	Y-direction Nodal force in local coordinate system
f_i	Line force
f_t	Line force scalar
$f(r/t_p)$	Normal force distribution
f'	Line force in local coordinate system
h_w	Weld height
I	Moment of inertia
K_f	Stress concentration factor
L_1	Length between virtual node and HS
L	Reference length
l_i	Element edge length
l_w	Weld leg length
M	Bending moment
m_{bb}	Bending moment induced weld load carrying bending moment
m_{bm}	Line force induced weld load carrying bending moment
m'	Moment in local coordinate system
n_{load}	Number of nodes in load line
r_s	Stress ratio
r_{lr}	Response stress ratio
S_e	ENS range
$S_{e,eff}$	Improved ENS range
t	Thickness
t_p	Plate thickness
t'_p	Virtual thickness
y	Distance from centroid to the point considered
z_i	Distance between reference nodes and HS

α	Notch angle
β	Stress angle
γ	Load response ratio parameter
δ	Element width
$\Delta\sigma_s$	Structural stress range
$\lambda_{a,s}$	first eigenvalue of (anti-)symmetry part
$\mu_{a,s}$	stress amplitude of (anti-)symmetry part
$\rho*$	Reference micro- and meso-structural length (or distance)
σ_{nom}	Nominal stress
σ_{nommod}	Modified nominal stress

Symbol	Definition
σ_b	Bending stress
σ_m	Memberane stress
σ_{nlp}	Nonlinear peak stress
σ_s	Structural stress
σ_{hs}	Hot spot stress
σ_x	Nominal stress in x direction
σ_e	Effective notch stress
σ_e	Effective notch stress
$\sigma_n(r/t_p)$	Weld notch stress distribution
$\tau_(xy)$	Shear stress in x and y direction
$\chi_{a,s}$	first eigenvalue coefficient of (anti-)symmetry part

1

Introduction

Fatigue failure represents a persistent concern in maritime engineering, characterized by the crack growing of materials subjected to cyclic loading and environmental stressors. From ship hulls to offshore wind turbines, marine structures are constantly exposed to dynamic forces that can compromise their structural reliability over time. Consider the challenges posed by the load forces of waves, currents, and static pressure—understanding the fatigue behavior of materials in marine environments is crucial for maintaining operational efficiency and preventing catastrophic failures.

1.1. Fatigue fundamental

Fatigue in mechanics refers to the failure of material or structures caused by cyclic loads, typically below the material's ultimate tensile strength(normally even under yield strength). Therefore elastic stress is usually considered in fatigue strength assessment[39]. In marine structures, the loads are mainly caused by waves and winds. The magnitude of the stress range plays an important role in fatigue.

In a specimen subjected to a cyclic load, a fatigue crack nucleus can be initiated on a microscopically small scale, followed by crack growth to a macroscopic size, and finally to specimen failure in the last cycle of the fatigue life[49]. Fatigue failure typically occurs three period: crack initiation period, crack propagation period, and final fracture. The general description of fatigue was given in Eurocode:

1. *"The process of initiation and propagation of cracks through a structural part due to action of fluctuating stress."[14]*

The process begins with the formation of small cracks on the material's surface or at stress concentrators, such as notches, holes, or inclusions. These cracks may form due to cyclic slip, extrusion, and intrusion of material grains, often exacerbated by factors like surface roughness, corrosion, or pre-existing defects. The second period is crack propagation period. Once initiated, the crack propagates with each loading cycle[58]. The propagation is influenced by the material's microstructure, loading conditions, and environmental factors.

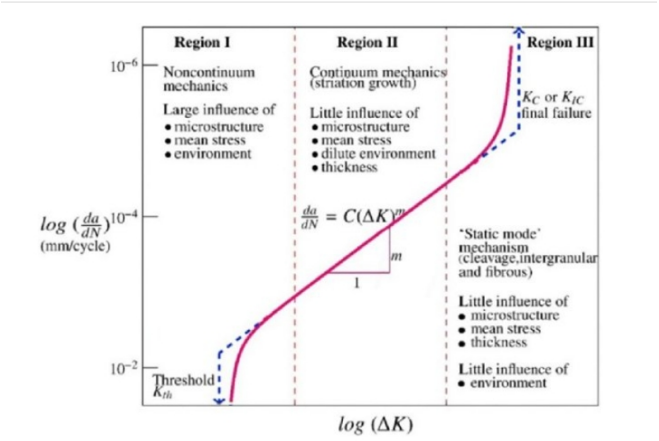

Figure 1.1: Fatigue crack growth curve[23]

After the crack size grows to a critical size, as soon as the crossing section area cannot support the applied load, the fatigue fracture will rapidly happen. Figure of crack growth curve 1.1 illustrates the periods and processes of fatigue.

1.1.1. Fatigue

The S-N plot describes relationship between stress range (so-called ”S”) and number of loading cycles (so-called ”N”), which Augustus Wöhler proposed in the 19th Century. The relation is displayed in the Cartesian coordinate system, where the N is in x-axis and S is in y-axis. The fatigue test results are presented in the form of discrete points in the S-N plot, which indicates that the specimen becomes failure after N cycles under the stress range corresponding to this point. The SN curve is fitted based on these discrete points as a smooth curve. A typical S-N curve is given as Figure 1.2

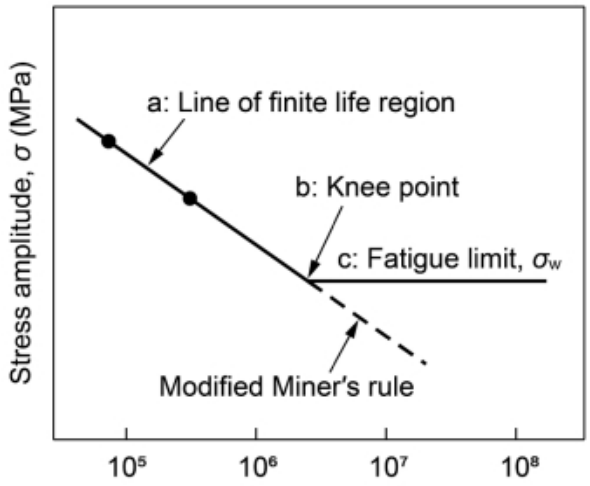

Figure 1.2: Typical S-N curve description[32]

At a constant amplitude, fatigue testing continues until the specimen failure. The number of loading cycles would be recorded and pointed in S-N coordinate. Depending on the range of N and materials, the fatigue could be divided as high cycle fatigue(HCF), mid cycle fatigue(MCF), and low cycle fatigue(LCF). LCF correspond to 10^2-10^4 number of cycles, MCF correspond to 10^4-$5 * 10^6$, and HCF correspond to $5 * 10^6$-10^9[44]. LCF mainly aims high stress ranges and low number of cycles, and

HCF aims low stress ranges and high number of cycles. In maritime and offshore industries, structures are generally designed for several decades, thus MCF and HCF range often needs to be focused on research.

For most of structures, there would be a horizontal curve parallel to x-axis which appears in the end of S-N curve. The stress range of this horizontal curve was called fatigue limit or fatigue endurance. Theoretically, the structure can endure infinite number of load cycles and will never failure when the stress range is under fatigue endurance. The fatigue limit is a theoretical concept that combines material properties and structural geometry. It indicates that there will be no fatigue when the stress becomes so low that the structure yields locally. Barthias et al.[4] and Sosino[53] both have conclusions that a real fatigue limit could only be achieved in absence of microstructural inhomogeneities or when there is no interference of a corrosive medium. However, it is impossible to implement in realistic practice.

1.1.2. Crack modes

Marine and offshore structures, such as ships, Floating production storage and offloading(FPSO), wind turbines, and underwater pipelines, are subjected to a wide range of loads due to their exposure to harsh marine environments. The primary causes of these loads can be environmental factors. Wave loads, wind loads, and hydrostatic pressure can cause stresses within the offshore structures. These natural phenomena are dynamic, thus the applicability of constant amplitude loading in simulation is limited.

The load mode that can induce crack could be categorized into 3, as Figure 1.3. The three load modes involve different crack surface displacements. Mode 1 is the opening or tensile mode, the crack faces are pulled apart; mode 2 is sliding or in-plane shear , the crack surfaces slide over each other; mode 3 is tearing or anti-plane shear, the crack surfaces move parallel to the leading edge of the crack and relative to each other. Mode 1 appears under bending stress and normal stress, which influence most to maritime and offshore structures. The first reason is the manufacturing method for stiffened panels. The hierarchy of the members leads to orthotropy, which results in normal stress. Besides, in thin wall structure normal stress is dominant. Mode 2 shows in-plane shear. As mentioned earlier, normal and bending stresses dominate in thin-walled structures,thus mode 2 is almost not relevant to marine and offshore structures. Out-of-plane shear is shown in mode 3, which occurs in some applications, for instance, torque modes of rotating blades in offshore wind turbines.

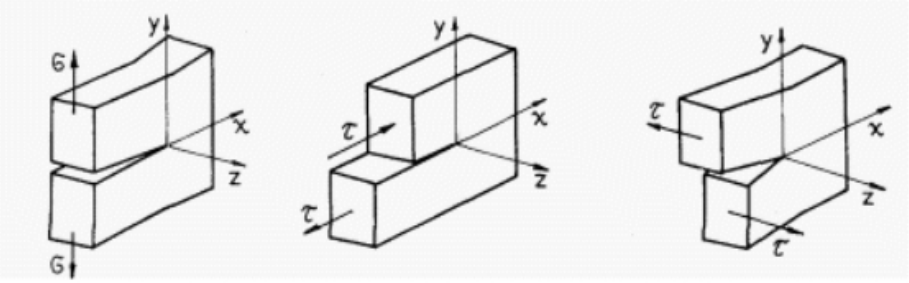

Figure 1.3: Three crack modes[30]

1.1.3. Hot spot types

The hot spot refers to a specific location within a structure where the stress concentrations are high enough to reduce the fatigue life of the material significantly. These spots are critical in fatigue analysis because they are potential initiation points for fatigue cracks. The hot spot in macroscopic is divided into three types under load mode 1, as Figure 1.4. The stress calculation and crack propagation vary from different hot spot types. For hot spot type A, the notch appears at weld toe end and perpendicular to the weld seam; for hot spot type B, the notch appears at the weld toe end and parallel to the weld seam; for hot spot type C, notches appear at the joint cross-section along the weld seam.

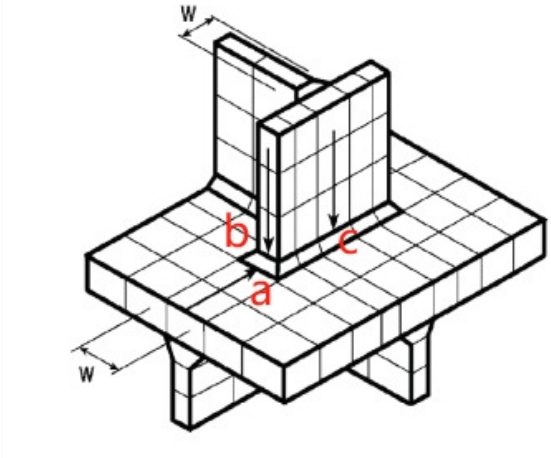

Figure 1.4: Hot spot types[27]

1.2. Problem statement

Marine structures primarily consist of assemblies of structural members, either in planar configurations such as stiffened panels or tubular configurations like trusses and frames. To accurately determine the structural response of these assemblies, finite element modeling is often necessary. In fatigue limit state assessments, particular attention is given to the typically arc-welded joints, due to high stress concentration and initiatial defect. This requires accurate estimates of far field stress. For thin-wall structures, the shell element model usually provides accurate approximation and requires less time for computing compare to solid element model. It is generally preferred to use shell or plate elements over solid elements for this modeling[7]. However, a critical question arises: should the weld be included in the model to obtain accurate far field stress estimates? If so, what is the appropriate modeling approach?

Fatigue resistance data for arc-welded joints are typically derived from small-scale specimen testing, which involves only the actual joint. However, in full-scale structures, structural aspects such as the scale effect and variations in welding-induced residual stress can affect fatigue resistance characteristics. This discrepancy raises concerns about whether the fatigue resistance observed in small-scale specimens accurately represents that of full-scale structures. Conducting fatigue tests on large-scale specimens, which incorporate these structural aspects, may provide a more accurate representation of the fatigue resistance in actual conditions.

1.3. Motivation

Due to the technical challenges and costs associated with full-scale testing of engineering components, laboratory experiments on smooth and small specimens are commonly conducted to determine basic fatigue properties. These data are then used for assessing the fatigue performance of actual structures. Consequently, it is essential to study the size effect in steel fatigue and to establish a reliable method for extrapolating data from small specimens to predict the behavior of full-scale components[54].

1.4. Research objective

This research will be based on the results of FEM simulations. The stress range will be calculated from the fem results, and the number of load cycles will be referred to the original LSS literature.

The first objective is to investigate if and how weld modeling in shell model is required in order to obtain accurate far field stress estimates for arc-welded joints in steel marine structures, in stiffened panels configuration. The solid model including the weld joint will be built as a real case to verify the accuracy of the shell model weld modeling. The second objective is to investigate if large scale specimen fatigue

test results, involving stiffened panel configuration, fit the small scale data scatter band for arc-welded joints in steel marine structures, adopting the effective notch stress concept[44].

1.5. Scope

The research will be limited to the typical planar large scale structures with fillet welds. The investigation will be limited to mode type 1 loading, at ambient conditions. Besides, in this research the load amplitude will be considered as constant, and are simplified to point load or line load. The fatigue tests data of large scale specimens will be compared to small scale specimen data collected by Qin[44].

1.6. Outline

This literature study aims to investigate relevant aspects of later research. Section 2.1 presents different kinds of fatigue damage criteria; section 2.2 investigates the finite element analysis and different finite element types; section 2.3 introduces two kinds of weld model; section 2.4 presents the detail of planar and tubular structure details; section 2.5 discuss the possible that influence similarity between large scale specimens and small scale specimens.

Chapter 3.5 investigate the frame-stiffener model, including FEM modeling and HS structural stress range calculating by using traction forces based procedure. The results are compared between as-welded shell model and unwelded shell model; as-weled shell model and solid model. Chapter 4 investigate similar studies as chapter 3.5 for SPM. Apart from that, two kinds weld shape modeling are also investigated(with and without boxing weld end).

In chapter 5 the effective notch stress concept is developed. The LSS fatigue resistance data include lifetime and ENS are substituted into SSS scatter band. Chapter 6 includes the conclusion and recommandation for further research.

2

Literature study

2.1. Fatigue assessment concepts

The stress range around weld toes and roots can be used to determine fatigue resistance and fatigue life according to the S-N curve, which is crucial for fatigue analysis. S-N curve is the method that describes the relation between the number of load cycles to failure and stress range. It was introduced in chapter 1.1.1. Currently, three main fatigue assessment approaches are adopted to analyze and calculate stress range, which are nominal stress concept, hot spot stress concept, and effective notch stress concept. In Eurocode 3 the nominal stress concept and hot spot stress concept are introduced[8].

The nominal stress concept(NSC) is a fundamental approach based on the assumption of evenly stress distribution over a cross-section area, ignoring local stress concentration and geometric irregularities. When the geometry becomes complex, the hot spot stress concept should be used[41]. Another approach for fatigue assessment is the effective notch stress concept. Effective notch stress is the total stress at the root of a notch, calculated under the assumption of linear elastic material behavior. To account for variations in weld shape parameters and the non-linear material behavior at the notch root, the actual weld contour is replaced by an effective one. The detailed introduction of the effective notch stress concept can be found in International Institute of Welding[21].

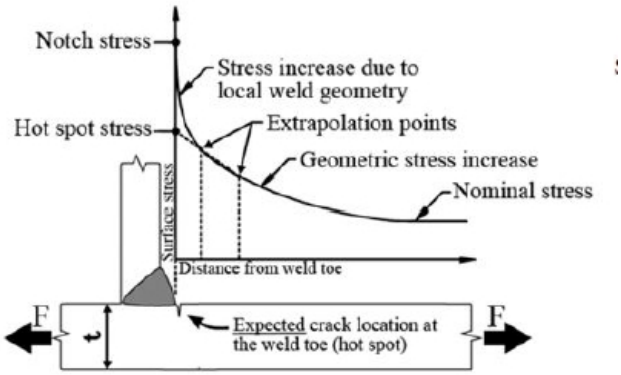

Figure 2.1: Stress distribution round weld toe for different assessment methods[2]

Figure 2.1. shows the stress distribution around the weld toe. Depending on different assessment approaches, each method considers different factors in the design stress. The shape and geometry of the welds are generally considered either in the calculation of stress and S-N curve designing.

2.1.1. Nominal stress

The nominal stress approach is the most traditional method for predicting the fatigue life of a structural component[25]. However, this method is sometimes very difficult to apply in real spot-welded structures because determining the nominal stress in complex structures can be challenging. Additionally, this approach does not account for local stress concentrations caused by the spot weld geometry and circumferential notches. While the nominal stress approach allows for simple calculations, it only offers the least accuracy.

According to elastic theory, all stress concentration effects should be excluded in the calculation of stress in the parent material or in weld adjacent to the potential crack location. The nominal stress described in this section can be categorized as direct stress, shear stress, principal stress, or equivalent stress[14]. Equivalent stress is here used in elastical case. The nominal stress σ_{nom} is calculated using the basic formula[36]:

$$\sigma_{nom} = \frac{F}{A} + \frac{M}{I} * y \tag{2.1}$$

Where F is the applied load; A is the cross-section area of the component; M is the bending moment; I is moment of inertia of the cross-section and y is distance from centroid to the point considered. This concept was built on the basic of a stress parameter criterion, it is a global approach using nominal stress range. This means that each component has a specific fatigue resistance curve. The details and nominal stress range for common structure are described in Eurocode[14], European Standard[33] and IIW[21]. This concept is typically employed during the initial design phase to provide a rapid estimate of stress levels. Additionally, it is sometimes used in material testing to characterize the fundamental strength properties of materials. The nominal stress concept has strong limitations. It is not reliable for predict ng fatigue life and failure in components with complex geometries or loading conditions, and it is impossible to capture size effect[24]. Figure 2.2 shows the MCF-HCF fatigue test scatter band based on nominal stress concerning different different weld joints in steel structures[44].

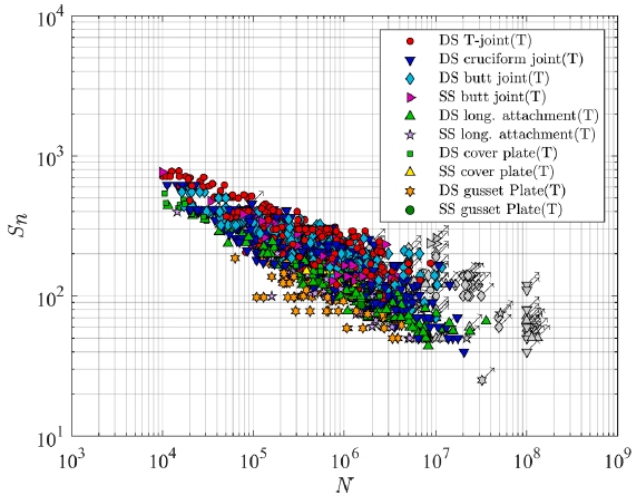

Figure 2.2: Nominal stress-based MCF-HCF fatigue resistance data[44]

The modified nominal stress concept improves upon the traditional nominal stress approach by incorporating factors that account for local effects and stress concentrations. The nominal stress is multiplied by an appropriate stress concentration factor K_f[14] to accommodate geometric discontinuities, eccentricities, and misalignments[39] that are not accounted for in the traditional nominal stress concept of specific constructional details. In general, the higher value of the SCF means that higher local stress at that geometric discontinuity than the nominal stress, which is more possible result in fatigue failure. When the SCF becomes infinite, it means that the local stresses will reach infinity. This usually occurs in theoretical sharp cracks or sharp discontinuities without fillets.

$$\sigma_{nom,mod} = \sigma_{nom} * K_f \tag{2.2}$$

2.1.2. Hot spot structural stress

The hot spot stress(HSS) concept is the most common and well-accepted in the maritime and offshore industry because it considers the stress concentration due to the geometric shape[26]. This is because the predictive fatigue life assessed using the HSS method is generally lower than the real case, which means that the result from the HSS concept is safe[63]. The hot spot stress is defined as the structural stress at the weld toe, which is determined by extrapolating stress values at specific distances from the weld toe, based on finite element analysis[35]. This approach focuses on the assessment of stress at the expected fatigue crack initiation area, often referred to as "Hot Spots". In Eurocode, the hot spot stress concept was introduced. However, there is no further explanations. The relative recommendations for the experiment and finite element method(FEM) were described by IIW[35]. This article only discusses the results based on FEM simulations, the latter will be focused. This approach is only applicable at the weld toe.

The weld toe always leads to the notch, which means nonlinear stress distribution in the direction of through plate thickness. The stress is contributed by bending stress(σ_b), membrane stress(σ_m), and nonlinear peak stress(σ_{nlp}). Figure 2.3 illustrates the contribution of stress near the hot spot. HSS concept is the approach that aims to exclude the nonlinear peak stress, thus the result of structural stress should only contain σ_b and σ_m.

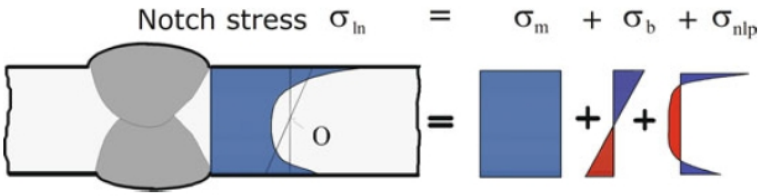

Figure 2.3: Hot spot structural stress distribution[35]

Surface stress extrapolation method The structural hot spot stress can be determined by extrapolating the stress values at reference points to the weld toe under consideration. In this paragraph, surface extrapolation method will be introduced. Linear elastic material behaviour are assumed generally, due to most design code only permit localized yielding[21]. The element size are determined by the reference points selected for stress evaluation in the surface extrapolation method. In the post process of finite element analysis(FEA), the first node near the hot spot should be selected as the reference point, which means the element size should be equal to the length between hot spot and the first reference point[21]. The further description of the regulation for element size in FEA will be introduced in Section 2.2.

The surface stress extrapolation method considers the stress distribution along the side surface of a plate near the weld toe. The reference points for this surface stress extrapolation are positioned at specific distances from the weld toe. The position of the reference point should be determined by specific distances, which the recommendation is given by IIW[21]. By using electric resistance strain gauges the stress is measured based on strain. The nonlinear part should be excluded in the extrapolation method. From Figure 2.4 it is obvious to see that the stress distribution along the direction vertical to plate thickness becomes linear from 0.4t away from the weld toe. In Niemi's research[37] the extrapolation points are defined as 0.4t and 1.0t away from weld toe for hot spot type A and C, where t is the thickness of the plate. When it comes to finite element analysis, 0.4 and 1.0t away from weld toe are recommended for fine mesh, 0.5t and 1.5t away from weld toe are recommended for coarse mesh. The extrapolation points should all be in the linear part, which means located far away from the area influenced by weld geometry, thus excluding the notch stress caused by the weld.

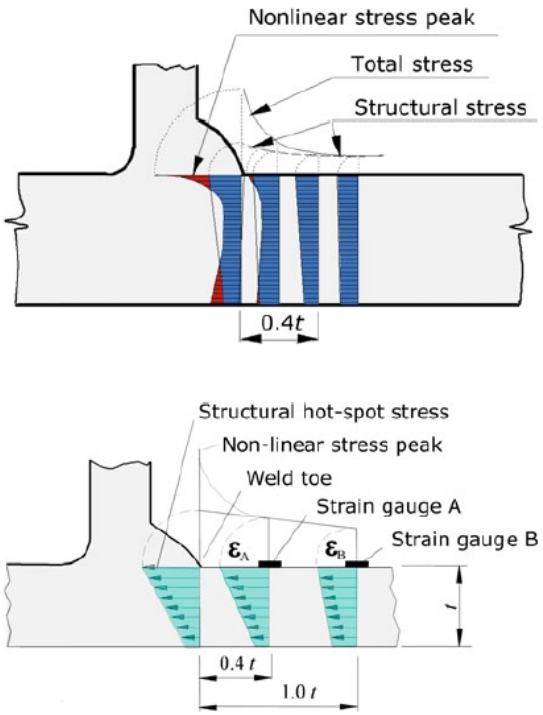

Figure 2.4: Linear extrapolation[37]

Compared to hot spot type A, the position of the extrapolation points for hot spot type B is independent from the thickness of the plate. This is because linear extrapolation is not applicable when the nonlinear structural stress increases significantly towards weld toe. Apart from that, linear extrapolation is also not applicable for the condition of the thick-wall structure and sharp load change[39]. For fine meshed hot spot type B, the position of extrapolate points is determined by quadratic extrapolation to the weld toe, which is 4mm, 8mm, and 12mm away from the weld toe. For coarse mesh condition, the distances are recommended as 5mm and 15mm.

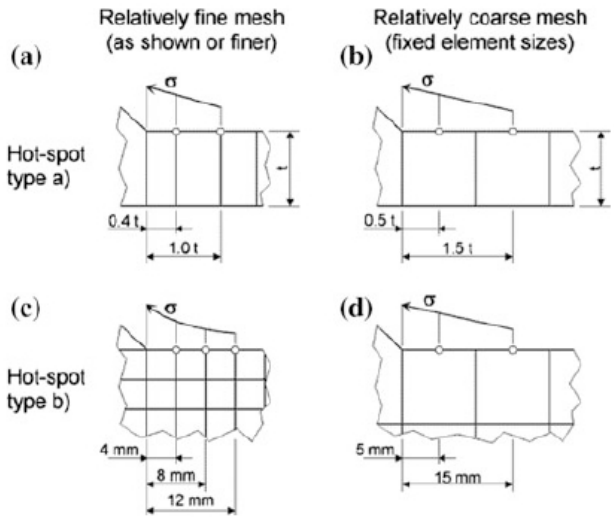

Figure 2.5: Reference points[21]

The specific calculation are as follow[21]:

- For fine mesh hot spot type A, using linear extrapolation.

$$\sigma_{hs} = 1.67 * \sigma_{0.4*t} - 0.67 * \sigma_{1.0*t} \tag{2.3}$$

- For fine mesh hot spot type A, using quadratic extrapolation.(for cases of pronounced non-linear structural stress increase towards the hot spot, at sharp changes of direction of the applied force, or for thick-walled structures.)

$$\sigma_{hs} = 2.52 * \sigma_{0.4*t} - 2.24 * \sigma_{0.9*t} + 0.72 * \sigma_{1.4*t} \tag{2.4}$$

- For coarse mesh hot spot type A, the extrapolation points are located at 0.5t and 1.5t, using linear extrapolation.

$$\sigma_{hs} = 1.5 * \sigma_{0.5*t} - 0.5 * \sigma_{1.5*t} \tag{2.5}$$

- Fine mesh for hot spot type B with element length of not more than 4mm, the three reference point locate at the absolute length 4mm, 8mm, and 12mm away from weld toe, using quadratic extrapolating.

$$\sigma_{hs} = 3 * \sigma_{4mm} - 3 * \sigma_{8mm} + \sigma_{12mm} \tag{2.6}$$

- For coarse mesh of hot spot type B, elements should have a length of 10mm at the hot spot, the reference point located at 5mm and 15mm, using linear extrapolation.

$$\sigma_{hs} = 1.5 * \sigma_{5mm} - 0.5 * \sigma_{15mm} \tag{2.7}$$

The recommendation from IIW for mesh size and reference point are concluded in the following Figures 2.5 2.6

Type of model and weld toe		Relatively coarse models		Relatively fine models	
		Type a	Type b	Type a	Type b
Element size	Shells	t x t max t x w/2[a]	10 × 10 mm	≤0.4 t x t or ≤0.4 t x w/2	≤4 × 4 mm
	Solids	t x t max t x w	10 × 10 mm	≤0.4 t x t or ≤0.4 t x w/2	≤4 × 4 mm
Extra-polation points	Shells	0.5 t and 1.5 t mid-side points[b]	5 and 15 mm mid-side points	0.4 t and 1.0 t nodal points	4, 8 and 12 mm nodal points
	Solids	0.5 and 1.5 t surface centre	5 and 15 mm surface centre	0.4 t and 1.0 t nodal points	4, 8 and 12 mm nodal points

Figure 2.6: Reference mesh and extrapolating[21]

2.1.3. Traction based structural stress

Recent research has focused on developing and refining surface extrapolation methods to compute hot spot stress. Alternatively, traction forces based has developed an innovative approach for determining structural stress at the weld toe or root[47]. This method focuses on the position of nodes and nodal forces. In Healy's research the hot spot stress around weld toe was calculated using surface extrapolation method and the traction forces based structural stress method[17]. The comparison of stress was made over different FE solvers, mesh refinements, and element types, which indicates the superior insensitivity and better accuracy of traction forces based procedure[18]. Since there is very less literature available on the traction forces based method, only the important parts are discussed

here.

When approaching the weld toe, the stress values obtained are influenced by the singularity induced by the notch. To prevent this effect, the reference node for stress and force evaluation should be selected at a distance from both the weld toe and the weld seam. Thus this method is not sensitive[11] to mesh size. For convenience, a row of elements with same length of δ can be used in the finite element model, as Figure 2.7.

Stress-based method by Dong As Figure 2.3, for the solid model with monotonic stress distribution in the direction of through thickness. As Figure 2, the normal structural stress was defined at section A-A, the second reference section was defined as B-B. The distance is element size δ. By imposing equilibrium conditions between sections A–A and B–B[11], the bending stress σ_b and membrane stress σ_m can be written as[11]:

$$\sigma_m = \frac{1}{t} * \int_0^t \sigma_x(y) * dy \tag{2.8}$$

$$\sigma_b * \frac{t^2}{6} + \sigma_m * \frac{t^2}{2} = \frac{1}{t} * \int_0^t \sigma_x(y) * y * dy + \delta \int_0^t \tau_{xy}(y) * dy \tag{2.9}$$

Where the σ_x is the nominal stress in x direction, δ is the element size, τ_{xy} is the shear stress, and t is the thickness of plate. Equation 2.8 represents the force balance along B-B and equation 2.9 represents the moment balance along A-A.

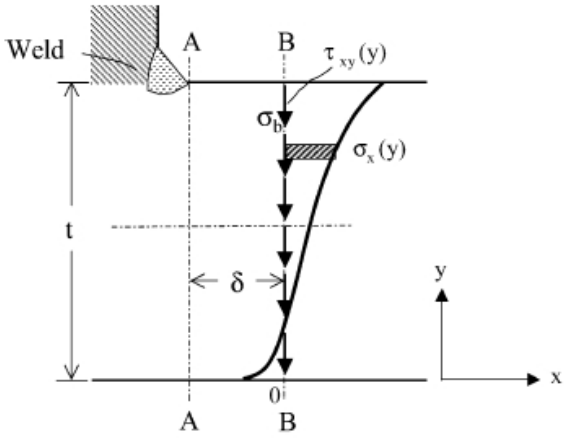

Figure 2.7: Structural stresses calculation procedure for through-thickness fatigue crack.[11]

Nodal force-based method Another approach is based on nodal force and moment. As the displacement-based FE analysis, the most accurate solution quantities are nodal force and nodal moment[13]. This two kinds of values should be used to extract structural stress to ensure reasonable insensitivity of mesh size in structure discontinuity(such as weld toe). In real FEM meshing case especially for weld toe and the plate area near it, there is always some irregularly shaped mesh existing. In Dong's article[13] a simultaneous equation was formulated to relate nodal force and line force.

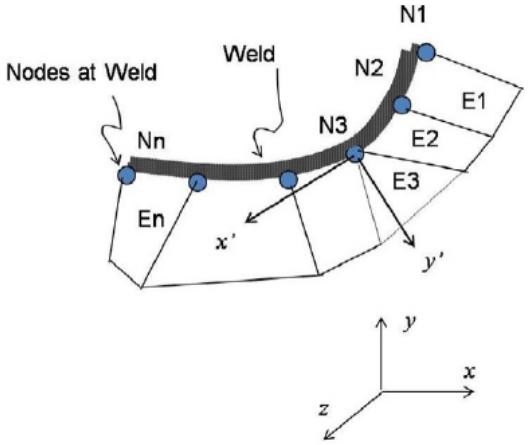

Figure 2.8: Coordinate converting.[50]

As Figure 2.8, nodal force vectors extracted from different elements are rotated from the global coordinate system(x,y,z) to the local coordinate system(x',y',z') along curved weld seam. For shell elements, the work done by nodal force over nodal displacement is equal to the work done by line force over same nodal displacement. The vector of linear force could be obtained with the following equation:

$$\begin{Bmatrix} F_1 \\ F_2 \\ F_3 \\ \vdots \\ \vdots \\ F_n \end{Bmatrix} = \begin{bmatrix} \frac{l_1}{3} & \frac{l_1}{6} & 0 & 0 & \cdots & 0 \\ \frac{l_1}{6} & \frac{(l_1+l_2)}{3} & \frac{l_2}{6} & 0 & \cdots & 0 \\ 0 & \frac{l_2}{6} & \frac{(l_2+l_3)}{3} & \frac{l_3}{6} & 0 & 0 \\ 0 & 0 & \ddots & \ddots & \ddots & 0 \\ \vdots & \ddots & \ddots & \ddots & \frac{(l_{n-2}+l_{n-1})}{3} & \frac{l_{n-1}}{6} \\ 0 & \cdots & \cdots & 0 & \frac{l_{n-1}}{6} & \frac{l_{n-1}}{3} \end{bmatrix} \begin{Bmatrix} f_1 \\ f_2 \\ f_3 \\ \vdots \\ \vdots \\ f_n \end{Bmatrix}$$

Figure 2.9: Nodal to line force converting.[13]

If the crack is parallel to the weld seam, the local coordinate axis x' and y' should be verticle to the weld toe[11]. In equation of Figure 2.9, $f_1, f_2, ..., f_n$ represents the line force along y' direction. $l_1, l_2, ..., l_n$ are the element edge length projected on the weld line for corresponding elements. The nodal force F represents the sum of all nodal forces from adjacent elements in the local coordinate system. The line moment can be obtained by using the same procedure and equation. Then the structural stress(sum of membrane stress and bending stress) is able to calculated with following equation for shell model[13]:

$$\sigma_s = \sigma_m + \sigma_b = \frac{f_{y'}}{t} - \frac{6m_{x'}}{t^2} \tag{2.10}$$

For solid model, the nodal forces in through thickness direction can be also linearized by same method as Figure 2.9.

2.1.4. Effective notch stress

Notch stress is the total stress at a local notch formed by the weld toe or weld root, as determined by linear elasticity theory. Compared to hot spot stress concept, the effective notch stress concept also includes the nonlinear peak stress[45]. This concept is based effective notch. One way to implement effective notch concept is do not consider the plastic-elastic material at crack tip[20], but is based on the highest computed elastic stress at the critical point. In Qin's article[44] the through thickness weld notch distribution σ_n was divided into 3 zones: the zone 1 peak stress; the zone 2 notch affected stress gradient; zone 3 far field dominated stress. ENSC is the approach that adopts a micro- and meso-structural notch support hypothesis. The effective notch stress(ENS) range S_e = σ_e could be estimated by averaging the notch stress distribution along a crack path over a material characteristic micro- and meso-structural length[44]. The integral process will be introduced detailed in research chapter.

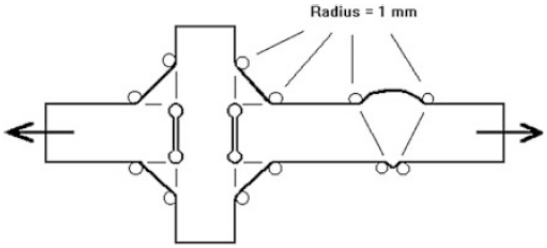

Figure 2.10: Effective weld contour.[21]

Another way is that considering the geometric of weld and nonlinear material behavior, the real weld contour is replaced by the effective weld contour here as Figure 2.10. This method has requirements w.r.t weld shape, size, element size, etc. For structural steels and aluminum alloys, 1mm of effective notch radius has been validated[21]. This method is only applicable to assess potential fatigue failures for weld joints from weld toe and weld2.11. Another restriction for ENSC is that it not applicable for the condition that there is significant stress component parallel to weld seam. The recommendation of weld angle is also given: 30 degrees for butt weld and 45 degrees for fillet weld. And the thickness should be limited to more than 5mm because ENSC is not validated for the apply of thin plates. The recommendation from IIW of element size is shown in Figure 2.12

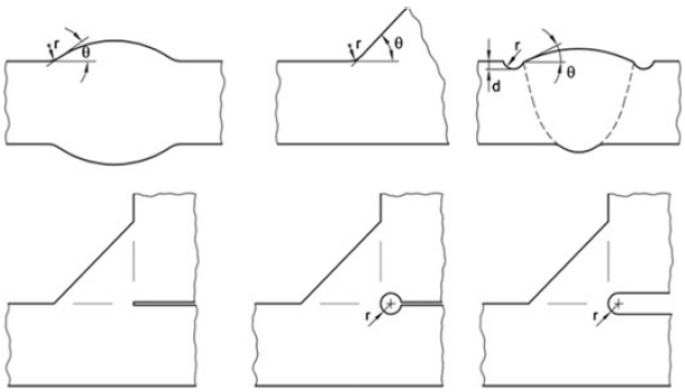

Figure 2.11: Recommand weld shape for ENSC.[21]

Element type	Relative size	Absolute size [mm]	No. of elements in 45° arc	No. of elements in 360° arc
Quadratic with mid-side nodes	≤r/4	≤0.25	≥3	≥24
Linear	≤r/6	≤0.15	≥5	≥40

Figure 2.12: Recommand element size on surface.[21]

2.2. Finite element analysis

The finite element analysis(FEA) is a computational technique used to predict physical system behavior in various conditions. It is implemented by breaking down a complex problem into smaller, which is so-called ”Finite Element”(FE). Then analyze the single finite elements and then gather them together to derivate the whole system’s behavior. This method is the finite element method(FEM). FEM was used to quantify and approximate various physical phenomena. FEA emerged from numerical methods and computational mechanics in the mid-20th century. Its development was tied to aerospace, automotive, civil engineering, maritime, and offshore engineering industries. The method became practical with the advent of digital computers, enabling the analysis of complex systems that were unsolvable by traditional analytical methods. Nowadays, many companies and institutions have developed their own FE solvers for different goals, but the most general FE solvers are ”ANSYS” and ”ABAQUS”. Generally, ABAQUS performs better in nonlinear case, for instance: wave impact, element destruction and crack calculation. On the other hand, ANSYS is more popular in static and quasi-static problems. Due to the fatigue assessment is linear case and static, the simulation software for this article will be ANSYS.

Fluid mechanics, solid mechanics, and thermodynamics are subclasses in which the world was identified as a continuum. The assumption of continuum means that physical properties are distributed through space and connect with material points[10]. These continuous media could be described as partial differential equations(PDE). The different FE solvers can solve the physical behaviors by using these PDE[39], for instance: strain, stress, force, displacement, and crack.

All results in this research will be based on the simulation data of the FEM, thus the accuracy of FEM modeling will be most crucial. Due to the fatigue assessment is linear case and static, the simulation software will be ANSYS. First, shell element model geometry of large scale specimens with and without welds will be built separately. Then boundary conditions and load will be applied according to the reference articles[31][6]. In post-processing, the nodal force and stress will be extracted in specific location, according to the method referenced in section 2.1.3 and 2.1.2. Solid model will be also built, the process of pre- and post-processing will be the same as for shell element model.

When it comes to the fatigue assessment, the determination of element type and element size is very crucial. Different element types are recommended for different cases by IIW[36].

2.2.1. Shell formulation

Shell elements are 2-dimensional elements, in which the actual material thickness is given as only property for the element. If the ratio of thickness to length is rarely small, the shell element model is able to offer accurate approximation. In general, the shell element model is suitable for solving elastic structural stress[21]. Mid-plane stress is equal to membrane stress and the surface stress(at bottom and top) is equal to the sum of the membrane stress and bending stress. When it comes to capturing nodal forces, the sum over the nodal forces of adjacent elements should be use, but not opposite elements, due to meaningless.

The deformation fields are defined as linear (3 or 4-node element) or parabolic (8-node element). For low-order linear elements, triangular and rectangular shape elements are possible[39], as Figure 2.13. The triangular element always generated at unregular areas, like weld or other joints, which have less degree of freedom than rectangular element. Increasing element degrees of freedom leads to more accurate simulations. This means that the result in 4-node elements is more accurate than that of

3-node elements[22].

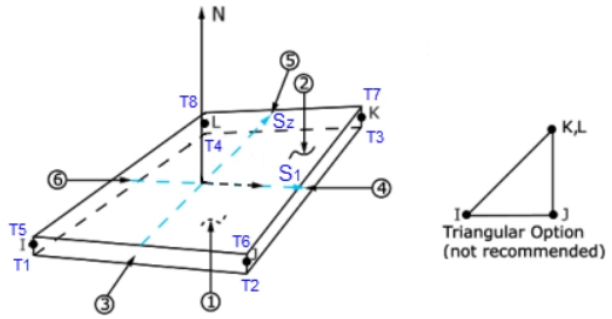

Figure 2.13: 3-node and 4-node shell element shape.[1]

For HS type A, the element size along the direction of stress should be generally 1.0t. The convergence check will also be investigated in this research. At the ends of longitudinal brackets or similar details, the result will be sensitive to the element size. The greater element size probably leads to non-conservative results[37]. For typical details as Figure 2.14 the element size should equal to the plate thickness but should not be greater than the half of attachment width. For the case of other details of HS type A and type B are shown in Figure 2.6

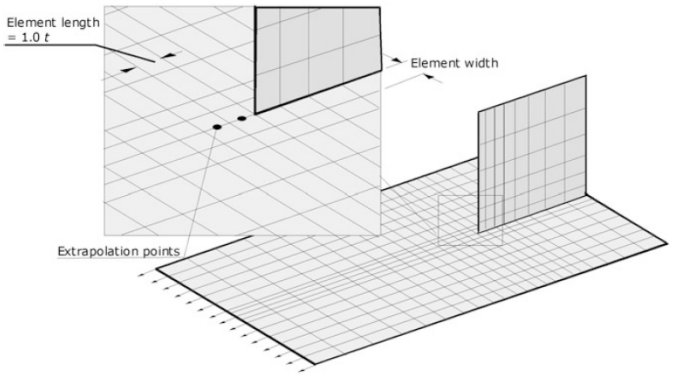

Figure 2.14: Typical coarse mesh at bracket end.[37]

2.2.2. Solid formulation

Solid elements are required for modeling structures with 3-dimensional deformation and stress fields. The thickness is modeled thus the variation of thickness is considered. Compared to shell element, this leads to a similar result to the real case. The shape of solid elements are usually 4-node tetrahedron, 10-node tetrahedron, 8-node hexahedron, and 10-node hexahedron, as Figure 2.15. The stress can vary in all three directions, and the nodes also have displacements in three directions.

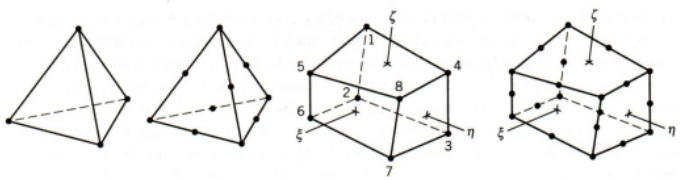

Figure 2.15: Solid element shape.[60]

In general, solid element model is more accurate in the description of geometry than the shell element model. But on the contrary, generation of solid mesh maybe more laborious than shell elements, it

requires more computing time for computers. In weld components, the weld shape can be modeled as real case. The linear distribution could be obtained by using of single-layer of 8-node cube linear solid[36]. The single-element through thickness and 2-point integration can achieve correct linear shell stress distribution.

2.2.3. Link formulation

Rigid bar elements are useful for connecting adjacent nodal points, such as to satisfy continuity conditions, as Figure 2.19. Alternatively, kinematic constraint equations can achieve the same purpose without introducing undesirable side effects[36].

2.3. Weld modelling

The most general method of building weld in FEM plate intersections is the oblique element method. This approach was first proposed and described by IIW[36], as Figure 2.16. The weld modeling implemented by increasing element thickness was also introduced in the same book but the author did not offer relative recommendations, as Figure 2.17. In this section the two kind of weld modelling method in FEM will be introduced.

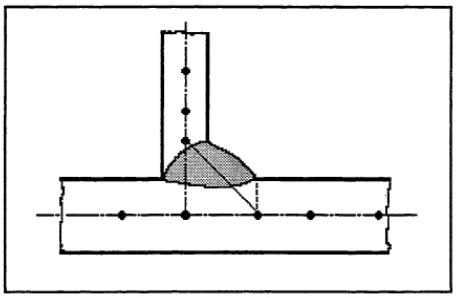

Figure 2.16: Inclined elements for weld modelling.[36]

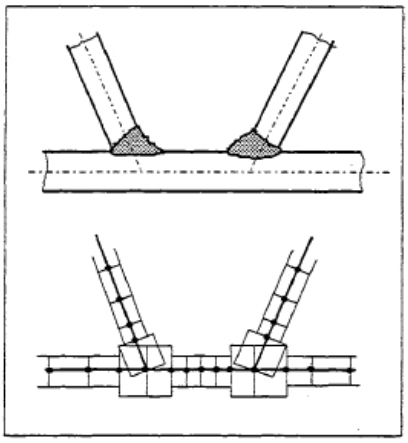

Figure 2.17: Increased thickness in the weld zone.[36]

2.3.1. Inclined shell

IIW guidlines[37] described the application and limitations of the inclined element method. The inclined elements are generated to connect the adjacent elements in intersecting plates, as Figure 2.18 a. This method represents both weld stiffness and geometry. However, the stiffness of the weld cannot be accurately simulated in this way, thus inclined element method is not applicable for weld root failure. Due to the stiffness and geometry are both crucial for this failure mode. This method exaggerates

the area of the cross-section near the intersection, which is also a disadvantage in longitudinal loaded joints.

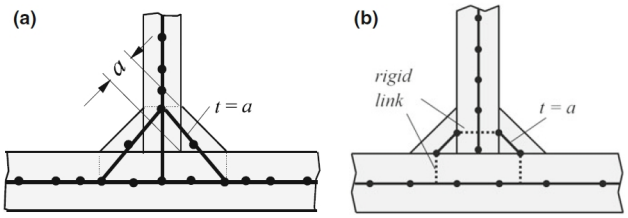

Figure 2.18: Fillet welds in a T-joint modelled with inclined elements having mid-side nodes(a) or connections with rigid links(b).[36]

2.3.2. Rigid link

An upgrade approach is implemented by using additional rigid links to the element in mid plane of the plates, the inclined elements are only used in fillet welds[59],as shown in Figure 2.18 b.

The rigid link method can make sure that the area of cross-section will be equal to the actual area in the shell element model. The foundation of this approach relies on modeling the local rigidity of a joint generated from the weld stiffness. This is implemented by connecting two adjacent shell elements with rigid links, each linking pairs of nodes along the entire weld length, as Figure 2.19.

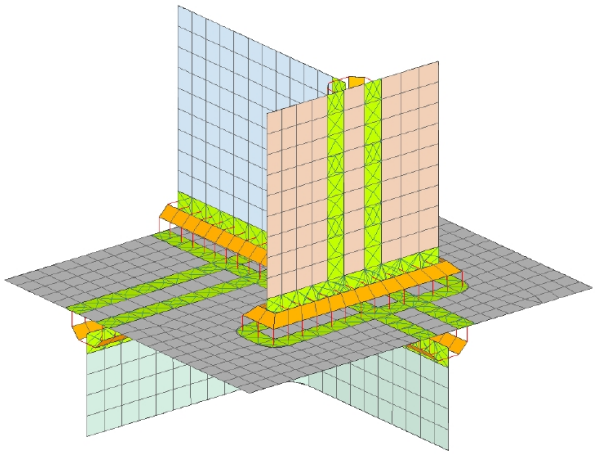

Figure 2.19: Specified rigid link for shell element model.[59]

2.3.3. Increased thickness

In Niemi's book[36] a weld modelling method in FEM was proposed by increasing the thickness in the weld area. In shell element model the stiffness of weld could be incorporated by increasing the thickness of elements near the weld[46]. In Eriksson's book[15] the thickened element are recommended to be applied in both intersecting plates for double-side fillet welding. This thickness of reference elements are also recommended to enlengthed with the increasing of weld leg length. In Niemi's book[37] the elements at weld region has an increased length corresponding to the sum of the weld leg length and half the thickness of the plate. Increasing the thickness of the element at the weld location can also include weld effects[46], Increased thickness of shell elements at the location of weld joints are shown in Figure2.20.

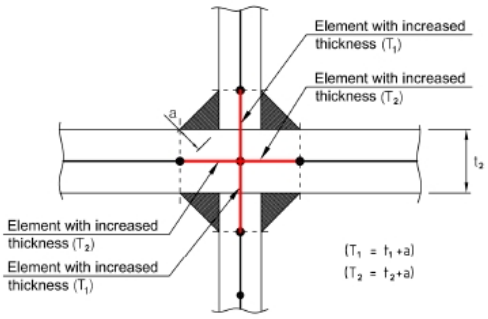

Figure 2.20: Increased thickness of shell elements at the location of the weld.[46]

In FEM modeling, the choice of weld model should depend on the shape and parameter of component details, and the crack position. The rigid body method is more applicable in weld root failure cases than inclined element method due to a better simulation of stiffness, but it also meaning more work in FEM modeling. In shell element modeling, two intersection plates connected by weld seams are separated and reformulated, as Figure 2.19. In this research only weld toe crack mode occurs, the rigid link method has no clear advantage over inclined shell method. Besides, increased thickness method does not include weld end, which does not apply to this study. Thus inclined element method will be chosen in FEM modeling.

2.3.4. Solid

The weld of the solid element model can be built on a real-world basis. The solid weld in the direction along the weld seam will be built as a triangular prism. As for the weld end, the triangular prism is also built in the through-thickness direction. They will be connected to each other by a partial cone, as Figure 2.21.

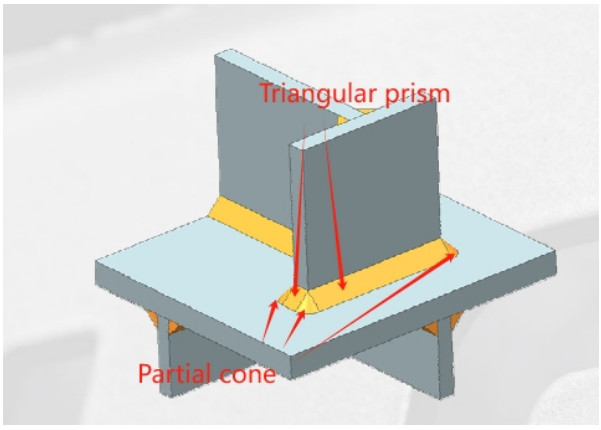

Figure 2.21: Solid weld model.[59]

2.4. Large scale fatigue specimens

In this chapter, different Large-scale specimens(LSS) will be discussed. Including component details and parameters. In this research, the LSS mentioned in this chapter will be modeled and analyzed, thus capturing details and dimensions for LSS is necessary. Compare to SSS, LSS involves more structure members and provides more realistic loading, response paths and welding induced residual stress distributions. Due to planar structure and tubular structure have different behaviors in fatigue, they will be introduced in different subsections.

2.4.1. Planar structural details

In this section the LSS from Berge's[6] and Miki's[31] will be introduced. The weld end occurs in the lug plate of frane-stiffener model below, and the cope holes of stiffener-plate model. These will be the important objective of this research.

Frame-stiffener model(FSM) The first object test model is a stiffener-frame planar structure in an FPSO from Berge's article[6]. The overview of global geometry is shown in Figure 2.22. The structure mainly consists of a shipside plate at the bottom, two frames at both sides, one center frame, one longitudinal stiffener, and three stiffeners on frames. Dimensions are given as table 2.1

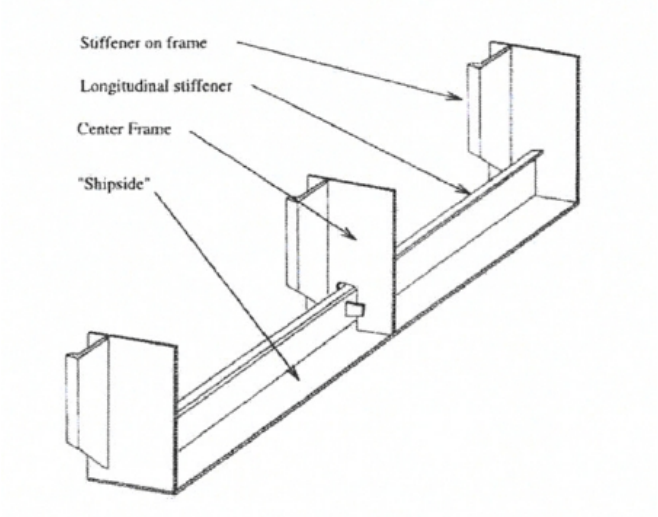

Figure 2.22: Globel geometry of Berge's model.[6]

Components	Dimentions
Shipside plate	6400*800*16mm(L*B*T)
Frames	1300*800*12mm(H*B*T)
Lug	12mm (T)
Longitudinal stiffener	HP 320*14
Stiffener on frame	HP 260*12

Table 2.1: Components dimention of Berge's model

The longitudinal stiffeners and stiffeners on frame are bulb flats. Bulb flats are a kind of specialized type of structural steel used in maritime, offshore, or other LSS applications. It offer a cost-effective, efficient, and corrosion-resistant solution for plate stiffening requirements. Key advantages include an excellent strength-to-weight ratio, providing superior buckling resistance at a lower weight compared to flat bars or angles[56]. The bulb rounded protrusion on one side, the detailed explanation is shown in Figure 2.23. The bulb flat offers relatively more strength and stability while reducing weight. The dimensions of the longitudinal stiffener is Holland Profile(HP) 320*14; the dimensions of stiffeners on frame is HP 260*12. where the detailed parameters could be found in Figure 2.24

le bulb flats problem.

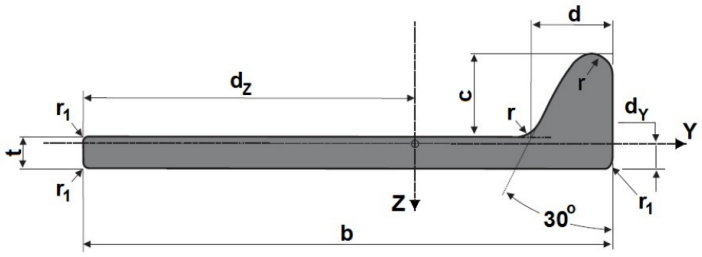

Figure 2.23: Definition of bulb flats shape and parameters.[38]

Section description						Mass per metre	Area of section	Surface area per metre	Distance to centre of gravity	
	b mm	t mm	c mm	d mm	r rmm	G Kg/m	A cm^2	U m^2/m	dx mm	dy mm
260x12	260	12.0	37.0	38.7	11.0	32.43	41.25	0.600	158.2	11.3
260x13	260	13.0	37.0	38.7	11.0	34.40	43.85	0.602	156.5	11.6
280x10.5	280	10.5	40.0	42.0	12.0	32.40	41.22	0.641	175.7	11.6
280x11	280	11.0	40.0	42.0	12.0	33.50	42.62	0.642	174.5	11.7
280x12	280	12.0	40.0	42.0	12.0	35.70	45.42	0.645	172.4	11.9
280x13	280	13.0	40.0	42.0	12.0	37.90	48.22	0.647	170.5	12.2
300x11	300	11.0	43.0	45.3	13.0	36.70	46.73	0.687	189.1	12.4
300x12	300	12.0	43.0	45.3	13.0	39.09	49.73	0.690	186.7	12.7
300x13	300	13.0	43.0	45.3	13.0	41.44	52.73	0.692	184.6	12.9
320x11.5	320	11.5	46.0	48.6	14.0	41.20	52.59	0.733	202.5	13.3
320x12	320	12.0	46.0	48.6	14.0	42.60	54.19	0.735	201.3	13.4
320x12.5	320	12.5	46.0	48.6	14.0	43.80	55.79	0.736	200.1	13.5
320x13	320	13.0	46.0	48.6	14.0	45.09	57.39	0.737	199.0	13.6
320x13.5	320	13.5	46.0	48.6	14.0	46.30	58.94	0.737	198.0	13.7
320x14	320	14.0	46.0	48.6	14.0	47.60	60.54	0.738	197.0	13.9

Figure 2.24: Bulb flat parameters.[56]

Another detail in stiffener-frame structure is the transition in mid frame. The mid frame right side near longitudinal stiffener flat section and the left side near bulb section is hollowed. And in right side, the mid frame connects with longitudinal stiffener by using a trapeziform lug plate, where the lug plate have 16mm thickness. Detail and dimensions in transition is shown in Figure 2.25.

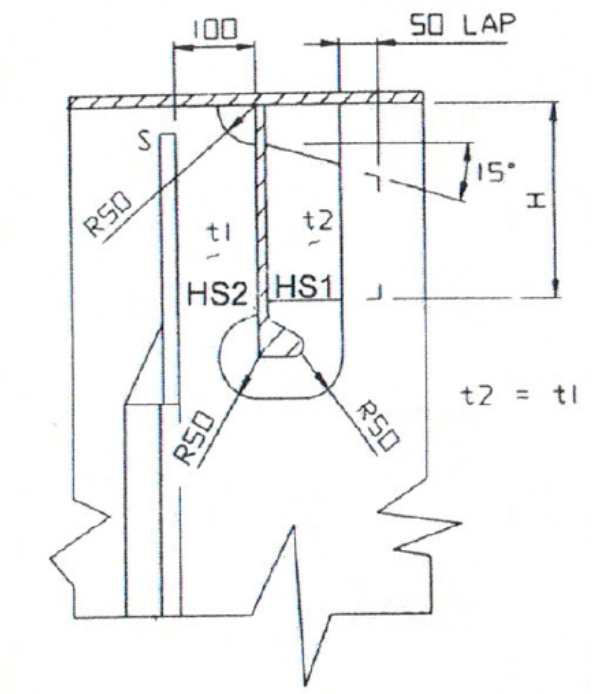

Figure 2.25: Dimension in transition.[6]

The hot spot 1 is located at the lug plate and the hot spot 2 is located at the stiffener web, as Figure 2.25. The load range was 40-400KN with a mean load of 240KN. The cyclic of loading was 0.5Hz. The model was welded to a steel which was bolted to the floor. The actual load is a hydrostatic pressure. Here as an approximation the two equal point load at the mid of shipside plate was assumed, as Figure 2.26

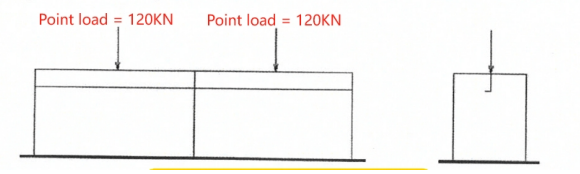

Figure 2.26: Load condition of Berge's model.[6]

Stiffener-plate model (SPM) Another object test model is a stiffener-plate planar model proposed by Miki [31]. The basic model is simple, only consisting of two flanges, two plates and one web. The web is located at mid, two flanges are located at top and bottom side vertical to the web. The two plates located at the left and right sides are vertical to both web and flanges. In real case, these stiffener-plate models are continuously connected to each other. The side plates are built to separate each other on the geometry. The flanges have 1500mm length, 250mm width, and 16mm thickness; the web has 1500mm length, 500mm height, and 9mm thickness; the plate have 9mm thickness. Additionally, the weld throat is 5mm. Based on this, the research models are divided into three types: specimen 1, 2, and 3, as Figure 2.27.

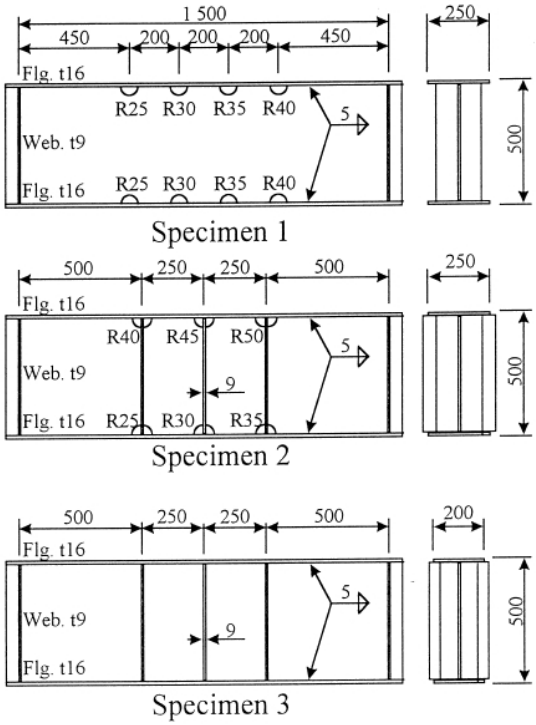

Figure 2.27: Stiffener-plate model parameters.[31]

Type	Thickness (mm)	Y.S. (MPa)	T.S. (MPa)	El. (%)	C (%)	Si (%)	Mn (%)	P (%)	S (%)
SM490YA	9	404	551	22	17	0.35	1.29	0.018	0.004
SM490YA	16	441	559	25	16	0.40	1.24	0.014	0.003

Figure 2.28: SM490YA properties.[31]

The material of the specimens is SM490YA, the properties are given in Figure 2.28. Specimen 1 has 8 cope holes and specimen 2 has 6 cope holes, but specimen 3 does not have. Specimen 2 have 3 intersecting plates that parallel to side plates. The radii of cope holes for specimen 1 and 2 are given in table 2.2

-	Radii in Specimen 1	Radii in Specimen 2
Cope hole numbers	8	6
Cope hole radii	25,30,35,40mm	25,30,35,40,45,50mm

Table 2.2: Cope hole data

Figure 2.29 gives the load, crack, and weld conditions for three specimens. The value of load condition are given in table 2.3. The position of line load is given in Figure 2.30. Specimen 1 and specimen 2 have two kinds of weld shapes. Type A weld has a traditional boxing weld in the weld end, but type B weld does not have boxing welds. This results in different crack growth directions for the same specimen. Thus the hot spot type and stress range will be various.

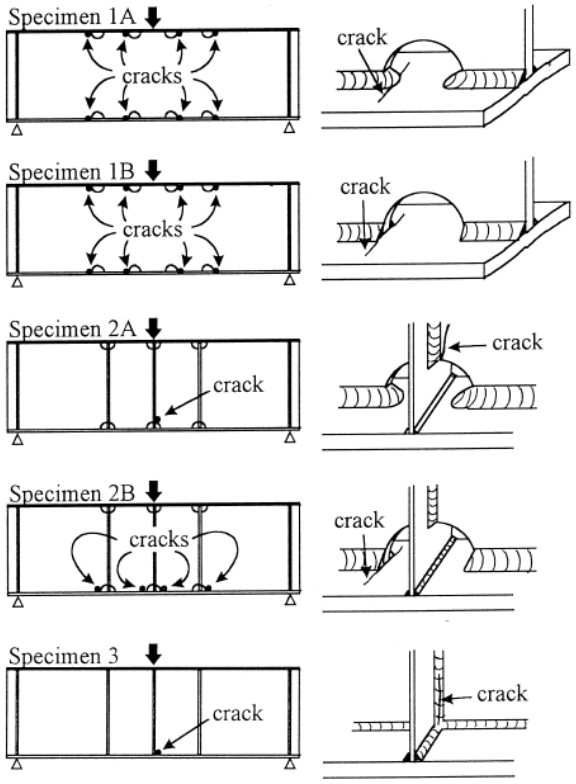

Figure 2.29: Load, crack, and weld condition of stiffener-plate specimens.[31]

Load range	Load repitation
400-450KN(take 450KN in calculation)	1-2Hz

Table 2.3: Load condition

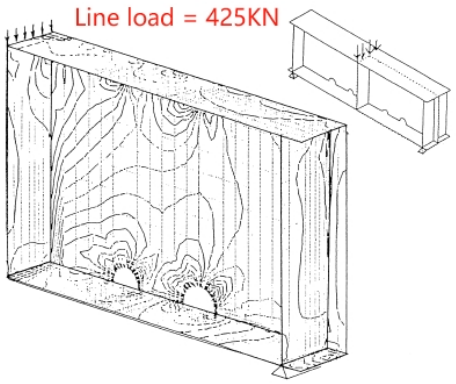

Figure 2.30: Line load for specimens.[31]

2.4.2. Tubular structural details

Tubular structures are widely used in maritime and offshore industries due to their excellent structural performance. Stress concentration, particularly in the welded joints of these structures, is a crucial design consideration, especially in the context of fatigue design. The fatigue behavior of tubular structure is different from planar model, several types of tubular joints are given in Figure 2.31

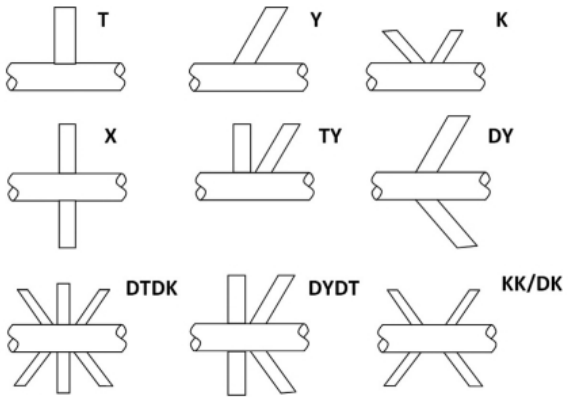

Figure 2.31: Various tubular joints.[48]

Compared to the planar model, the stress distribution will be more complicated in multi-planar tubular specimens. The tubular joints could be divided into circular and non-circular cross-sections. Circular cross-section are more common due to there is no sharp corners and irregular shapes. Thus stress concentration could be ignored. However, Since geometry is often required during actual manufacturing, non-circular cross-sections can also exist. So it usually has worse fatigue performance than circular joints. In tubular structures the extreme fibers contribute a lot to the bending moment, the weld model will be more important than that of planar model[29].

T-Joint tubular structure A typical T-joint tubular structure was proposed by Barsoum[3]. Two different weld configurations were built: a three-pass single-U weld groove for maximum weld penetration, and a two-pass fillet (no groove) welded tube-to-plates for minimum weld penetration. The parameters, configurations and two kinds of weld shape are given in Figure 2.32.

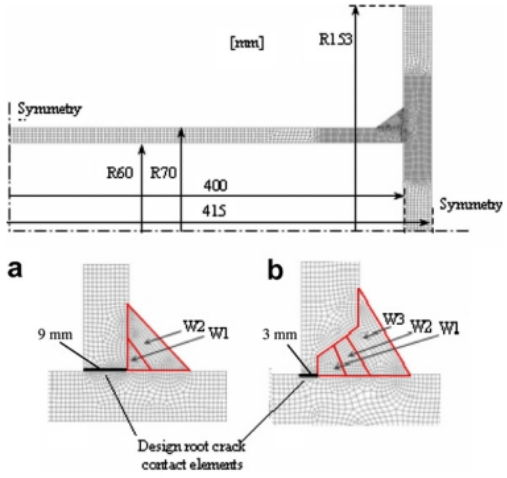

Figure 2.32: T-Joints tubular model.[3]

Barsoum quantified the influence of the weld penetration depth and studied the effects of residual stresses on the fatigue life and the crack path. The tubular joints were divided into five different batches, as Figure 2.33. Figure 2.34 shows the fatigue resistance data based on the number of cycles N to failure, which is represented in S-N curve. It is obvious to see that the B4 batch(fillet weld with no groove) has significantly lower fatigue resistance than other cases. This is because the small compressive residual stress exists in the weld root, which allows the crack to propagate from the root side[3].

	B1*	B2*	B3*	B4**	B5* (stress relief)
$P_{internal}$ (MPa)	0	25	15	0	0
$FAT_{50\%}$[c]	155	137	132	108	146
FAT according to IIW	142	123	116	83	142
Failure	Toe	Root[a]	Root[a]	Root	Toe[b]

[a] One test object failed at weld toe (between weld and tube) at 18 kNm.
[b] One test object failed at weld toe (between weld and plate) at 20 kNm.
[c] Fatigue strength at two million cycles at a 50% failure probability.
* Single-U weld groove.
** Fillet weld (no groove).

Figure 2.33: Fatigue test data from Baroum.[3]

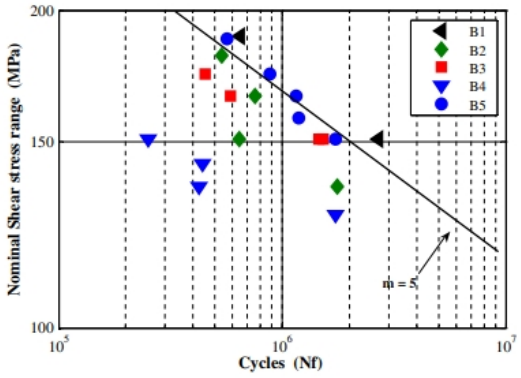

Figure 2.34: S-N plot from Barsoum.[3]

K-Joint tubular structure Wei et al. proposed a continuous large scale tubular structure in the research[62]. The fatigue test of a full-scale welded cast steel truss girder used in the bridge structure

was performed, as shown in Figure 2.35. The tubular truss consists by four complete cast steel joints, connecting each part of the tubular truss. A sinusoidal fatigue load with a frequency of 1.25 Hz, ranging from 100 kN to 1000 kN in fatigue test. Dimensions are also given in the following figure. Fatigue resistance data is shown in S-N plot 2.36

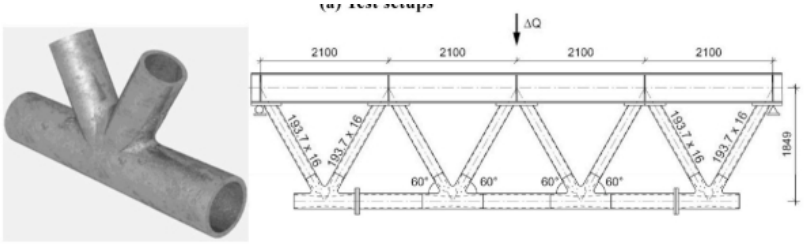

Figure 2.35: K-Joint tubular dimentions.[62]

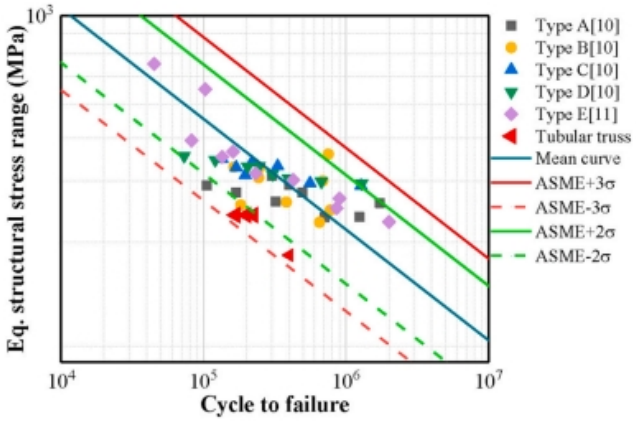

Figure 2.36: K-Joint tubular truss fatigue data.[62]

2.5. Fatigue resistance similarity

This chapter aims to discuss the current understanding of fatigue similarity between small scale specimens and full scale structures, including scale effect, residual stress, and stress gradient. For small scale specimens, Qin et al.[44] already obtained the fatigue resistance scatter band in S-N plot including thousands of examples 2.2, and from that could conclude the effectiveness of the effective notch concept. In this research, I will collect LSS data to compare with SSS to draw conclusions about similarity.

The most noticeable difference between SSS and LSS is the size difference, especially for thickness. Structural components that have different sizes normally show different fatigue behaviors. These behaviors are generally dominated by defects generated from multiple sources, including manufacturing processes[64]. Zhu et al. divided scale effects into 3 categories: statistical size effect, geometrical size, and technological size effect.

2.5.1. Statistical size effect

For AlMgSi1 6082-T6 aluminum alloy specimens and EN-GJS-400-18-LT ductile cast iron specimens, Przybilla et al.[42] and Shirani et al.[51] had already validate the statical size effect in their experiment. In Figure 2.37 the comparison of fatigue data for different scale specimens is shown to prove the scale effect of fatigue resistance.

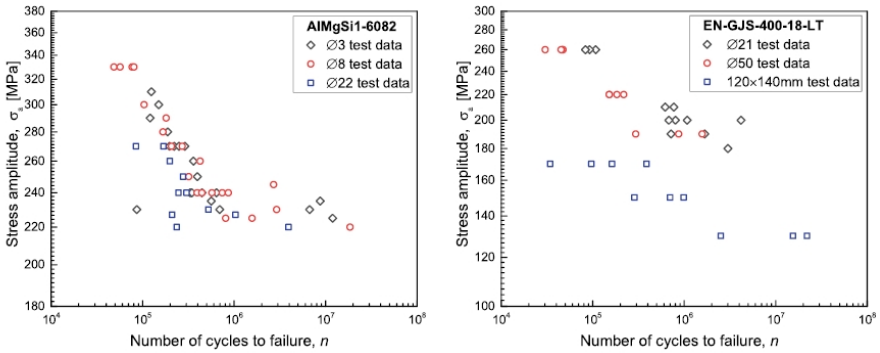

Figure 2.37: Fatigue data comparison from Shirani et al. and Przybilla et al.[51][42]

The fatigue limit of structures normally decreases with its size growth. One important reason is that in high stressed area, the crack is more possible to be generated in bigger specimens[64]. The crack normally leads to failure, thus reducing the fatigue behaviors. The reason of this condition is due to the discontinuity of material. Based on the assumption that the cracks have the same probability of occurrence on the same material and in the same shape, the weakest link will be more likely to appear in bigger specimens, as the explanation from Figure 2.38

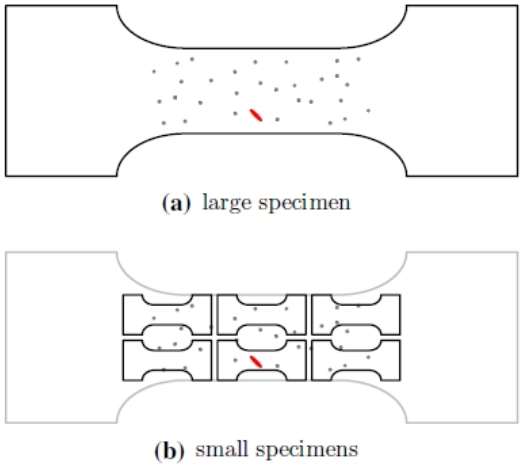

Figure 2.38: Explanation of weakest argument[41]

2.5.2. Welding induced residual stress

Residual stress is the stress that remains in a material after the original cause of the stress has been removed. It can arise from various manufacturing processes, treatments, and mechanical operations. In maritime and offshore structures, the residual stress is always induced by the plastic deformation while welding. Residual stresses significantly influence the fatigue strength of welded structures. It is well established that high tensile residual stresses negatively impact fatigue life, whereas compressive residual stresses can have a beneficial effect.

From Barsoum's research[3] it is well proved that a three-pass single-U weld groove induces compressive residual stress, which improves the fatigue behavior, as Figure 2.32 and 2.33. Hanssen et al. also analyzed a frame box structure for a two-stroke diesel engine regarding welding residual stresses, post weld heat treatment(PWHT), and fatigue strength. They found that the as-welded specimen have double fatigue lifetime than the stress-relieved specimen, due to compressive residual stress at the root[16].

On the other hand, some people researched the negative influence of tensile residual stress on fatigue

behaviors. From Figure 2.39 it is obvious to see that stress relief heat treatment improves the high-cycle fatigue strength by a factor of two(B and D are stress-relieved specimens, A and C are original specimens). It should be noticed that under the cycles number N = 10^6 there is almost no influence from tensile residual stress[55].

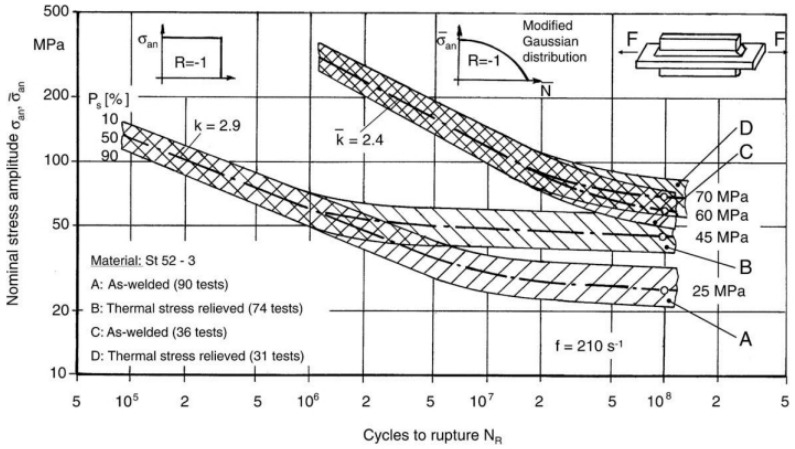

Figure 2.39: Influence from tensile residual stress[55]

2.5.3. Stress gradient

Stress gradient effect is a kind of geometrical scale effect. Notched components always show varying degrees of stress concentration under external loadings. In engineering applications, mechanical components are often designed with various types of notches, such as holes, shoulders, and grooves, to fulfill specific functional requirements. These geometrical discontinuities create stress concentrations, which can lead to complex stress-strain states or even localized plastic deformations.Due to the complex stress and stress gradient distributions in the notch root vicinity, the stress gradient is utilized to explain the notch effect[65].

When the external loading is applied, due to stress concentration, the material at surface near the notch root yields quickly, but the internal material(away from surface in through-thickness direction) does not, which still support the whole component. This is how stress gradient influences the short crack growth. Papadopoulos et al.[40] explain the difference between the scale effect and stress gradient with many examples. Shiratsuchi et al.[52] proved that the relative stress gradient at weld toe depends only on weld toe radius. As Figure 2.40, the stress gradient decreases with the increase of notch radii and becomes a constant when the notch radiu is large enough. The influence of stress gradient on fatigue life still needs to be classified and discussed separately. Liao et al[28]. proves that the fatigue resistance of LSS which have a greater notch size is lower than that of the SSS which has smaller notch size.

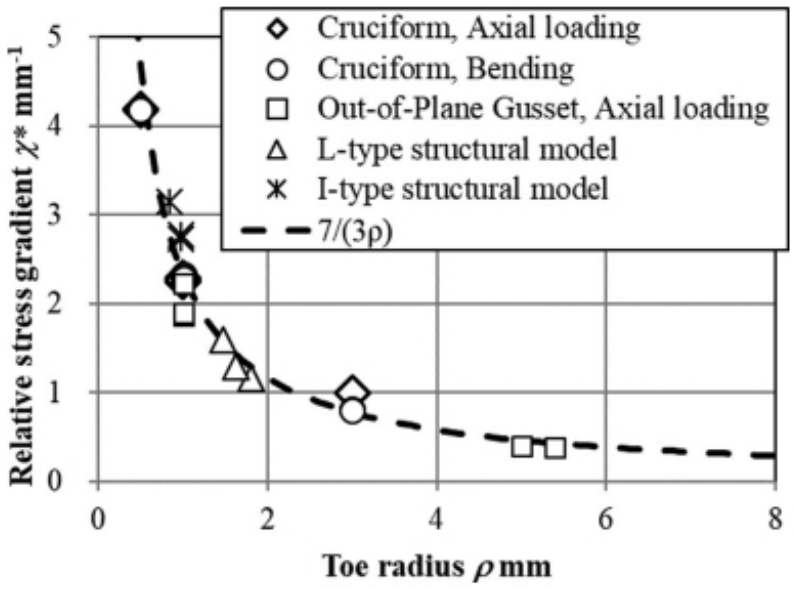

Figure 2.40: Relation between stress gradient and notch radiu[52]

2.5.4. Load path redundancy

A significant influence on fatigue behaviors is the load path. When designing structures, the excess structure parts are usually considered. This is for increasing backup load paths in order to keep the structure safe while some components are failure. The load path redundancy can also divide load to different paths to reduce the significant stress generated in a certain area. In SSS there is almost no load path redundancy. In LSS the load path redundancy is instrumental to redistributing stresses after crack initiation, which decreases the rate of crack propagation and performs better fatigue behaviors[29].

3

Frame-stiffener model details

This chapter focuses on the FEM modeling of frame-stiffener planar model. The properties are given as Figure 2.22 and table 2.1. In order to investigate the weld modeling influence for shell model, and validate the shell model results by simulating the solid model. In addition, surface extrapolation methods and traction forces based procedure were used to calculate the stress range.

3.1. Geometry details

For shell models, the thickness effect should be considered in geometry modeling. In the FEM simulation, the thickness is generated along both sides of through-thickness direction of the defined area. Thus when it comes to geometry generation, the shipside plate length, frame height, and bulb flat dimensions are required to be modified for accurate simulation, as paragraphs below. The global coordinate system of FSM is defined as Figure 3.1.

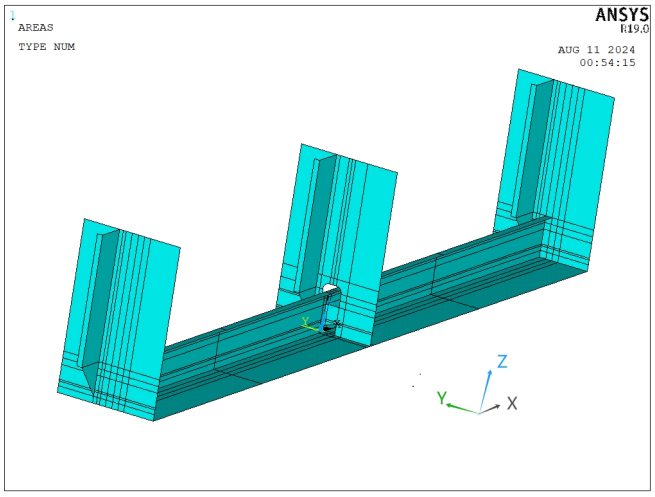

Figure 3.1: Globel coordinate system of FSM.

Geometry details of shipside length and frame height In real (solid) model, shipside plates have 6400mm length in x-direction and frames have 12mm thickness, thus the full solid structure is 6424mm. In order to obtain same dimension in shell model, the shipside plate length should be added with two times of half frame thickness on the basic of 6400mm, thus 6412mm. Similarly, the frame length in y-direction will be 1308mm.

Geometry details of bulb flat dimensions In section 2.4, the shape of a bulb flat had already been introduced. Because the curved area on top cannot be built accurately in shell model, it will be simplified as Figure 3.2. Length of flat b, length of web c, thickness of flat t_{bf}, and section are A are considered to remain unchanged. The parameters are given in Figure 2.24. Because the sectional area remains the same and the geometry does not change much, the change in moment of inertia is minimal. Therefore web thickness t_{bw} can be calculated by the following equation:

$$A = ((b - \frac{t_{bw}}{2}) * t_{bf}) + ((c + \frac{t_{bf}}{2}) * t_{bw})) \tag{3.1}$$

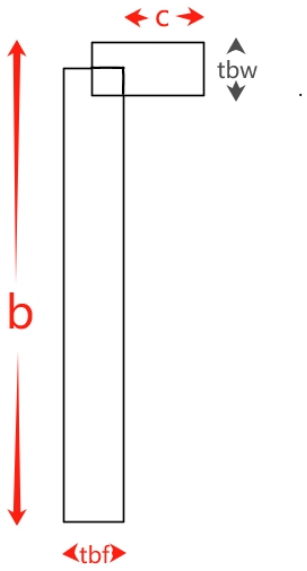

Figure 3.2: Bulb flat simplified configuration.

After calculating, the web thickness of HP320*14 and HP260*12 are 34.9mm and 27.32mm.

3.2. Material properties

Only elastic material properties are defined, due to elastic material behaviors are considered in intact fatigue analysis. In FEA, the structural stress is linearly correlated with load level. The steel properties are given in the following table 3.1.

Steel properties	Value	Unit
Modulus of elasticity	210000	MPa
Poisson ratio	0.29	-
Material density	0.0078	kg/mm^3

Table 3.1: Steel material properties

3.3. Shell element model

This section includes the shell modeling aspects and stress range calculation. Subsection 3.3.1 explained the weld modeling by using inclined shell method; subsection 3.3.2 introduced the aspects of pre-processing; the structural stress is obtained from 3.3.3 and 3.3.4 by using two different methods.

3.3.1. Weld modeling

In this research, weld seams are modeled by using inclined shell method, introduced in subsection 2.3.1. However, the weld shape and dimension are not given in Berge's article. The welds are built along the lug-longitudinal stiffener joint and mid frame-longitudinal stiffener joint, which are located at both sides of longitudinal stiffener. Mid frame, lug plate, and longitudinal stiffener body both have 12mm of thickness. According to IIW's recommendation[37], the weld leg length of shell weld seam is set as 12mm, and the thickness of weld will be 12mm as well. The weld and plates that constitute the vertical joints are at an angle of 45 degrees, as Figure 3.3 3.4 3.5 3.6. In order to obtain more accurate far field stresses, the welds are modeled in both sides of stiffener.

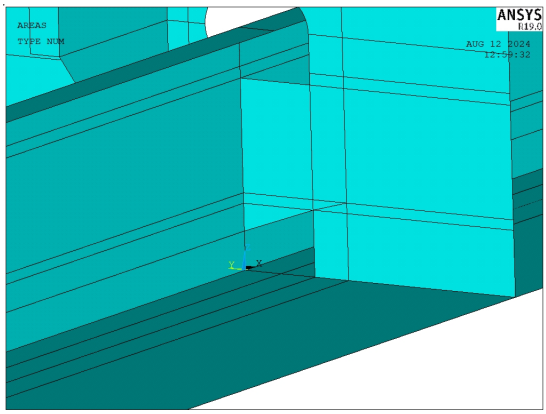

Figure 3.3: Lug-stiffener joint without weld

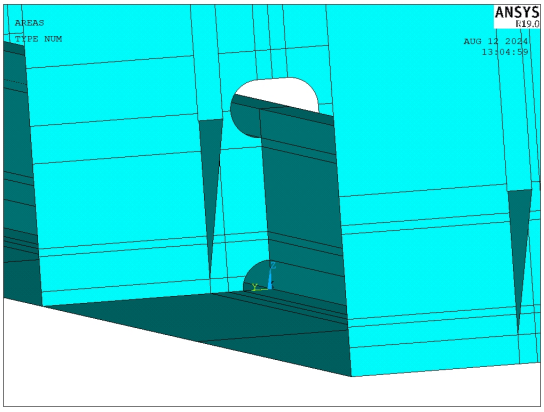

Figure 3.4: Frame-stiffener joint without weld

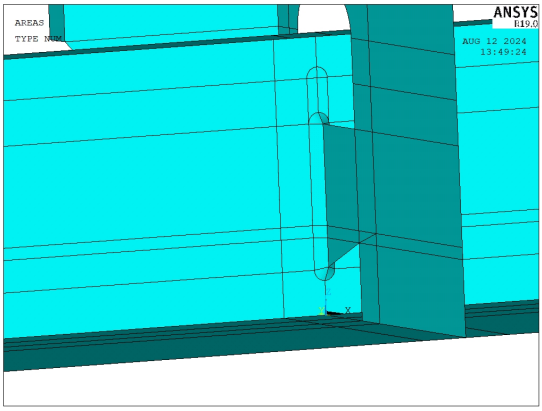

Figure 3.5: Lug-stiffener joint with weld

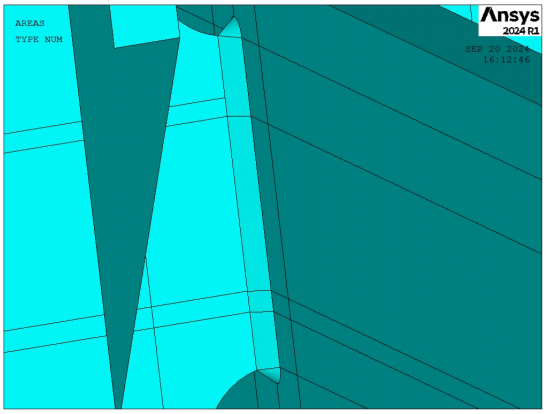

Figure 3.6: Frame-stiffener joint with weld

3.3.2. Numerical modeling

Geometry modeling followed the given data from Berge and the adjustment which discussed in section 3.1. Here, the lug plate modeling is implemented using the offset command. In APDL coding, the thickness of shell element model can be observed by using "eplo" command. As Figure 3.7, the lug plate was divided into 2 regions. Region 2 is the combination of mid frame and lug plate, thus have 24mm thickness. This part of area was offset 6mm from mid frame location along the negative direction of y-axis. Region 1 was offset 12mm from mid frame location along the negative direction of y=axis and had 12mm thickness.

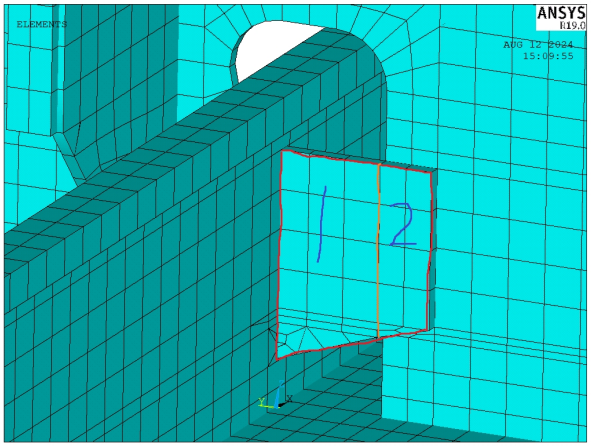

Figure 3.7: Lug plate details.

Element type In this research, element type SHELL181 was applied for shell models. SHELL181 is suitable for analyzing thin to moderately-thick shell structures. It is a four-node element with six degrees of freedom at each node. The element is well-suited for linear, large rotation, and/or large strain nonlinear applications. Change in shell thickness is accounted for in nonlinear analyses. In the element domain, both full and reduced integration schemes are supported. SHELL181 accounts for follower (load stiffness) effects of distributed pressures [1].

Boundary conditions and load The load condition was given in Figure 2.26, two equal point loads with 100KN magnitude in the z-axis positive direction at shipside. Due to the linear FEA and the load range is 400KN, stress range can be obtained by simply doubled structural stress. In real cases, the shipside plate of FSM is located outside and subjected load from seawater. On the contrary, the frames and stiffener on frames(SOF) connected with other components in FPSO in order to stabilize FSM. Therefore, the boundary condition was assumed at the top of frames and SOF, as Figure 3.8. The constraint of translational DOF in x, y, and z directions and rotational DOF around axis are applied in each boundary mentioned above.

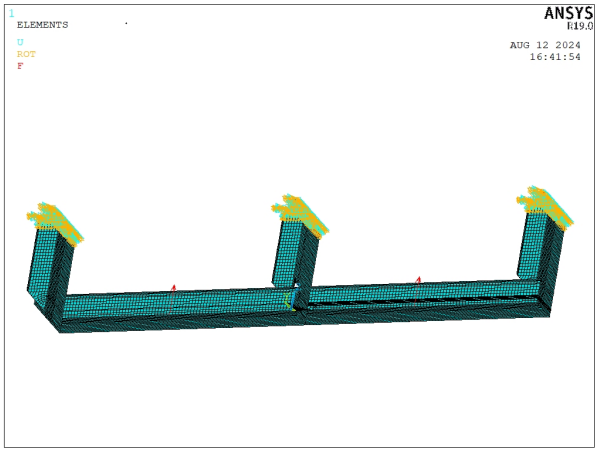

Figure 3.8: Boundary condition and load of FSM.

3.3.3. Structural stress with surface extrapolating method

When analyzing structural stresses, stresses and forces perpendicular to the joint should be taken into account. As figure 3.9, normal stress distribution in the y-direction was given. The HS appeared at the top of the joint, which consistent to Berge's experiment data. From Berge's article[6] it was known that the crack propagates parallel to the weld seam direction, which indicates that the HS is type B, as Figures below:

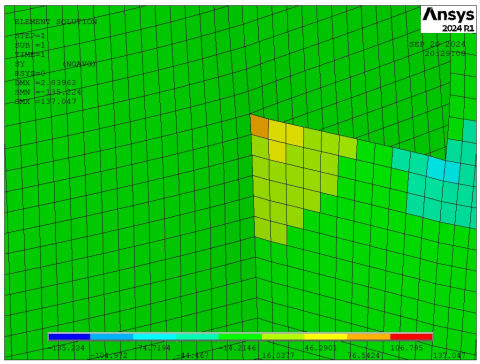

Figure 3.9: Stress distribution and HS of unweld FSM.

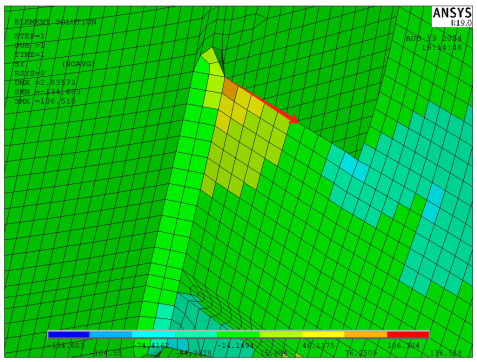

Figure 3.10: Stress distribution and HS of as-welded FSM.

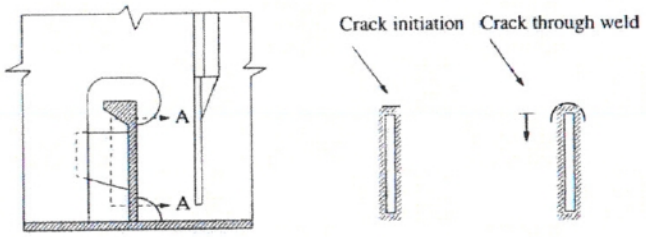

Figure 3.11: Crack initiation and propagation of FSM[6].

Convergence check The convergence check is implemented in this paragraph. Element size was set to 10 different values between 1mm and 12mm. To ensure the accuracy of the convergence check, calculation process for fine mesh is used to obtain structural stress in each case. According to the recommendation of IIW, the stress value of nodes on the top of the lug plate will be extracted, along the negative direction of the y-axis from HS. The normal stress in y-direction are extracted from the nodal solution. For the same node, the stress was averaged between the front and back measured values. In FSM the HS is type B, hot spot structural stress could be obtained by following equation:

$$\sigma_{hs} = 3 * \sigma_{4mm} - 3 * \sigma_{8mm} + \sigma_{12mm} \tag{3.2}$$

Where σ_{4mm}, σ_{8mm}, and σ_{12mm} are nominal stress evaluated with 4mm, 8mm, and 12mm away from HS in FEM. When the node is not locate at the above position, it will be estimated by the adjacent nodes using linear interpolating. Table 3.2 and table 3.3 indicate the results of unwelded models and as-welded models.

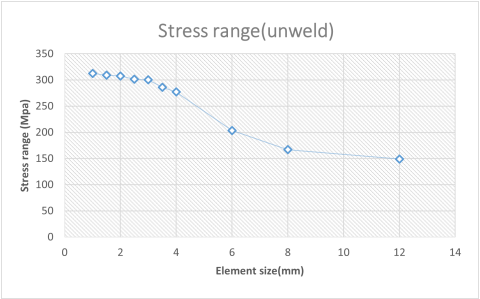

Figure 3.12: FSM unweld model convergence

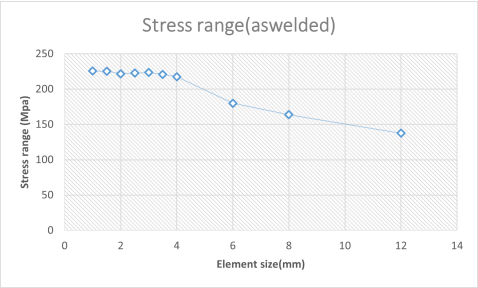

Figure 3.13: FSM as-welded model convergence

Comparison Compared table 3.2 and table 3.3 it is obvious that the hot spot structural stress range in as-welded model is lower than that in the unwelded model. For unweld case, results converged when

Element size	Stress range(MPa)
1mm	313
1.5mm	309
2mm	307
2.5mm	301
3mm	300
3.5mm	286
4mm	277
6mm	204
8mm	167
12mm	149
Berge's experiment	200

Table 3.2: Stress range by using surface extrapolating method for unwelded FSM

Element size	Stress range(MPa)
1mm	225
1.5mm	225
2mm	222
2.5mm	223
3mm	224
3.5mm	221
4mm	218
6mm	180
8mm	164
12mm	138
Berge's experiment	200

Table 3.3: Stress range by using surface extrapolating method for as-welded FSM

ES became 2mm; for as-welded case, results converged when ES became 4mm. The modeling of weld seam significantly decreases structural stress, resulting in values that are closer to the experimental result.

3.3.4. Structural stress with traction forces based procedure

Another method to obtain structural stress is the traction forces based procedure. Nodal force in Y-direction(vertical to weld toe) are used here. In post-processing, the structural force from element solution can provide nodal force which contributes by adjacent elements. Structural stress σ_s consists of membrane stress σ_m and bending stress σ_b, the calculating process in HS type B case are shown below:

$$\sigma_m = \frac{\sum f_{yi}}{t_p'}, f_{yi} = \frac{F_{yi}}{t_p} \tag{3.3}$$

$$\sigma_b = \frac{6 * (\sum (f_{yi} * z_i) - \sigma_m * \frac{{t_p'}^2}{2})}{{t_p'}^2} \tag{3.4}$$

Typically, t_p' is defined as 20mm here(in z direction). Thus, the calculation will consider nodes within about 20mm of the notch, Which was shown in Figure 3.14 and 3.15. The f here is the nodal force in unit width, obtained by nodal force F divide thickness t_p. The factor z_i is the distance between target nodes and notch, t_p is the plate thickness(12mm here). It should also be noted that the last nodal force should be only taken contribution from the element which is close to the notch.

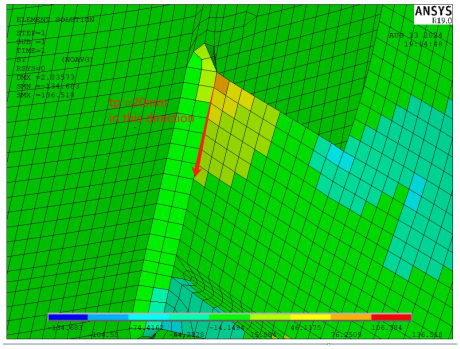

Figure 3.14: FSM nodal force selection in as-welded model

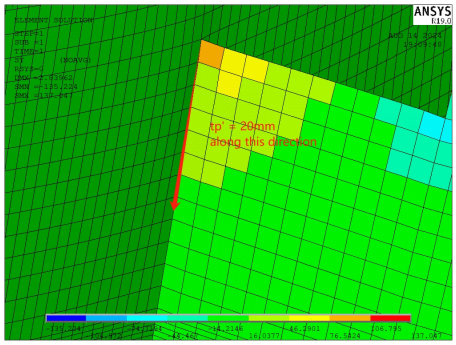

Figure 3.15: FSM nodal force selection in unwelded model

Without weld model Element size were set as 12mm, 10mm, 7mm, 6mm, 5mm, and 4mm separately to validate the convergence. Due to FSM is large-scale, and limited by computer performance the mesh size cannot be further refined to smaller than 4mm. The results obtained did not show clear convergence, however, when the ES is less than 6mm, the results become stable. Therefore, the minimum value of ES=4mm will be taken as the research object.

Element size(mm)	Number of selected Nodes	t'_p(mm)	σ_m(MPa)	σ_b(MPa)	Stress range(MPa)
12	3	24	49	69	236
10	3	20	55	72	253
7	4	21	54	58	223
6	4	18	59	59	237
5	5	20	56	58	228
4	6	20	56	55	221

Table 3.4: FSM Stress range by using traction forces based procedure

With weld model Similar to the results from section 3.3.3, stress range of as-welded model is relatively smaller than that of unwelded model. Meanwhile, the stress range of as-welded model in FEM is almost the same as Berge's experimental data. Moreover, there is almost no difference between the membrane stress of as-welded and unwelded cases. The magnitude difference in stress range is mainly reflected in bending stress. This phenomenon confirms previous assumption in section 3.3.3 about the difference between the two cases, which is the stress concentration difference between the vertical joint and 135-degree joint. Because the membrane stress distributes evenly across the section area, but the bending stress are not evenly distributed across the cross-section and are usually maximum at the surface. The geometry discontinuity-induced SCF mainly influences bending stress.

Element size(mm)	Number of selected Nodes	t'_p(mm)	σ_m(MPa)	σ_b(MPa)	$\Delta\sigma_s$(MPa)	r_s
12	3	24	51	57	215	0.53
10	3	20	56	55	221	0.5
7	4	21	54	51	209	0.49
6	4	18	59	49	216	0.45
5	5	20	57	48	208	0.46
4	6	20	56	46	204	0.45

Table 3.5: FSM Stress range by using traction forces based procedure

3.4. Solid element model

In this section, solid FSM model with weld was built to validate results from shell models. Compared to shell model, there are multiple elements in through-thickness direction. Therefore solid element

model can provide more detailed stress and force distribution along thickness. Traction forces based procedure was used to obtain HS structural stress range in solid model case, the first step is the linearization of nodal force, as the equation in Figure 2.9. After that, With moment equilibrium, scalars in line force vector can be integrated, as following equation:

$$f_{yi} * t_p = \frac{(f_{t,1} + f_{t,2})}{2} * l_1 + \frac{(f_{t,2} + f_{t,3})}{2} * l_2 + ... + \frac{(f_{t,n-1} + f_{tn})}{2} * l_(n-1) \tag{3.5}$$

Where f_t is the line force scalar in through-thickness direction; l_i is the distance between nodes, thus element edge length. The rest of calculation process for membrane and bending stress is same with equation 3.4.

3.4.1. Solid pre-processing

The geometry parameters of solid model followed as information of Bergs's article[6]. The boundary condition and load points are same as shell models. However, the amplitude of load force is set as 50KN in each point and the load range is 400KN, thus the stress range needs to be obtained by multiplying the structural stress by 4. In through-thickness direction, 4 elements at minimum are required in order to have a proper bending description. Therefore element size was set as 3mm in lug plate. Limited by CPU performance, the mesh size in other components in FSM solid model was set as 20mm to decrease the time cost in simulation.

3.4.2. Solid post-processing

The stress distribution is shown in Figure 3.16. It is obvious to see that the HS appears at the same location as as-welded shell model.

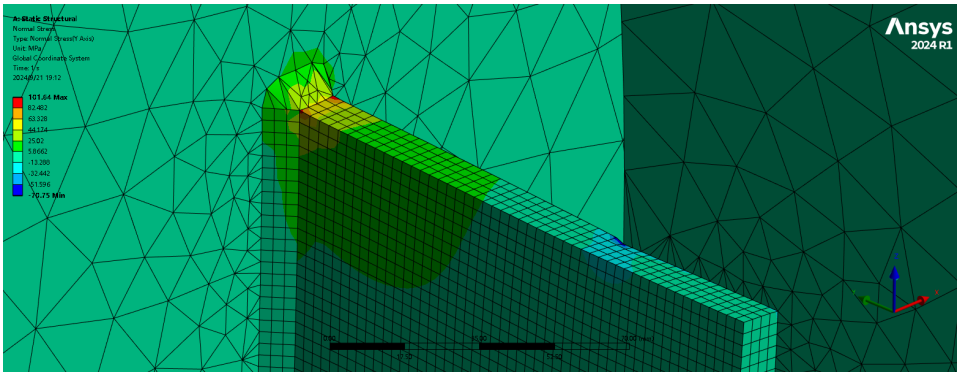

Figure 3.16: FSM solid model stress distribution near HS.

In through-thickness direction(x-direction), nodal forces of all(5) nodes in same row are extracted. In weld seam direction(y-direction), the t'_p is recommended to smaller than 20mm, thus 6 nodes in same column are extracted. After the linearization of nodal forces2.9 and the equivalent substitution3.5 of the linear forces in x-direction, The line force of each row could be obtained, given in table 3.6.

Row number	1	2	3	4	5	6
Z-location	210.55	207.07	203.59	200.12	196.65	193.17
Line force(N)	121.24	116.81	79.33	62.63	51.82	10.29

Table 3.6: FSM solid model line force

Using same process as shell model, the membrane stress σ_m, bending stress σ_b and HS structural stress range $\Delta\sigma_s$ are given as table 3.7.

3.5. Weld modeling aspects

In the case of FSM shell model, the weld modeling decreases HS structural stress range, where the gap in percentage is 7.7%. This is because T-joint in unweld case induce more stress concentration than

σ_m(MPa)	σ_b(MPa)	$\Delta\sigma_s$(MPa)	r_s
25	26	207	0.51

Table 3.7: FSM solid model HS stress range

135-degree joint in the as-welded model. This is verified by comparing bending stress and membrane stress in two cases. The membrane stress in two cases remains almost unchanged, the main difference is in bending stress. Additionally, the stress ranges of solid model, as-weled shell model and Berge's experiment data are very similar, this demonstrates the applicability of building inclined welds in shell model for FSM.

4

Stiffener-plate model details

This chapter focuses on the FEM modeling and results of stiffener-plate planar model. According to different positions of cope holes and vertical intersecting plates, the types of models are divided into specimen 1 and specimen 2. Specimen 1 has four varieties of cope hole radii R, which are 25mm, 30mm, 35mm, and 40mm. Specimen 2 has six varieties of cope hole radii, which are 25mm, 30mm, 35mm, 40mm, 45mm, and 50mm. Intersecting plates are inserted perpendicular to the web to simulate cross girders. The general geometry(unwelded) in ANSYS is given as following figures 4.1 and 4.2, material properties and dimensions are given as figure 2.27 and 2.28. In this chapter, hot spot structural ranges are obtained by using traction forces based procedure.

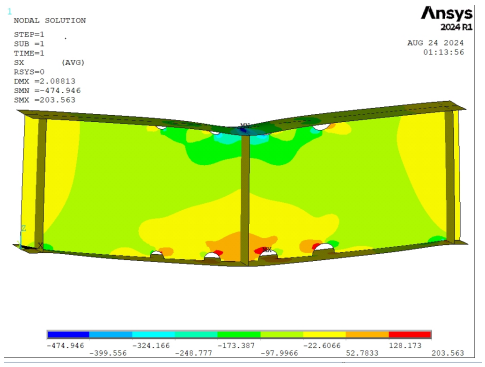

Figure 4.1: Specimen 1 geometry

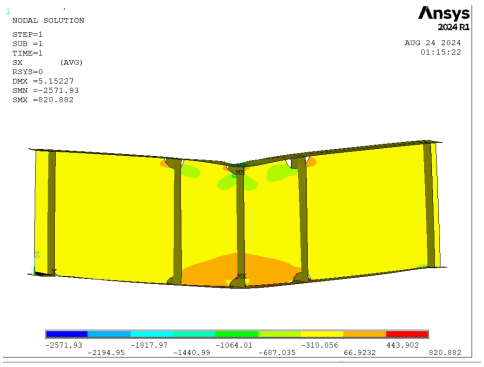

Figure 4.2: Specimen 2 geometry

4.1. Hot spot type modeling

For SPM models, two types of weld shapes are investigated. Weld type A includes boxing weld at the seam end, weld type B does not have it. The weld angle is 45 degrees and the throat thickness is 5mm. In shell element model, it was implemented by setting weld leg length as 12.5mm and thickness of 10mm. This approach results in inaccurate stresses in the root case, due to the coinciding section between weld seam and plate. However, this does not affect the weld toe, which is feasible in current research. In solid model, Welds can be built according to the experiment's data. Two types of weld shape in shell and solid model are illustrated in Figures 4.3,4.4,4.5,4.6 below.

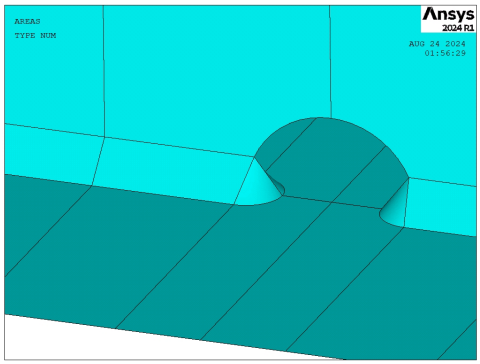

Figure 4.3: Type A weld in shell element model

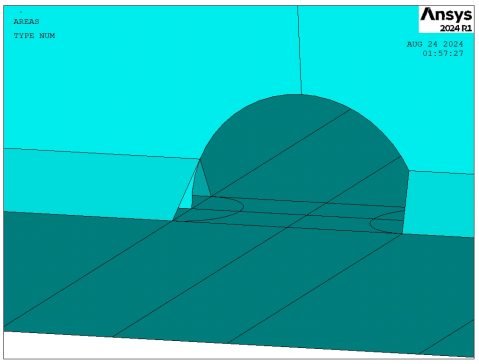

Figure 4.4: Type B weld in shell element model

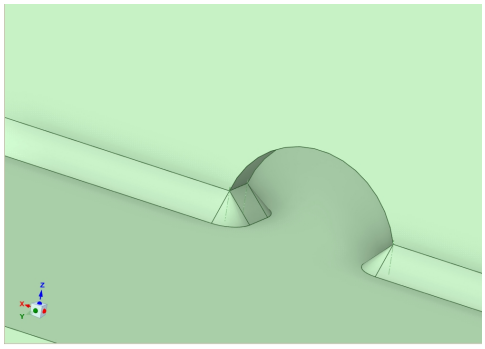

Figure 4.5: Type A weld in solid element model

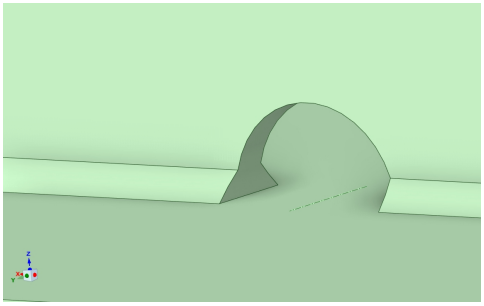

Figure 4.6: Type B weld in solid element model

4.2. Crack locations

For specimen 1 and specimen 2, fatigue cracks appear at different place, depending on weld type. With specimen 1, the cracks all occurs at weld toe outsides, which are away from loading point at the flange plate inside cope holes, as Figure 4.7. In Miki's experiment, cracks are observed at both the top and bottom side flanges. The cracks propagate along the verticle direction of the weld seam. Current research focuses on tension case , because the highest stress occurs at hot spots. Therefore only HS at bottom will be investigated.

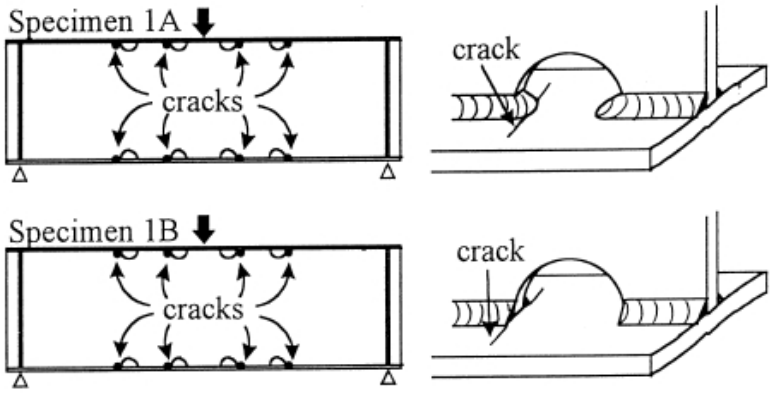

Figure 4.7: Crack occurs in specimen 1[31]

With Specimen 2A, cracks were observed at the web from weld toe with intersecting plate of tension side cope hole(R30), which grows along the parallel direction of the weld seam. With specimen 2B,

crack was observed at tension side cope holes(R40, R45, R50). Similar to specimen 1, cracks initiated at weld toe in flange and propagate in vertical direction of weld seam, as Figure 4.8

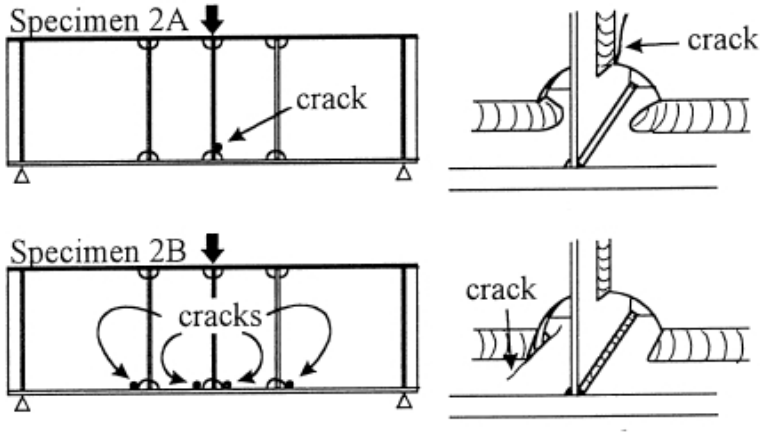

Figure 4.8: Crack occurs in specimen 2[31]

In specimen 1A, specimen 1B, and specimen 2B, the notches appear at the weld toe end are and perpendicular to the weld seam, which are HS type A. With specimen 2A, the notch appears at the weld toe end and parallel to the weld seam, which is HS type B.

4.3. Shell element model

This section includes shell model aspects and stress range calculation of SPM specimen 1 and specimen 2, as well as structural stress range calculation. According to various specimens and various weld model types, the investigation of HS and stress ranges are divided into six categories, which are specimen 1 with weld type A(S1A); specimen 1 with weld type B(S1B); specimen 1 unwelded(S1UW); specimen 2 with weld type A(S2A); specimen 2 with weld type B(S2B); specimen 2 unwelded(S2UW). Because the load condition is a three-point bending load, structural stress has different orientations depending on the cope hole locations. For comparison amplitudes, the stresses are presented as final absolute values.

Boundary condition and load To ensure that the investigating HS is located at the tension side, two kinds of boundary conditions and loads will be set according to different cases. For specimen 1, the cope holes are symmetrically distributed in the upper and lower flanges. Thus only one boundary and load mode is required, as Figure 4.9. In FEM, the amplitude of the load is set as 50KN which is applied at each node along the load line. A linear force of 450 KN was applied in the experiment. Therefore structural stress range $\Delta\sigma_s$ could be obtained with equation 4.1. Where n_{load} is the number of nodes in the applied load line.

$$\Delta\sigma_s = \frac{\sigma_s * 450}{50 * n_{load}} \tag{4.1}$$

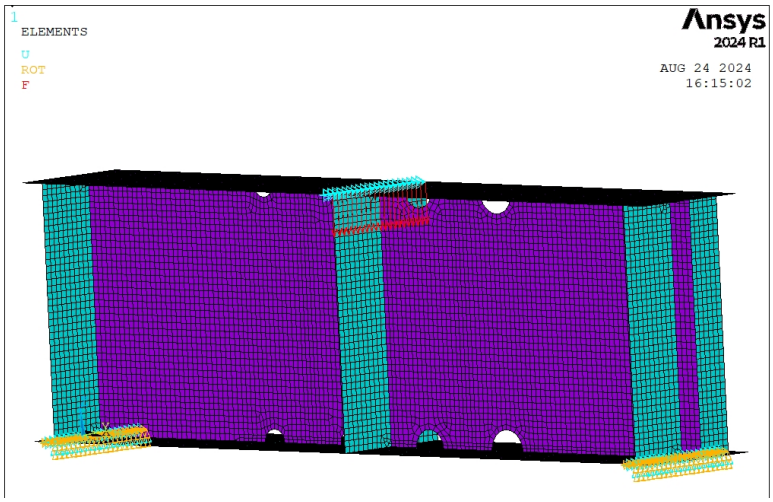

Figure 4.9: Specimen 1 boundary condition and load

For specimen 2, crack occurs at various positions depending on different weld types. In S2A the crack was observed at the weld toe near cope hole R30 in the intersecting plate. BC and load are applied the same as specimen 1, as Figure 4.10.

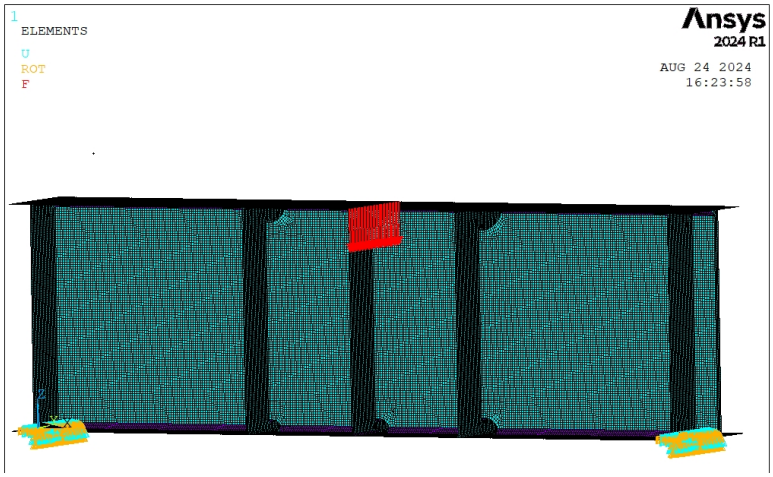

Figure 4.10: Specimen 2A boundary condition and load

When it comes to specimen 2A, cracks were observed at the upper flange near cope holes R40, R45, and R50. The line load is applied at the middle of bottom flange, and constraints are applied at side of top flange, as Figure 4.11. The amplitude of load is same as that in specimen 1. In the case of specimen 2 unwelded, two loading modes will be applied separately to compare the magnitude of the structural stress range at different hot spots.

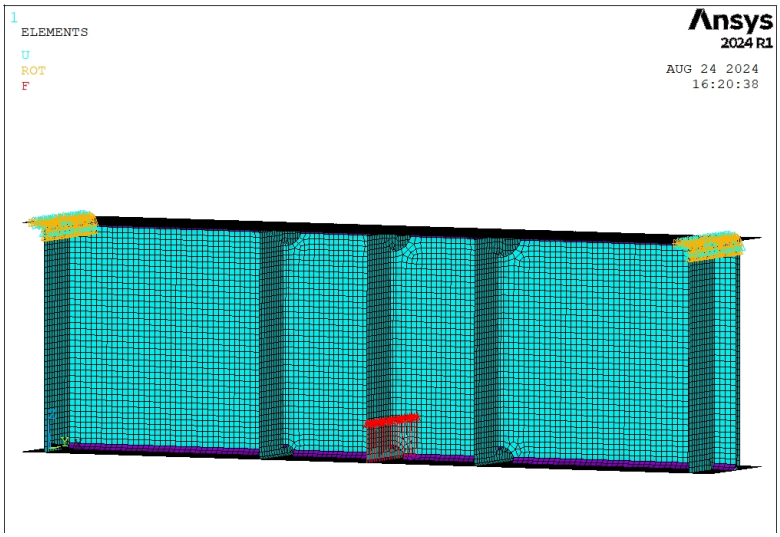

Figure 4.11: Specimen 2B boundary condition and load

4.3.1. Specimen 1 with weld type A

As figure 4.7, the crack is perpendicular to the weld seam. The HS is type A here. In this case, the weld seam is continuous, which refers to a line formed by weld toe nodes along the weld direction. This could be approximately described as a continuous curve in a shell element model[12], as Figure 4.12.

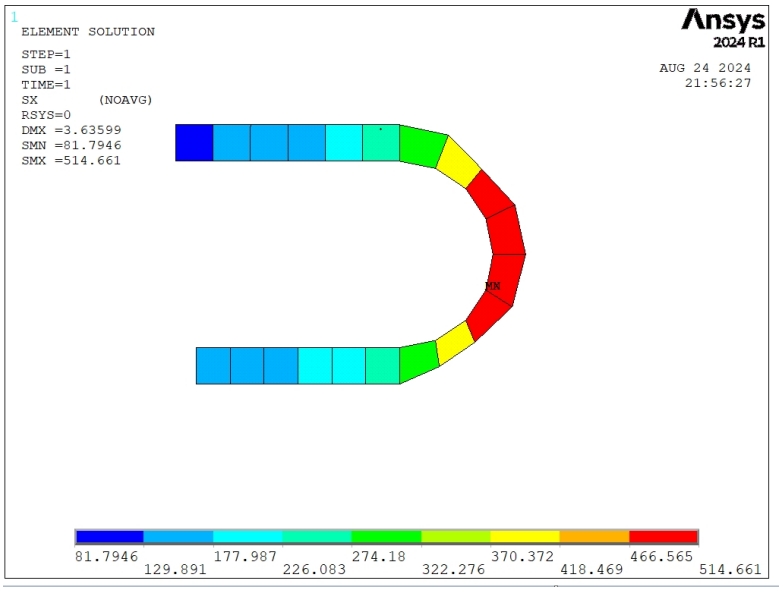

Figure 4.12: Elements and nodes at weld toes

Within the case of displacement-based FEM, the most accurate solution quantities is nodal force and nodal moments in the shell element model. For continuous weld, nodes along the weld toe are used to extract nodal forces and moments from FEM post-processing in the global coordinate system(x,y,z). Then nodal force/moment vector should be rotating along the weld seam onto local coordinate system(x',y',z'), as Figure 2.8. The rotation of nodal force is implemented with the equation in Figure 4.13.

$$\begin{Bmatrix} F_x{}' \\ F_y{}' \end{Bmatrix} = \begin{bmatrix} \cos(\alpha) & -\sin(\alpha) \\ \sin(\alpha) & \cos(\alpha) \end{bmatrix} \begin{Bmatrix} F_x \\ F_y \end{Bmatrix}$$

Figure 4.13: Nodal force rotation

Where F_x and F_y are the nodal force component in global system x and y direction; F'_x and F'_y are the nodal force component in local system x' and y' direction; α is the angle between x-axis and element edge at weld seam toe. Within the work equivalent between nodal force and line force at same node, the line force in local coordinate system could be converted from normal component nodal force(perpendicular to weld seam) by using the equation in Figure 2.9. Note that the force and moment should use the summation of contribution from adjacent elements. According to the right-hand principle, moment in the y-direction should be used with force in the x-direction together, or vice versa(if in the x-y plane). In consequence, membrane stress and bending stress could be obtained with local line forces and line loads, as functions 4.2 and 4.3.

$$\sigma_m = \frac{f_{x'}}{t_p} \tag{4.2}$$

$$\sigma_b = \frac{6m_{y'}}{{t_p}^2} \tag{4.3}$$

By using the method above, σ_m and σ_b can be obtained with the nodal force extracted and global coordinate position from FEM. Stress distribution near HS is shown in Figure 4.14. Elements size are set as 5mm, n_{load} is 55 in S1A. For HS structural stress at different cope holes, the decomposition of resultant nodal force in tangent orientation and normal orientation are illustrated in Figures 4.15, 4.16, 4.17, 4.18 below:

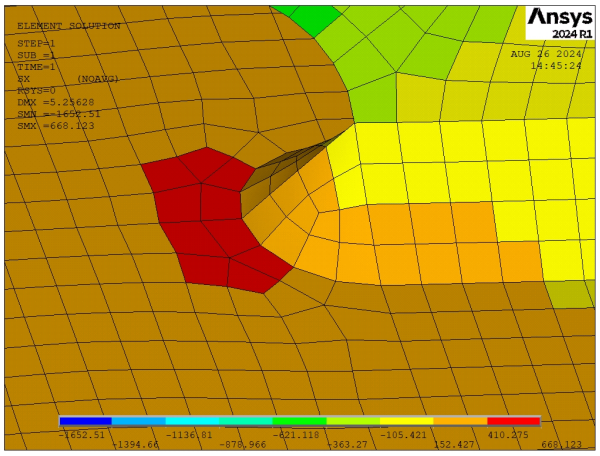

Figure 4.14: Stress distribution in S1A HS

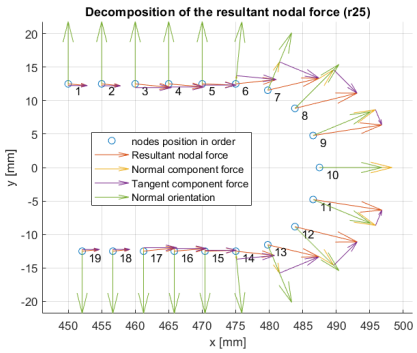

Figure 4.15: Force decomposition R25

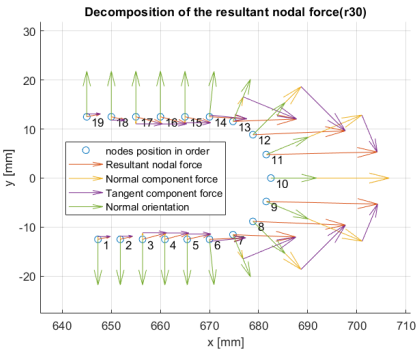

Figure 4.16: Force decomposition R30

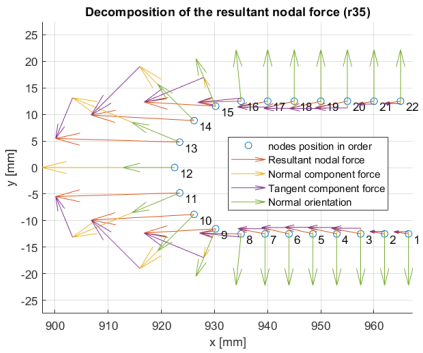

Figure 4.17: Force decomposition R35

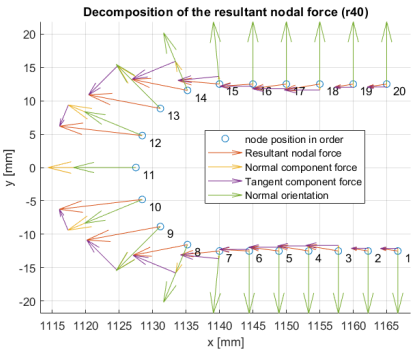

Figure 4.18: Force decomposition R40

From the illustration of resultant force decomposition, we can see that the highest structural stress in normal orientation appears at the tip of weld end, which is the location of HS type A. Membrane stress σ_m, bending stress σ_b, and summation σ_s along the distance of weld toe are given in Figures 4.19, 4.20, 4.21, 4.22 below.

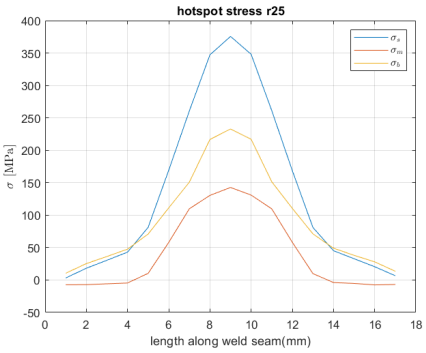

Figure 4.19: Structural stress R25

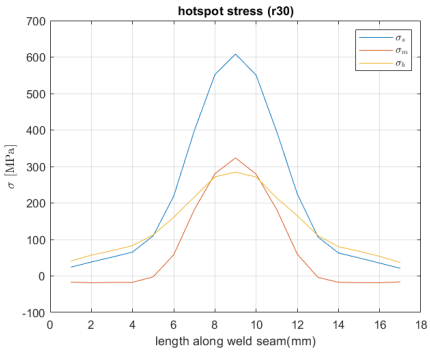

Figure 4.20: Structural stress R30

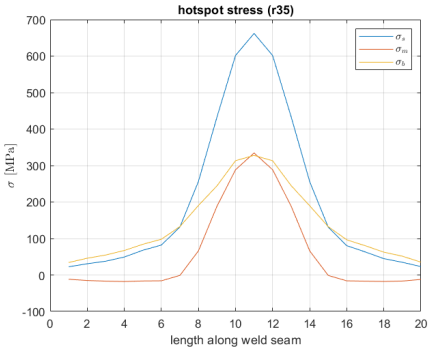

Figure 4.21: Structural stress R35

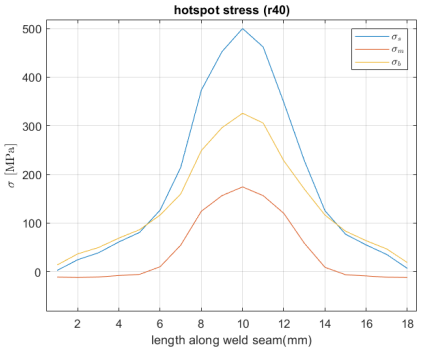

Figure 4.22: Structural stress R40

The amplitude of highest structural stress and stress ratio are listed in table 4.1 below:

HS type A position	σ_m(MPa)	σ_b(MPa)	σ_s(MPa)	$\Delta\sigma_s$(MPa)	Stress ratio r_s
R25	143	233	376	61	0.62
R30	324	285	608	100	0.47
R35	334	328	662	108	0.49
R40	174	326	500	82	0.65

Table 4.1: SPM S1A shell model structural stress

The highest HS structural stress occurs at R35, and descending in order are R30, R40, R25, which shows similar trend as the experimental data from Miki's experimental data as Figure 4.23 below, obtained by using the surface extrapolation method. Generally, the result from this method will be overestimated. Thus results in table 4.1 could be considered as reasonable.

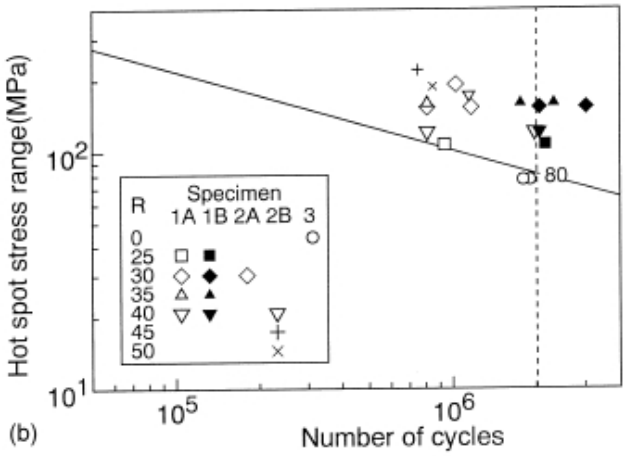

Figure 4.23: Miki's experimental HS stress range.[31]

In order to further validate the correctness of the shell model, amplitude of first principle stress are measured at same nodes along the weld toe, as Figures 4.24, 4.25, 4.26, 4.27. The first principle stress at compression and tension side shows symmetrical values at each side of weld seam toe. The amplitudes of tension side are also similar to HS structural stress.

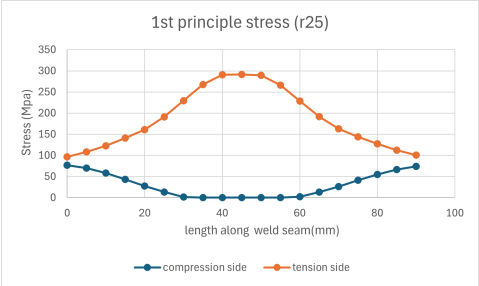

Figure 4.24: First principle stress R25

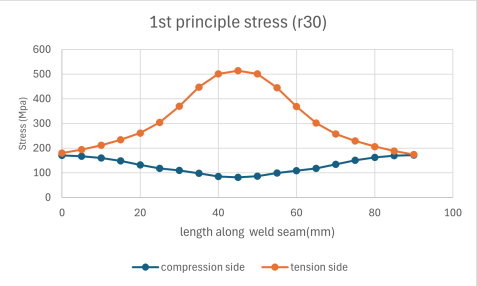

Figure 4.25: First principle stress R30

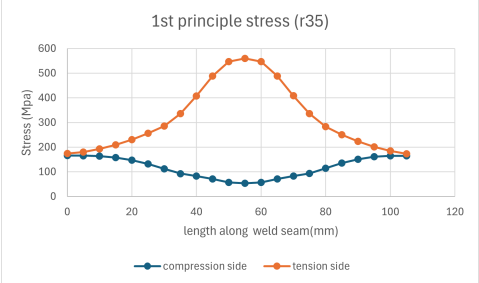

Figure 4.26: First principle stress R35

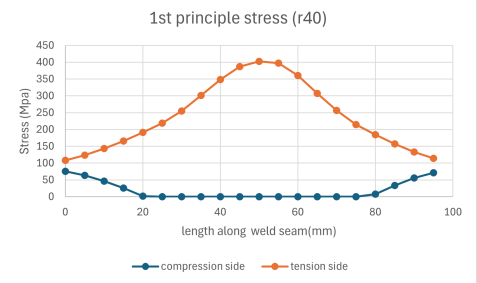

Figure 4.27: First principle stress R40

4.3.2. Specimen 1 with weld type B

Weld type B did not provide a continuous weld seam. There is a sharp corner at the weld end. Therefore the continuous linearization method in S1A is not applicable in S1B. In dealing with the sharp weld corner effect in this case, the virtual node method[13] could be applied here. Two reference lengths from weld end are designed as L_1 and L. The L_1 is the distance from weld end to the end to the virtual node. The position of the virtual node is at the attachment between weld seam and bottom plate. As figure 4.30, the distance between black point and verticle mid plane indicates L and red point indicates virtual node. In this research the failure of LSS is considered as when the crack fully grows at through-thickness direction, thus L_1 was defined as:

$$L_1 = \frac{t_w}{2} + l_w = 4.5mm + 7.07mm \tag{4.4}$$

Where t_W is the thickness of the vertical web and l_w is the weld leg length, thus $L_!$ is 9.5mm. The parameter L serves as an integration interval in enforcing equilibrium conditions for edge tractions along the weld toe line from weld end to a distance measured by L[13]. In order to simplify the calculation, L is set to same as coarse mesh size. Limited by the modeling of the weld, element size was set as 12.5mm here. F_1 is the nodal force perpendicular to weld at weld end and F_2 is the nodal force at a distance of L from weld end. The illustration is given in Figure 4.28. The effect on the overall structural stress calculations along L is considered. Using the following equation 4.5 the equivalent converting between nodal force and line force can be implemented. The corresponding line moment at the same position can be calculated in the same way. The calculation process for σ_m and σ_b are same as equation 4.2 and 4.3.

$$f = \frac{F_1 * (L_1 + L) + F_2 * (L_1 - L)}{L_1 * L} \tag{4.5}$$

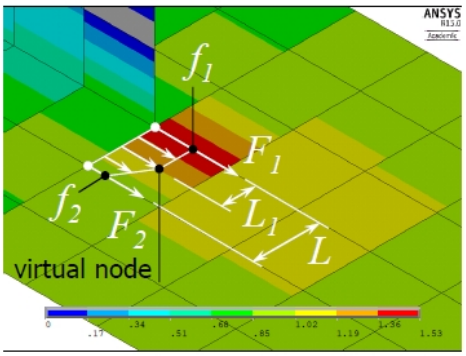

Figure 4.28: Virtual Node method illustration.[19]

Compared to the reference specimen in figure 4.28, S1B and S2B contain straight weld seams, and the reference virtual node position is also different. To ensure the accuracy of results, structural stresses evaluated at both sides are averaged. Stress distribution near HS is shown in Figure 4.29. Within the virtual node method, Hs structural stress at four various cope holes are listed as table 4.2 below. Element size was set as 12.5mm, n_{load} is 21.

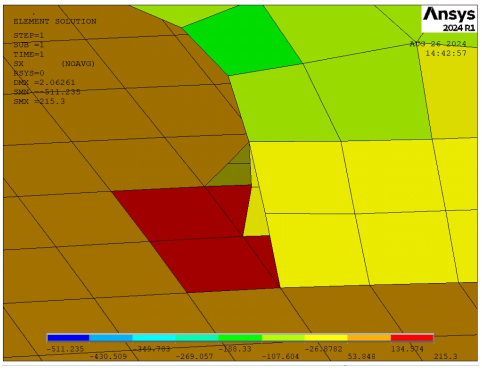

Figure 4.29: Stress distribution in S1B HS

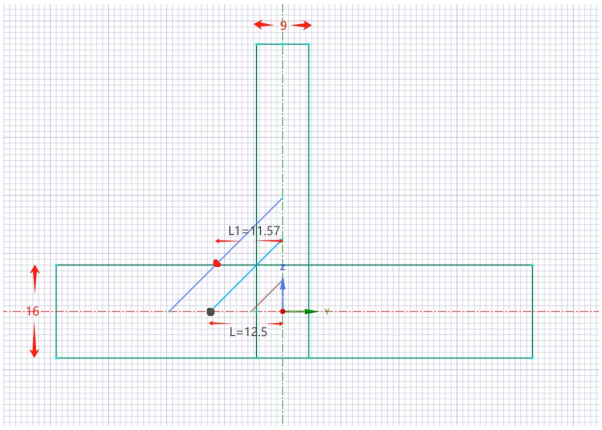

Figure 4.30: Type B weld virtual node

HS type A position	σ_m(Mpa)	σ_b(Mpa)	σ_s(Mpa)	$\Delta\sigma_s$(Mpa)	Stress ratio r_s
R25	106.73	124.88	231.61	99.40	0.54
R30	220.95	127.76	348.71	149.66	0.37
R35	229.50	160.89	390.39	167.55	0.41
R40	120.76	182.06	302.82	129.97	0.60

Table 4.2: SPM S1B shell model structural stress

For specimen 2B, the stress range shows the same trend as experimental data and that in S1A. The value in S1B is considerably higher than in S1A. This may be because the curved weld end in S1A provides a smoother geometry transition.

4.3.3. Specimen 1 without weld

To validate the weld modeling influence of structural stress, specimen 1 shell model without weld is investigated in this subsection. Because the sharp geometry discontinuity exists at the joint, the virtual node method is used here similar to S1B. However, there is no straight weld seam located at the joint between the web and flange. Attachment(virtual node) is now directly located at the plate joint. The definition of L_1 should be changed to half of the web thickness, which is 4.5mm, as figure 4.32. The position of nodal force extracting and the rest of the calculation process is the same in subsection 4.3.2.

Element size is set as 12.5mm similarly. The structural stress and stress ratio of unwelded specimen 1 are given in table 4.3. Stress distribution near HS is shown in Figure 4.31.

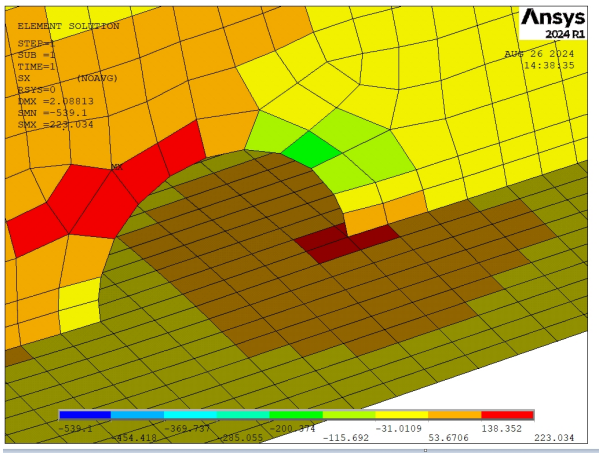

Figure 4.31: Stress distribution in S1UW HS

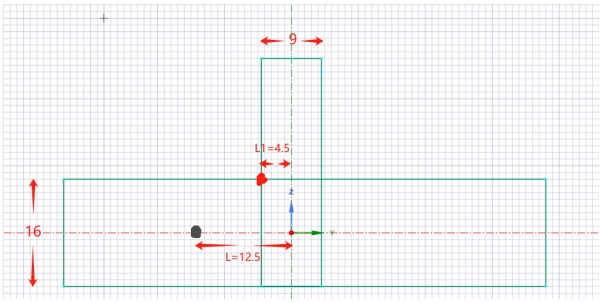

Figure 4.32: Unweld model virtual node

HS type A position	σ_m(MPa)	σ_b(MPa)	σ_s(MPa)	$\Delta\sigma_s$(MPa)	Stress ratio r_s
R25	174	160	334	143	0.48
R30	274	153	426	183	0.36
R35	289	191	480	206	0.40
R40	191	221	411	177	0.54

Table 4.3: SPM S1UW shell model structural stress

Stress range in the unwelded shell model of specimen 1 is significantly higher that in S1A and S1B in each cole hole. The stress ratio r_s in S1UW is similar to that in S1B, which are lower than S1A. This is probably because the geometry difference in the weld end varies the stress distribution. The comparison of stress range in three weld modeling cases are given in Figure 4.33.

Figure 4.33: Stress range comparison of specimen 1.

4.3.4. Specimen 2 with weld type A

In specimen 2A, the crack occurs not at the flange anymore, but at weld toe in vertical web. Hot spot is defined as type B here, because the crack is parallel to the weld seam. Therefore the method to obtain HS structural stress is the same as FSM, in section 3.3.4. Element size is set as 5mm and the n_load is 51. Four nodes are included into account, t'_p is 14mm, as illustrated in Figure 4.34. The stress range and stress ratio are given in table 4.4.

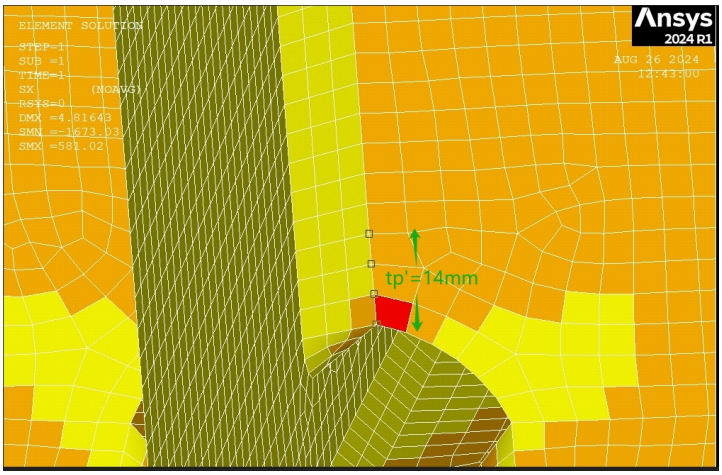

Figure 4.34: Specimen 2A HS.

HS type B position	σ_m(MPa)	σ_b(MPa)	σ_s(MPa)	$\Delta\sigma_s$(MPa)	Stress ratio r_s
R30	300	411	711	125	0.58

Table 4.4: SPM S2A shell model structural stress

4.3.5. Specimen 2 with weld type B

In specimen 2B, fatigue crack occurs at the top flange tension side(R40,R45,R50), as figure 4.8. Different from specimen 1 and specimen 2A, the line load is applied at the mid of the bottom flange outer edge. Boundary conditions are constrained at sides of top flange outer edge, as shown in Figure 4.11. In specimen 2B, the geometry discontinuity at weld end is sharply changed, which is similar to specimen 1B. Virtual node method as introduced in subsection 4.3.2 is applicable for S2B. Web thickness and weld length are the same as in specimen 1. Therefore L_1, L, element size, and n_{load} are same as

in specimen 1. Stress distribution near HS is shown in Figure 4.35. Stress range and stress ratio are listed as table 4.5 below:

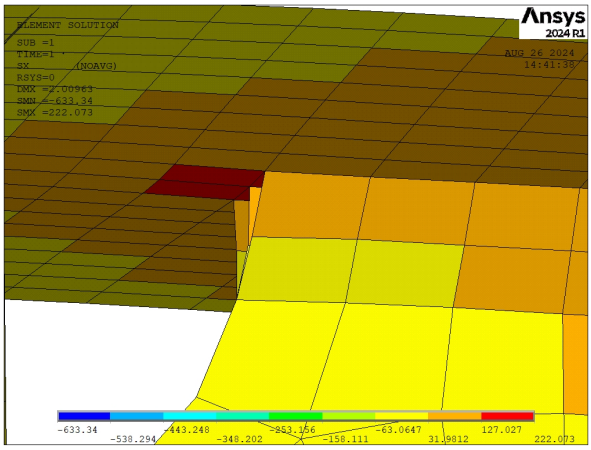

Figure 4.35: Stress distribution in S2B HS

HS type A position	σ_m(MPa)	σ_b(MPa)	σ_s(MPa)	$\Delta\sigma_s$(MPa)	Stress ratio r_s
R40	134	142	277	119	0.51
R45(left)	256	125	382	164	0.33
R45(right)	259	135	394	169	0.34
R50	142	181	323	139	0.56

Table 4.5: SPM S2B shell model structural stress

Structural stress still varies from the distance to the load line and cope hole size. The structural stress becomes larger when the position is closer to load line. At the same distance, a larger cope hole size results in a larger structural stress. In s2B, highest structural stress occurs at R45, the value on the right side is slightly higher than on the left side. Compared to HS type B in S2A, structural stress iN S2B R45 is significantly higher.

4.3.6. Specimen 2 without weld

The investigation of unwelded specimen 2 was not included in Miki's experiment. The location of the crack does not determine the exact location. Hence both hot spot types in specimen 2A and specimen 2B are investigated in this subsection. For HS type B(S2A), stress range at R30 is evaluated; for HS type A(S2B), stress ranges at R40, R45, and R50 are evaluated. Stress distribution of S2UW near two types of HS are shown in Figures 4.37 and 4.37.

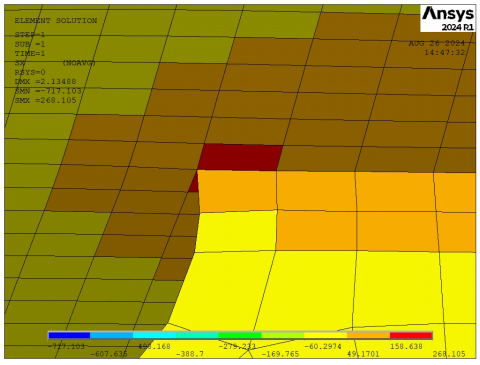

Figure 4.36: Stress distribution in S2UW type A HS

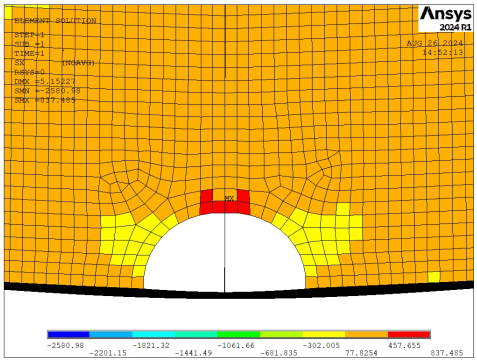

Figure 4.37: Stress distribution in S2UW type B HS

HS type B Due to no weld is modeled in S2UW, the reference nodes for HS type B stress range calculating are located at the joint of web and intersecting plate. Contributes of nodal force from elements on the left and right sides are extracted separately, and structural stress will be calculated separately. Element size was set as 5mm, n_{load} is 51. Four reference nodes are included to take into account. The parameter t_p' is 18.18mm, which is obtained by the z-coordinate value of the top reference node subtracted from that of the bottom reference node. Structural stress and stress ratio of HS type B are given in the table 4.6 below:

HS type B position	σ_m(MPa)	σ_b(MPa)	σ_s(MPa)	$\Delta\sigma_s$(MPa)	Stress ratio r_s
R30(Right side contribute)	395	557	952	167	0.59
R30(Left side contribute)	392	543	935	165	0.58

Table 4.6: SPM S2UW HS type B shell model structural stress

Structural stress range and stress ratio are barely the same between R30 Right and R30 Left. Compared to the results from S2B, S2UW is significantly higher.

HS type A HS type A at R40, R45, and R50 are also investigated in this subsection. In this case, the geometry discontinuity at joint is similar to S1UW, the virtual node method is applied. The parameter L_1 is 4.5mm. The element size was set as 12.5mm and n_{load} is 21. Stress range and stress ratio are given in the table 4.7. Gap between as weld shell model and the unwelded model for different HS is shown in Figure 4.38.

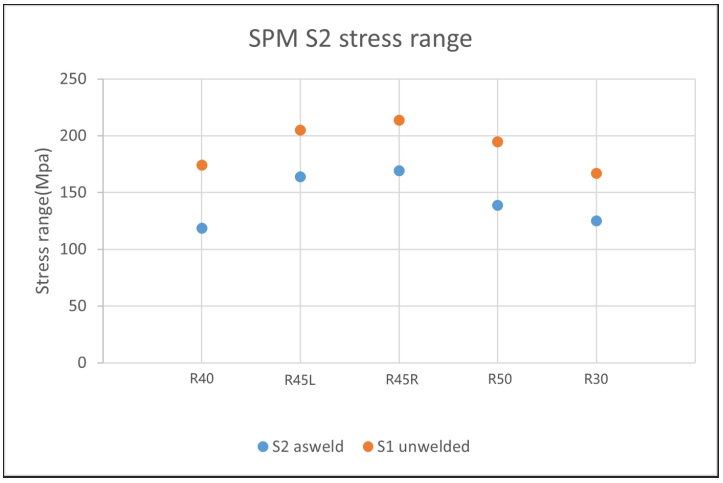

Figure 4.38: Stress range comparison of specimen 2.

HS type A position	σ_m(MPa)	σ_b(MPa)	σ_s(MPa)	$\Delta\sigma_s$(MPa)	Stress ratio r_s
R40	203	203	406	174	0.50
R45(left)	176	301	477	205	0.37
R45(right)	190	307	498	214	0.38
R50	212	241	453	195	0.53

Table 4.7: SPM S2UW HS type A shell model structural stress

4.4. Weld modeling influence

From the results in the section 4.3, it is obvious that in every case structural stress in the unwelded shell model is significantly higher than in the as weld model. In specimen 1 the influence of two different weld types to HS type A at flange is investigated. This effect is eventually reflected in the structural stress

range. Weld type B results in higher structural stress than weld type A. The table 4.8 below shows the percentage difference in the values of stress range for S1 shell models with different types of weld.

HS type A	S1Aσ_s(MPa)	S1Bσ_s(MPa)	S1UWσ_s(MPa)	S1A S1UW gap	S1B S1UW gap
R25	62	99	143	57%	30.7%
R30	100	150	183	45.6%	18.2%
R35	108	168	206	47.4%	18.6%
R40	82	130	177	53.7%	26.4%

Table 4.8: Stress range value gap for specimen 1

Based on the stress range value of unwelded model, the value of S1A is reduced by 45.6% to 57%; the value of S1B is reduced by 18.2% to 30.7% depending on the HS position. In the case of a smaller cope hole size and farther distance from the load point, the gap will be greater.

For specimen 2, the investigation mainly focuses on the stress range gap in different HS types. Stress ranges in the unwelded model are also much higher than in the as-welded model. The stress range gap in percentage for S2 is given in tables 4.10 and 4.9.

HS type B	S2Aσ_s(MPa)	S2UWσ_s(MPa)	S2A S2UW gap
R30	125	167	26.4%

Table 4.9: Stress range value gap for specimen 2 HS type B

HS type A	S2Bσ_s(MPa)	S2UWσ_s(MPa)	S2B S2UW gap
R40	119	174	30.0%
R45 left	164	205	20.0%
R45 right	169	214	20.7%
R50	139	195	28.7%

Table 4.10: Stress range value gap for specimen 2 HS type A

The stress range of S2B is reduced by 20% to 30% from S2UW, which is similar to the gap between S1B and S1UW. Similarly, higher stress range gap occurs at smaller cope size and farther distance from load point case. For HS type B of S2A, the gap is 26.4%. In the stiffener-plate model including cope holes, the difference is significant in aswelded model and unwelded model for structural stress results. Generally, the stress range in unwelded model is higher than unwelded model, this provides safety redundancy in industrial computing. However, if accurate results are required, it is recommended to build weld in the shell model to avoid overestimating the stress range.

4.5. Solid element model

In order to validate the accuracy of shell model results, solid models of SPM are also investigated. The weld throat length is set as 5mm, which is the same as Miki's experiment. The applied load and boundary condition are the same as in shell model. Loading amplitude was set as 50KN that evenly distributed along weld line, thus the stress range could be obtained by multiplying the structural stress by 9.

4.5.1. Specimen 1 solid model

Type A HS in solid case could be considered as type B HS in shell case, because their shape in the section is the same, as the illustration in Figure 4.39. Membrane stress σ_m and bending stress σ_b are obtained by equations 4.6 and 4.7. Where f_{xi} is the nodal force in unit width, obtained by F_{xi} divide element edge length δ. In solid model, five nodes in through-thickness direction are sufficient to describe the bending stress, hence element size was set as 4mm in the critical area.

$$\sigma_m = \frac{\sum f_{xi}}{t_p}, f_{xi} = \frac{F_{xi}}{\delta} \tag{4.6}$$

$$\sigma_s = \frac{6 * (\sum (f_{xi} * z_i) - \sigma_m * \frac{{t_p}^2}{2})}{{t_p}^2} \tag{4.7}$$

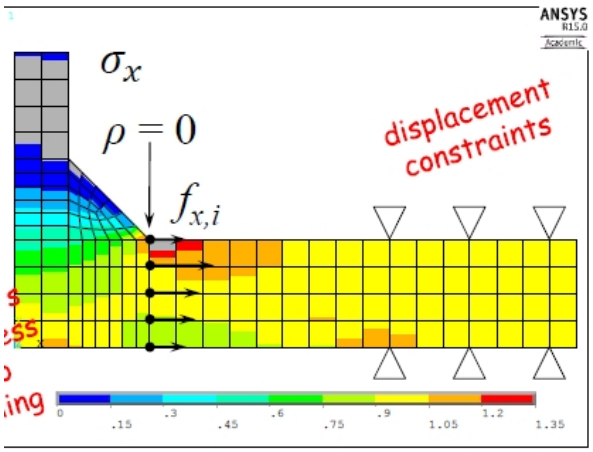

Figure 4.39: Type A HS illustration in solid model[19].

The stress distribution of S1A and S1B solid model are shown in Figures 4.40 and 4.2. Structural stress and stress ratio are given in tables 4.11 and 4.12.

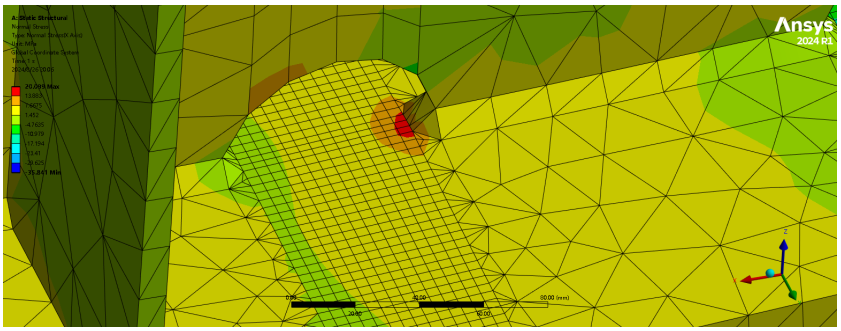

Figure 4.40: SPM S1A solid model stress distribution near HS.

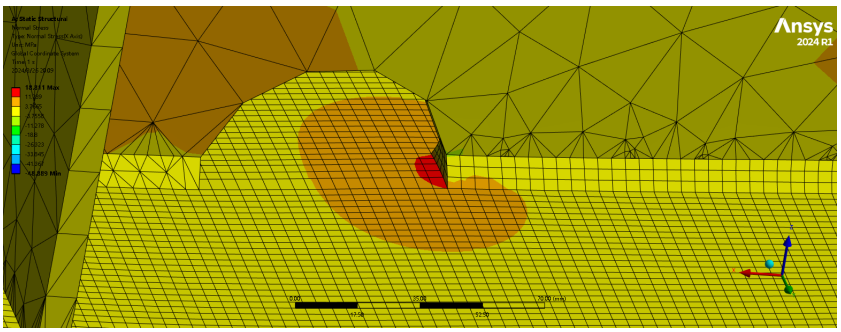

Figure 4.41: SPM S1B solid model stress distribution near HS.

HS type A position	σ_m(MPa)	σ_b(MPa)	σ_s(MPa)	$\Delta\sigma_s$(MPa)	Stress ratio r_s
R25	3	6	9	78	0.69
R30	5	7	12	108	0.55
R35	5	8	13	118	0.59
R40	3	7	10	89	0.73

Table 4.11: SPM S1A solid model structural stress

HS type A position	σ_m(MPa)	σ_b(MPa)	σ_s(MPa)	$\Delta\sigma_s$(MPa)	Stress ratio r_s
R25	4	7	11	98	0.67
R30	8	9	16	148	0.54
R35	8	10	18	164	0.57
R40	5	10	15	132	0.69

Table 4.12: SPM S1B solid model structural stress

4.5.2. Specimen 2 solid model

S2A solid model HS in Specimen 2A is type B, which means that the method to evaluate structural stress should be the same as FSM in section 3.4. First, the nodal forces in through-thickness direction is linearized by using converting matrix in figure 2.9. Then the scales in line force vector can be integrated with moment equilibrium, as equation 3.5. Finally, membrane stress and bending stress can be obtained with equations 3.3 and 3.4. Element size was set as 2.25mm to ensure 5 nodes occur at the web in through-thickness direction. In verticle direction(z-direction), 5 nodes are included, thus t_p' is 10.3mm. Stress distribution and structural stress is given in Figure 4.42 and table 4.13.

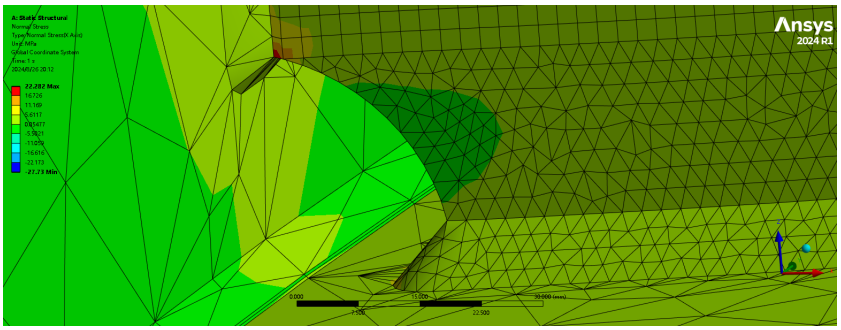

Figure 4.42: SPM S2A solid model stress distribution near HS.

HS type B position	σ_m(MPa)	σ_b(MPa)	σ_s(MPa)	$\Delta\sigma_s$(MPa)	Stress ratio r_s
R30	6	7	12	111	0.53

Table 4.13: SPM S2A solid model structural stress

S2B solid model The method to obtain S2B solid model structural stress is the same as in S1B solid model. Stress distribution and structural stress in different cope hole is given as Figure 4.43 and table 4.14.

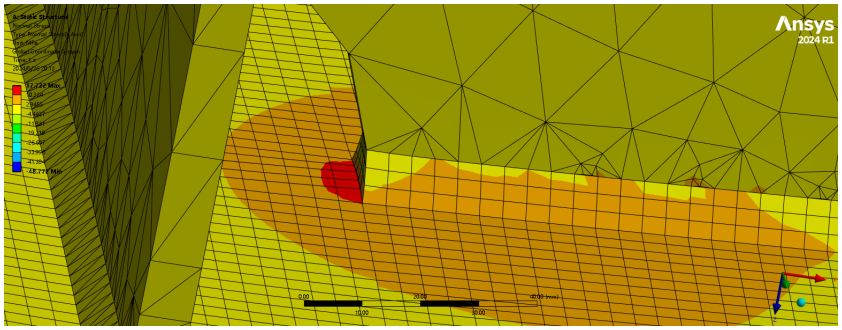

Figure 4.43: SPM S2B solid model stress distribution near HS.

HS type A position	σ_m(MPa)	σ_b(MPa)	σ_s(MPa)	$\Delta\sigma_s$(MPa)	Stress ratio r_s
R40	5	9	13	119	0.65
R45l	8	8	17	152	0.50
R45r	8	9	18	158	0.51
R50	5	10	15	132	0.67

Table 4.14: SPM S2B solid model structural stress

4.6. Differences between shell and solid model results

The deviation research between shell and solid model is investigated in this section. The comparison of HS structural stress are given in scatter plots below. Figure 4.44 and 4.45 shows the stress range deviation between shell model and solid model in specimen 1A and specimen 1B; 4.46 shows the deviation in specimen 2, where r40-r50 correspond to HS type A and r30 correspond to HS type B.

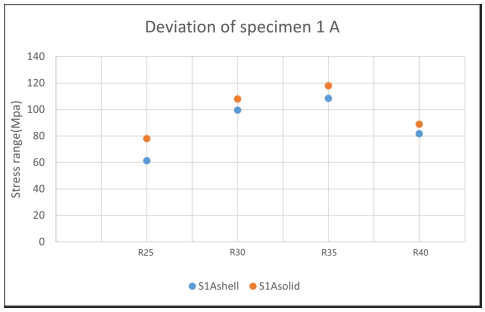

Figure 4.44: Deviation of specimen 1A

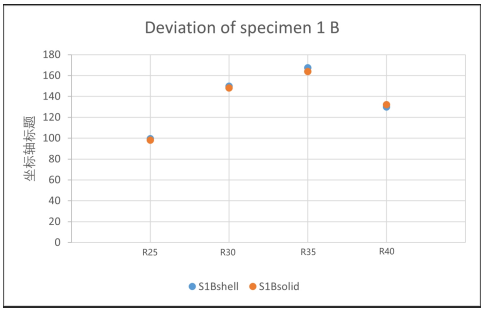

Figure 4.45: Deviation of specimen 1B

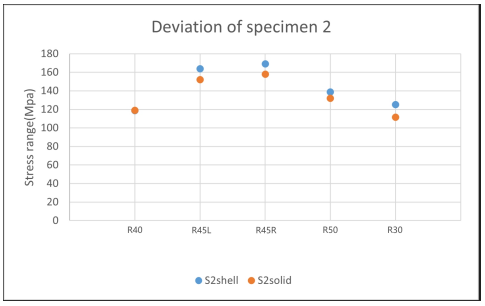

Figure 4.46: Deviation of specimen 2

As can be seen from the plots, stress range deviation in both type B weld case is very small. But in weld type A case, the deviation becomes larger. There could be two reasons for this phenomenon.

First is because the irregular mesh was generated in type A weld. Triangular cone-shaped elements exist at type A weld, which induced inaccurate output nodal force. The second possible reason is the overlapping section existing at the flange and web in the shell element model when modeling the weld seam. The coinciding section induces higher material stiffness near the weld root, which could influence the result from the weld toe. For the first, better better-performing processor(e.g.DelftBlue) is required to do the global(not only in critical areas) mesh refining of the LSS. For the second case, the improving method of weld modeling can be used in shell element model, for instance, rigid bar connection method. Using rigid bar to connect the inclined weld element and the plate elements can avoids the appearance of overlapping elements, which provides accurate material stiffness at weld root. The eroor in percentage for each investigated HS is given in the table 4.15 below.

HS position	HS type	Weld type	Shell σ_s(MPa)	Solid σ_s(MPa)	Error
R25	A	S1A	61	78	21.2%
R30	A	S1A	100	108	7.9%
R35	A	S1A	108	118	8.2%
R40	A	S1A	82	89	8.1%
R25	A	S1B	99	98	-1.4%
R30	A	S1B	150	148	-1.1%
R35	A	S1B	168	164	-2.1%
R40	A	S1B	130	132	1.5%
R30	B	S2A	125	112	-12.1%
R40	A	S2B	119	119	-0.2%
R45l	A	S2B	163	152	-7.7%
R45r	A	S2B	169	158	-7.1%
R50	A	S2B	139	132	-5.0%

Table 4.15: SPM stress range deviation between solid and shell model

5

Fatigue similarity validation

In this chapter, effective notch stress of LSS is investigated. With respect to two kinds weld shape, weld load carrying stress coefficient C_{bw} are evaluated separately. After that, the fatigue failure criteria of SSS and LSS are discussed, in order to approximate the LSS lifetime. In consequence, LSS fatigue data was substituted into SSS scatter band. The fatigue similarity is validated.

5.1. Effective notch stress range

Through-thickness stress weld notch stress distribution is typically defined as three zones, which are:

- Zone 1: Peak stress
- Zone 2: Notch affected stress gradient
- Zone 3: Far-field dominated stress

Nominal stress concept and HS structural stress have lack of measurements in Zone 1. The effective notch stress includes partial zone 1, 2, and 3 information. The notch stress refers to the non-linear stress distribution that occurs along the direction of a surface notch due to changes in geometry. ESSC based on the averaged notch stress in micro- and meso-structural length $\rho*$.

Non-linear notch stress distribution is necessary to be defined to evaluate ENS. Den besten[9] and Qin et al,[44] provided the numerical expression of weld notch stress distribution $\sigma_n(r/t_p)$ in through-thickness direction. Weld height h_w and weld leg length l_w are required to define notch angle α and stress angle β, which are shown in following equations:

$$\alpha = \frac{1}{2}(\pi + arctan(\frac{h_w}{l_w})) \tag{5.1}$$

$$\beta = \alpha - \frac{\pi}{2} \tag{5.2}$$

Weld notch stress distribution In this research, h_w is always equal to l_W thus β is 22.5° and α is $\frac{5}{8}\pi$. The expression of $\sigma_n(r/t_p)$ depends on whether the joint is symmetry, which depends on whether the stress distribution is symmetrical with respect to $\frac{t_p}{2}$ or not. For non-symmetry(typically single side and double side T-joint) case, the calculation process is shown as following equation:

$$\begin{aligned}\sigma_n(r/t_p) =&\Delta\sigma_s * [(\frac{r}{t_p})^{\lambda_S-1}\mu_S\lambda_S(\lambda_S+1)(\cos((\lambda_S+1)\beta))-\\ &\chi_S\cos((\lambda_S-1)\beta)+\\ &(\frac{r}{t_p})^{\lambda_a-1}\mu_a\lambda_a(\lambda_a+1)(\sin((\lambda_a+1)\beta))-\\ &\chi_a\sin((\lambda_a-1)\beta)+\\ &C_{bw}(2(\frac{r}{t_p})-1)-2*r_s*(\frac{r}{t_p}))]\end{aligned} \tag{5.3}$$

and in case of symmetry(typically double side butt joint):

$$\begin{aligned}\sigma_n(r/t_p) =&\Delta\sigma_s * [(1-2r_s(1-f(\frac{r}{t_p}=0.5)))f(\frac{r}{t_p})+\\ &r_s(2f(\frac{r}{t_p}=0.5)-1)*(f(\frac{r}{t_p})+(1-f(\frac{r}{t_p}=0.5))-2(\frac{r}{t_p}))]\end{aligned} \tag{5.4}$$

with

$$\begin{aligned}f(\frac{r}{t_p}) =&\Delta\sigma_s * [(\frac{r}{t_p})^{\lambda_S-1}\mu_S\lambda_S(\lambda_S+1)(\cos((\lambda_S+1)\beta))-\\ &\chi_S\cos((\lambda_S-1)\beta)+\\ &(\frac{r}{t_p})^{\lambda_a-1}\mu_a\lambda_a(\lambda_a+1)(\sin((\lambda_a+1)\beta))-\\ &\chi_a\sin((\lambda_a-1)\beta)+\\ &C_{bw}(4(\frac{r}{t_p})-1)-2*r_s*(\frac{r}{t_p})]\end{aligned} \tag{5.5}$$

and

$$f(\frac{r}{t_p}=0.5)=\frac{(\lambda_a-\lambda_S)(\lambda_a\lambda_S-2C_{bw})}{\lambda_a(\lambda_a-1)-\lambda_S)(\lambda_S-1)}+C_{bw} \tag{5.6}$$

Where μ_a and μ_S stress amplitude of (anti-)symmetry part, obtained by using force and moment equilibrium:

$$\mu_S=\frac{C_{bw}(\lambda_a+1)+3(\lambda_a-1)}{(\lambda_a-\lambda_s)(cos((\lambda_s+1)\beta)-\chi_a cos((\lambda_s-1)\beta)} \tag{5.7}$$

$$\mu_a=\frac{C_{bw}(\lambda_s+1)+3(\lambda_s-1)}{(\lambda_a-\lambda_s)(cos((\lambda_a+1)\beta)-\chi_a cos((\lambda_a-1)\beta)} \tag{5.8}$$

λ_s and λ_a are the first eigenvalues of (anti-)symmetry part, can be found from the solution of non-trivial system, in case of $\lambda>0$, $\lambda\neq 1$:

$$\begin{aligned}\lambda * sin(2\alpha)+sin(\lambda 2\alpha)=0\\ \lambda * sin(2\alpha)-sin(\lambda 2\alpha)=0\end{aligned} \tag{5.9}$$

The χ_s and χ_a are first eigenvalue coefficient of (anti-)symmetry part, can be obtained with following equations:

$$\chi_s=\frac{cos((\lambda_s+1)\alpha)}{cos((\lambda_s-1)\alpha)} \tag{5.10}$$

$$\chi_a=\frac{sin((\lambda_a+1)\alpha)}{sin((\lambda_a-1)\alpha)} \tag{5.11}$$

Weld load carrying coefficient contains the notch stress distribution specific information. Assume that σ_s*C_{bw} is the linear summation of normal force and bending induced membrane and bending stress components:

$$\begin{aligned} \sigma_s * C_{bw} &= \sigma_m * C_{bm} + \sigma_b * C_{bb} \\ C_{bm} &= \frac{m_{bm}}{\sigma_s * (1 - r_s)} * (\frac{6}{{t_P}^2}) \\ C_{bb} &= \frac{m_{bm}}{\sigma_s * r_s} * (\frac{6}{{t_P}^2}) \end{aligned} \tag{5.12}$$

Bending moment m_{bm} and m_{bb} are obtained by using FE beam model, which shows weld load carrying information. To simplify the calculations, a parametric fitting function has been obtained as well, involving a physical and fitting part. For single side case:

$$C_{bm} = -0.187 * e^{-0.527*(\frac{h_w}{l_w})} + 0.209 \tag{5.13}$$

$$C_{bb} = -0.271 * e^{-0.889*(\frac{h_w}{l_w})} + 0.302 \tag{5.14}$$

and for double side case:

$$C_{bm} = -0.056 * e^{-0.76*(\frac{h_w}{l_w})} + 0.079 \tag{5.15}$$

$$C_{bb} = -0.045 * e^{-0.37*(\frac{h_w}{l_w})} + 0.076 \tag{5.16}$$

The C_{bw} of FSM and SPM notches was obtained with equations 5.12, 5.13, 5.14, 5.15, 5.16. It should be noticed that for type B weld in SPM, due to no weld end was modeled, $\frac{hw}{lw}$ is positive infinity. Thus C_{bm} is 0.209 and C_{bb} is 0.302. Relationship between C_{bm}, C_{bb} and $\frac{hw}{lw}$ was illustrated in figure 5.1 below. When hw becomes greater, the C_{bm} and C_{bb} tend to be constant. C_{bw} value with respect to different notches are given in table 5.1 and 5.2.

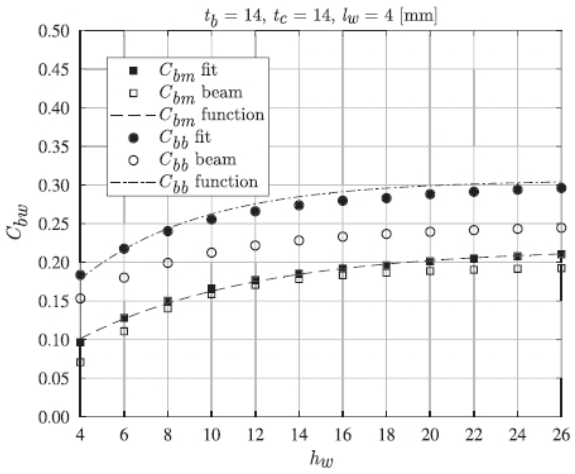

Figure 5.1: Double-sided T joint C_{bm} and C_{bb} fit for varying h_w.[43]

Effective notch stress ENS could be estimated by integrating notch stress distribution along crack path over characteristic length $\rho*$. V-shape notch is assumed at weld toe, analytical solution of ENS are given in following equations. For non-symmetry case:

$$
\begin{aligned}
\sigma_e &= \frac{1}{\rho^*}\int_0^{\rho^*}\sigma_n(r)\mathrm{d}r \\
&= \sigma_s\cdot\left(\frac{t_p}{\rho^*}\right)\cdot\left\{\left(\frac{\rho^*}{t_p}\right)^{\lambda_s}\mu_s(\lambda_s+1)[\cos\{(\lambda_s+1)\beta\}- \right. \\
&\quad \chi_s\cos\{(\lambda_s-1)\beta\}]+ \\
&\quad \left(\frac{\rho^*}{t_p}\right)^{\lambda_a}\mu_a(\lambda_a+1)[\sin\{(\lambda_a+1)\beta\}- \\
&\quad \chi_a\sin\{(\lambda_a-1)\beta\}]+ \\
&\quad \left. C_{bw}\cdot\left\{\left(\frac{\rho^*}{t_p}\right)^2-\left(\frac{\rho^*}{t_p}\right)\right\}-r_s\cdot\left(\frac{\rho^*}{t_p}\right)^2\right\}
\end{aligned}
$$

and in case of symmetry:

$$
\begin{aligned}
\sigma_e &= \frac{1}{\rho^*}\int_0^{\rho^*}\sigma_n(r)\mathrm{d}r \\
&= \sigma_s\cdot\left(\frac{t_p}{\rho^*}\right)\cdot\left\{\left[1-2r_s\left\{1-f\left(\frac{r}{t_p}=\frac{1}{2}\right)\right\}\right]\cdot\right. \\
&\quad \left(\left(\frac{\rho^*}{t_p}\right)^{\lambda_s}\mu_s(\lambda_s+1)[\cos\{(\lambda_s+1)\beta\}- \right. \\
&\quad \chi_s\cos\{(\lambda_s-1)\beta\}]+ \\
&\quad \left(\frac{\rho^*}{t_p}\right)^{\lambda_a}\mu_a(\lambda_a+1)[\sin\{(\lambda_a+1)\beta\}- \\
&\quad \chi_a\sin\{(\lambda_a-1)\beta\}]+ \\
&\quad \left. C_{bw}\cdot\left\{2\left(\frac{\rho^*}{t_p}\right)^2-\left(\frac{\rho^*}{t_p}\right)\right\}\right)+ \\
&\quad r_s\cdot\left\{2\cdot f\left(\frac{r}{t_p}=\frac{1}{2}\right)-1\right\}\cdot\left[\left\{1-f\left(\frac{r}{t_p}=\frac{1}{2}\right)\right\}\cdot\left(\frac{\rho^*}{t_p}\right)-\left(\frac{\rho^*}{t_p}\right)^2\right]\Bigg\}.
\end{aligned}
$$

In the critical distance theory, micro- and meso-structural length depend on loading and response level because of changing crack initiation and growth contributions[57]. For welded joints in steel structures, an average value of $\rho*$ is typically 0.4mm[44]. However for LSS, considering the size effect, the range of t_p dependent value $\rho*$ has been estimated for different fatigue resistance curve model(BB, ORFL, BRFL, GRFL) cases[5][44]. To keep SSS and LSS resistance data are following same model, $\rho*$=1.14mm in the GRFL model is used.

To obtain the most probable micro an meso-structural length estimate, ρ^* is taken into account. Explotional mean stress models have been developed to improve lifetime estimate in case of relatively low stress range and high mean stress, which is applicable for as-welded joints in MCF-HCF[44]. Walker's mean stress model[61] includes two required components to characterize loading&response cycle, the advance expression of effective notch stress range can be written as:

$$
S_{e,eff} = \frac{S_e}{(1-r_{lr})^{1-\gamma}} \tag{5.17}
$$

Where response stress range S_e = $\sigma_{max}-\sigma_{min}$; response stress ratio r_{lr} = $\frac{\sigma_{min}}{\sigma_{max}}$; the loading&response ratio coefficient γ is a fitting parameter, taken 0.92 in GRFL model[44]. Table below shows the $S_{e,eff}$ of all investigating HS(notch) at weld toe. Note that every case in this research is symmetrical.

HS in LSS	HS type	α	C_{bw}	S_e(MPa)	$S_{e,eff}$ (MPa)
FSM	B	$\frac{5}{8}\pi$	0.140	288	289.87
SPM S1A R25	A	$\frac{5}{8}\pi$	0.156	82	82
SPM S1A R30	A	$\frac{5}{8}\pi$	0.142	133	133
SPM S1A R35	A	$\frac{5}{8}\pi$	0.144	145	145
SPM S1A R40	A	$\frac{5}{8}\pi$	0.158	110	110
SPM S1B R25	A	$\frac{3}{4}\pi$	0.259	131	131
SPM S1B R30	A	$\frac{3}{4}\pi$	0.243	194	195
SPM S1B R35	A	$\frac{3}{4}\pi$	0.247	218	218
SPM S1B R40	A	$\frac{3}{4}\pi$	0.265	172	172
SPM S2A R30	B	$\frac{5}{8}\pi$	0.048	138	138
SPM S2B R25	A	$\frac{3}{4}\pi$	0.256	156	156
SPM S2B R30	A	$\frac{3}{4}\pi$	0.240	212	212
SPM S2B R35	A	$\frac{3}{4}\pi$	0.241	219	219
SPM S2B R40	A	$\frac{3}{4}\pi$	0.261	183	183

Table 5.1: LSS effective notch stress in as-welded shell model

HS in LSS	HS type	α	C_{bw}	S_e(MPa)	$S_{e,eff}$(MPa)
FSM	B	$\frac{5}{8}\pi$	0.146	293	295
SPM S1A R25	A	$\frac{5}{8}\pi$	0.162	104	105
SPM S1A R30	A	$\frac{5}{8}\pi$	0.149	144	145
SPM S1A R35	A	$\frac{5}{8}\pi$	0.153	158	158
SPM S1A R40	A	$\frac{5}{8}\pi$	0.166	119	120
SPM S1B R25	A	$\frac{3}{4}\pi$	0.271	130	130
SPM S1B R30	A	$\frac{3}{4}\pi$	0.259	195	195
SPM S1B R35	A	$\frac{3}{4}\pi$	0.262	216	216
SPM S1B R40	A	$\frac{3}{4}\pi$	0.273	176	176
SPM S2A R30	B	$\frac{5}{8}\pi$	0.049	123	124
SPM S2B R25	A	$\frac{3}{4}\pi$	0.270	158	158
SPM S2B R30	A	$\frac{3}{4}\pi$	0.256	199	196
SPM S2B R35	A	$\frac{3}{4}\pi$	0.256	207	208
SPM S2B R40	A	$\frac{3}{4}\pi$	0.271	175	176

Table 5.2: LSS effective notch stress in solid model

5.2. Validation in SSS scatter band

To validate the fatigue similarity between SSS and LSS, number of load cycles N(lifetime) should be evaluated. This involves the definition of fatigue failure. Generally for SSS, the experiment is stopped when the specimen is completely fractured. In this case, number of cycles N will be substituted into the S-N diagram as lifetime. However, complete fracture is not realistic in LSS experiments. Regarding to LSS, fatigue failure is usually defined in terms of crack length. Due to the reference articles of FSM and SPM did not include the specific crack shape, the penny-shape(ellipse) crack was assumed, as Figure 5.2

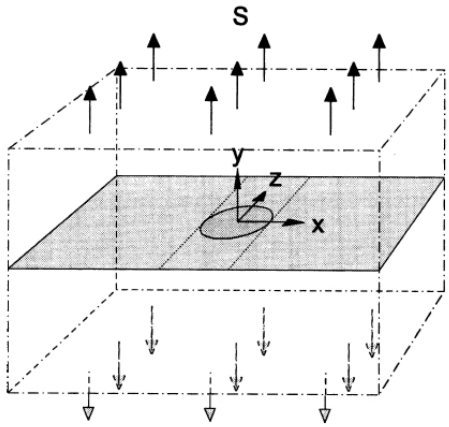

Figure 5.2: Penny-shaped crack in solid under tension.[49].

For crack in HS type B, elliptical crack grows along its major axis, which is the same direction as virtual thorugh-thickness direction(tp'). Therefore, LSS in case of HS type B can be considered as failure when crack in major axis length is equal to tp' length. When it comes to HS type A, short axis direction is the same as through-thickness direction. When the crack in minor axis grows to an equal thickness of the plate, the LSS can be considered a failure. In references of FSM and SPM, ellipse crack length are measured in major axis. Corresponding lifetime N are recorded as well. The choice of crack length and N in different cases are listed as table 5.3. Note that in Miki's article only the vague lifetime is shown in the SN-diagram, therefore, lifetime in SPM is only approximation and is not entirely accurate.

Specimen&HS	HS type	crack length(mm)	Lifetime(N)
FSM	B	20	638,000
SPM S2A R30	B	10	1,000,000
SPM S1A R25	A	20	950,000
SPM S1A R30	A	20	850,000
SPM S1A R35	A	20	850,000
SPM S1A R40	A	20	850,000
SPM S1B R25	A	20	2,200,000
SPM S1B R30	A	20	2,000,000
SPM S1B R35	A	20	1,700,000
SPM S1B R40	A	20	2,000,000
SPM S2B R40	A	20	1,300,000
SPM S2B R45l	A	20	750,000
SPM S2B R45r	A	20	750,000
SPM S2B R50	A	20	900,000

Table 5.3: Lifetime approximation from reference articles.[31][6]

In Figures below, LSS fatigue resistance data are overlayed into SSS scatter band(created by Qin[44]). The SSS data scatter band is set to black, fatigue resistance data of FSM, SPM S1A, SPM S1B, SPM S2A, SPM S2B are set to red, green, cyan, magenta, yellow colors respectively. From figure 5.13 and 5.14 it is shown that the resistance data of SPM S1A and S2A are not included into the SSS scatter band, which located below that. The LSS have lower lifetime than SSS in same effective notch stress range. This means that LSS is less fatigue resistant than SSS. In marine industries, the SSS standard should not be used for fatigue design for LSS.

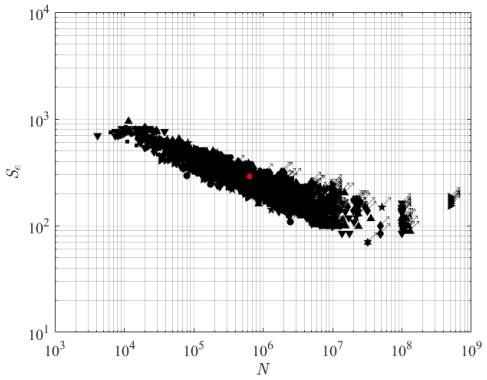

Figure 5.3: Fatigue similarity between SSS and FSM shell result

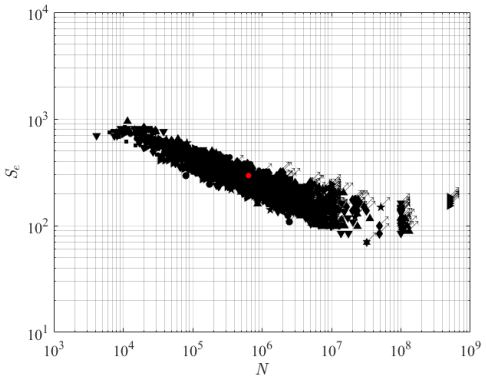

Figure 5.4: Fatigue similarity between SSS and FSM solid result

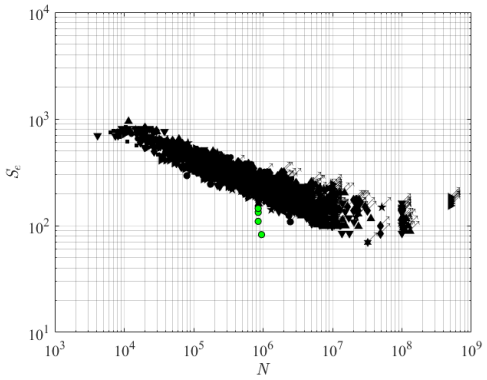

Figure 5.5: Fatigue similarity between SSS and SPM S1A shell result

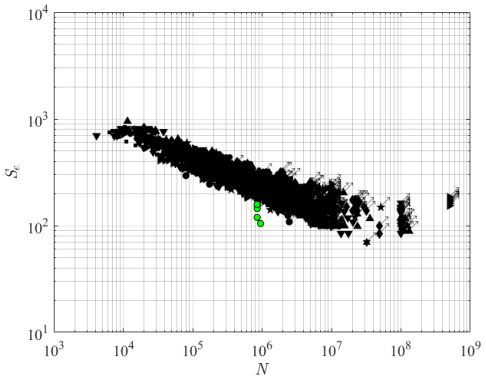

Figure 5.6: Fatigue similarity between SSS and SPM S1A solid result

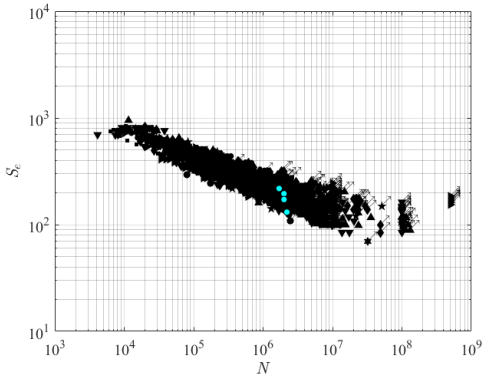

Figure 5.7: Fatigue similarity between SSS and SPM S1B shell result

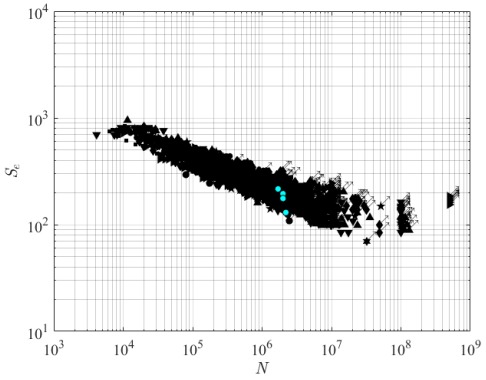

Figure 5.8: Fatigue similarity between SSS and SPM S1B solid result

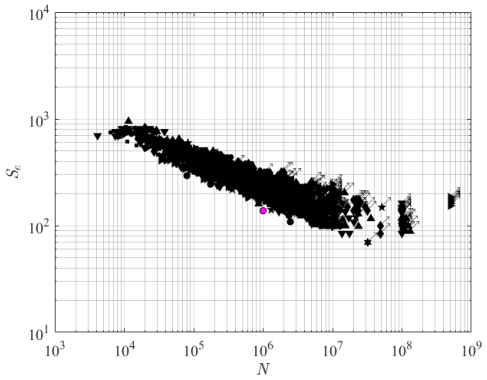

Figure 5.9: Fatigue similarity between SSS and SPM S2A shell result

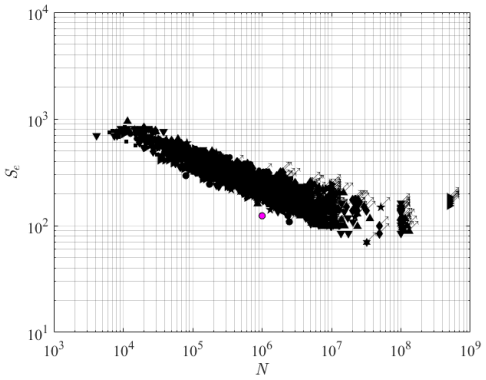

Figure 5.10: Fatigue similarity between SSS and SPM S2A solid result

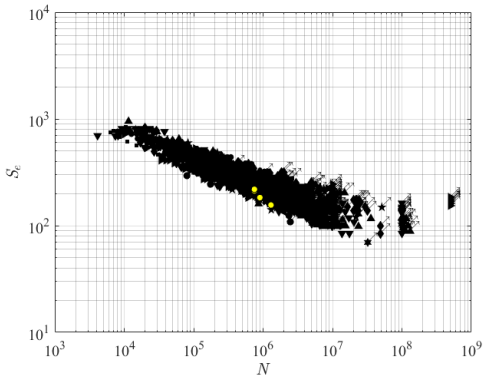

Figure 5.11: Fatigue similarity between SSS and SPM S2B shell result

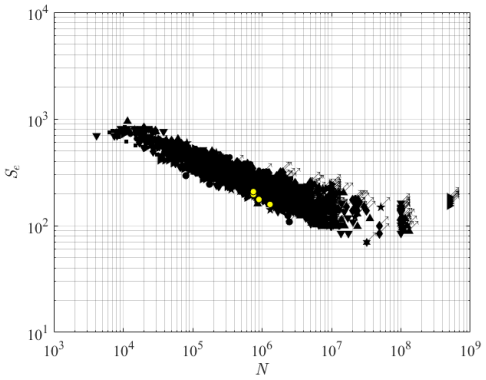

Figure 5.12: Fatigue similarity between SSS and SPM S2B solid result

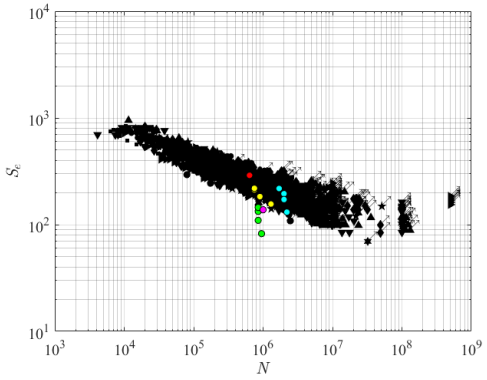

Figure 5.13: Fatigue similarity between SSS and LSS shell result

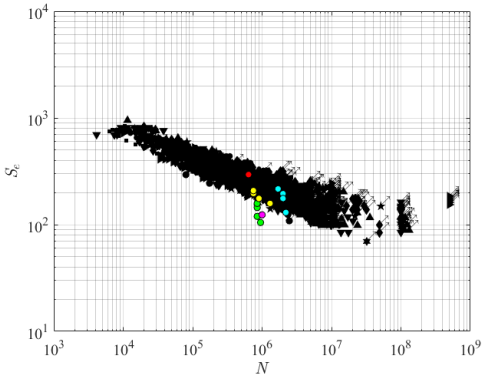

Figure 5.14: Fatigue similarity between SSS and LSS solid result

6

Conclusion

In this chapter, the research conclusion is stated. Apart from that, the recommendation is also listed.

6.1. Conclusion

To achieve the research objectives and address the questions, two kinds of typical LSS were selected from the existing literature, which are Frame-stiffener model and stiffener-plate model. According to different LSS models shell element models with and without weld seams were first established in ANSYS APDL. Traction forces based procedure is used to evaluate HS structural stress. Meanwhile, solid element models are also modelled to verify the structural stress. After obtaining the above results, effective notch stress calculations were performed based on structural stress for two different weld end models. In consequence, ENS and lifetime data of LSS were substituted into SSS fatigue scatter band, the fatigue similarity was validated.

The purpose of this research is to validate fatigue similarity between maritime structural steel small-sclae specimens and large-sclae specimen. This is verified by substituting LSS fatigue data into SSS fatigue scatter band. meanwhile, the influence of weld modeling in shell element model for LSS is also investigated. In this thesis, inclined shell method was applied to verify the HS structural stress difference between as-welded and unwelded model. The research questions and answers are listed below:
Research question 1:

1 Is weld modeling required to obtain accurate arc-welded joint far field stress estimates?

- Weld modeling is crucial to be built in FEM shell model. Structural stress in unwelded model is always higher than that in as-welded model. Hence fatigue resistance data in S-N plot will be overestimated. This results in fatigue failure occurs earlier than expected.

Research question 1 subquestions:

1.1 Planar LSS and HS identification.

- The research objective LSS in this study include two models, which are FSM and SPM. In the actual study, stress calculations were conducted for the various HS near the lug plate and cope hole.

1.2 How to build the weld seam in shell element models?

- According to IIW recommendations, the inclined shell method was employed for weld seam modeling. In the SPM, two different weld seam shapes were modeled separately. Type A weld seam contains a boxing weld, while Type B weld seam does not.

1.3 How about the difference in structural stress result between extrapolation method and traction forces based method?

- For FSM, HS structural stress results by surface extrapolation method is greater than that of traction forces based procedure. This is reasonable, as the mesh sensitivity of the former can lead to deviations due to singularity when the mesh size is not small enough. This usually results in an increase in the results.

1.4 How does the weld modeling influence structural stress results in FSM?

- When using traction forces based procedure to calculate the structural stress of HS Type B in FSM, the results from the shell model without weld seams are relatively greater compared to those from the shell element model with weld seams. The magnitude of this difference is approximately ten percent. This could be due to the joint angle becoming less perpendicular and more gradual from unwelded case to as-welded case.

1.5 Does the FSM shell element model indicate reasonable results?

- By comparing the structural stresses obtained from the solid model and the as-welded shell model, it was found that there was almost no difference between the two. This validates the accuracy of the FEM shell model and proves the importance of weld seam modeling in the shell model.

1.6 How to evaluate structural stress when there is no weld end modeled?

- In the SPM, when investigating the weld type B model and the unwelded model, structural stress calculations were performed using the virtual node method due to the sharp geometric discontinuities near HS type A.

1.7 For SPM, does weld modeling indicate similar effects as FSM?

- Similar to the results presented in the FSM, in the SPM, the structural stress range of the shell model without weld seams is greater than that of the model with weld seams; Additionally, the results for the type B weld model are higher than those for the type A weld model but lower than those for the unwelded model. Depending on the type and location of the HS, the difference in stress range varies between 18% and 30%.

1.8 Does the SPM shell element model indicate reasonable results?

- The results from the SPM solid model are generally comparable to those from the shell model with weld seams. But for S1A R25 and S2A R30 case, the deviation becomes to 21.2% and -12.1% respectively. here could be two reasons for this phenomenon. First is because triangular cone-shaped elements exist at type A weld, which induced inaccurate output nodal force; the second is coinciding section induces higher material stiffness near the weld root when modeling weld seam.

Research question 2:

2 Will fatigue resistance data of large-scale specimens have similarity with regard to small-scale specimens fatigue scatter band?

- By overlaying the ENS and lifetime of LSS into the SSS scatter band, it was found that LSS fatigue resistance data is included in most cases. Fatigue resistance data of S1A(R30 and R35) and S2A are located at the low boundary of SSS scatter band. However, S1A(R25 and R40) fatigue resistance data falls below the scatter band. This means that in this case the LSS fatigue resistance is worse than every tested SSS. The fatigue criteria for SSS do not apply to LSS.

Research question 2 subquestions:

2.1 For as-welded shell and solid element models, what is the effective notch stress based on structural stress?

- In chapter 5 the effective notch stress of hot spots are investigated and calculated. Since the type B welded model in the SPM does not have a boxing weld at the weld end, C_{bw} is higher than that in type A welded model. By comparing the ENS, it was found that the results for the type B weld cases are higher. This is because the notch angle has increased, leading to more stress concentration.

2.2 How to define lifetime N according to current literature and assumptions?

- The fatigue failure criterion for LSS is assumed to be when the crack length grows in through-thickness direction to equal the thickness of plate tp(Note that in HS type B case, tp'=tp). The lifetime corresponding to different crack locations was determined from the reference literatures.

6.2. Recommandations for further research

Based on the results of this study and the above conclusions, the following recommendations for further research are outlined in this section.

- In FEM modeling, inclined shell method in shell element model induces overlapping sections between weld seam and plates. This results in higher material stiffness at weld root position. This probably affects the results of structural stress at the weld toe. In future relative research, the rigid connection method should be employed, using rigid bars to connect the nodes on the inclined shell and the plate to model the weld seam. This method ensures that the stiffness near the weld root is accurately represented.
- Due to the performance limitations of the PC, it is not possible to use a globally finer mesh in the solid model. There are some irregular triangular cones generated near investigating area. This may lead to relatively inaccurate results. When researching LSS, a more powerful computer should be used to achieve a globally fine mesh(i.e. DelftBlue).
- Considering that in fatigue similarity validation, the lifetime is approximated from SN curves in the literature, and the fatigue failure criteria based on crack length are assumed and probably have a gap compared to actual conditions, the fatigue resistance results for LSS may not be entirely accurate in scatter band. Meanwhile, both references were published two decades ago, manufacture technology particularly welding is not state-of-art. Which results in the lifetime to failure is not accurate, most likely much lower than ideal. In future research, it is recommended to use new experimental data to determine the relationship between crack length and lifetime, and to develop more comprehensive failure criteria.
- Weld load carrying stress coefficient C_{bw} should be evaluated with more rigorous approach in case of unwelded notch. For instance, fitting curves between $sigma_n$ and FEA result(should obtain more than 10 elements in through-thickness direction). In the current research, C_{bw} was determined by Qin[44]'s empirical formula.
- Regarding to effective notch stress evaluating, this study only includes DS T-joints and SS T-joints, which are both stress distribution non-symmetrical case. To obtain more general results, it is also important to investigate symmetrical cases in future(i.e. butt joint).
- Similar to the previous recommendation, this study only investigates planar LSS and does not include tubular LSS, which significantly differs in stress distribution and stress calculation. Further research should address this gap by including tubular LSS studies.

References

[1] ANSYS. *ANSYS APDL Element Reference*. 2022.

[2] Mustafa Aygül. *Fatigue analysis of welded structures using the finite element method*. Chalmers Tekniska Hogskola (Sweden), 2012.

[3] Zuheir Barsoum. “Residual stress analysis and fatigue of multi-pass welded tubular structures”. In: *Engineering failure analysis* 15.7 (2008), pp. 863–874.

[4] Bathias. “There is no infinite fatigue life in metallic materials”. In: *Fatigue & fracture of engineering materials & structures* 22.7 (1999), pp. 559–565.

[5] J Baumgartner and R Waterkotte. “Crack initiation and propagation analysis at welds–assessing the total fatigue life of complex structures: Rissinitiierung und Wahrscheinlichkeitsanalyse an Schweißverbindungen–Abschätzung der Lebensdauer von komplexen Strukturen”. In: *Material-wissenschaft und Werkstofftechnik* 46.2 (2015), pp. 123–135.

[6] S Berge, A Johansen, and Lars G Bjorheim. “Fatigue strength assessment of hull details for an FPSO”. In: *Proceedings of the Practical Design of Ships and Other Floating Structures, PRADS’01, Papers: P2001-10 Proceedings.* (2001).

[7] Gabriele Bufalari, Henk den Besten, and Miroslaw Lech Kaminski. “Mode-III fatigue of welded joints in steel maritime structures: Weld notch shear stress distributions and effective notch stress based resistance”. In: *International Journal of Fatigue* 165 (2022), p. 107210.

[8] Luis Simões Da Silva, Rui Simões, and Helena Gervásio. *Design of steel structures: eurocode 3: design of steel structures, part 1-1: general rules and rules for buildings*. John Wiley & Sons, 2012.

[9] JH Den Besten. “Fatigue resistance of welded joints in aluminium high-speed craft: a total stress concept”. In: (2015).

[10] Hans-Jörg G Diersch and Hans-Jörg G Diersch. “Fundamental Concepts of Finite Element Method (FEM)”. In: *FEFLOW: Finite Element Modeling of Flow, Mass and Heat Transport in Porous and Fractured Media* (2014), pp. 239–404.

[11] P Dong. “A structural stress definition and numerical implementation for fatigue analysis of welded joints”. In: *International journal of fatigue* 23.10 (2001), pp. 865–876.

[12] P Dong et al. “Assessment of ASME’s FSRF rules for vessel and piping welds using a new structural stress method”. In: *Welding in the World* 47 (2003), pp. 31–43.

[13] Pingsha Dong. “A robust structural stress method for fatigue analysis of offshore/marine structures”. In: *J. Offshore Mech. Arct. Eng.* 127.1 (2005), pp. 68–74.

[14] CEN EN. “1-1, Eurocode 3: Design of steel structures”. In: *General rules and rules for buildings* (1993).

[15] Åsa Eriksson et al. *Weld evaluation using FEM: a guide to fatigue-loaded structures*. Industrilitteratur, 2003.

[16] Anders Viggo Hansen and Henning Agerskov. “Fatigue Assessment of Root Defects in the Welded Structure of a Large Two-Stroke Diesel Engine”. In: *8th International Fatigue Congress: Design and Analysis of Welded High Strength Steel Structures*. EMAS Publishing. 2002, pp. 373–390.

[17] Brian E Healy. “A case study comparison of surface extrapolation and Battelle structural stress methodologies”. In: *International Conference on Offshore Mechanics and Arctic Engineering*. Vol. 37432. 2004, pp. 447–464.

[18] Brian E Healy. “A comparison of the surface extrapolation and battelle structural stress methodologies as applied to a spectral fatigue analysis of a representative FPSO structural detail”. In: *International Conference on Offshore Mechanics and Arctic Engineering*. Vol. 42703. 2007, pp. 269–279.

[19] TUDelft Henk den Besten. *OE44085 slide*. 2022.

[20] Mohsen Heshmati. “Fatigue life assessment of bridge details using finite element method”. In: (2012).

[21] AF Hobbacher et al. *Recommendations for fatigue design of welded joints and components*. Vol. 47. Springer, 2016.

[22] David Hutton. “Fundamentals of finite element analysis”. In: *(No Title)* (2004).

[23] Khangamlung Kamei and Muhammad A Khan. “Current challenges in modelling vibrational fatigue and fracture of structures: A review”. In: *Journal of the Brazilian Society of Mechanical Sciences and Engineering* 43.2 (2021), p. 77.

[24] Burak Karabulut et al. “Experimental and numerical fatigue assessment of duplex welded transversal stiffeners”. In: *International Journal of Fatigue* 134 (2020), p. 105498.

[25] SK Khanna and X Long. “Fatigue behavior of spot welded joints in steel sheets”. In: *Failure mechanisms of advanced welding processes*. Elsevier, 2010, pp. 65–100.

[26] Myung Hyunn Kim et al. “Fatigue Assessment of Ship Structures using Hot Spot Stress and Structural Stress Approaches with Experimental Validation”. In: *SNAME Maritime Convention*. SNAME. 2008, D011S002R004.

[27] Jae-Myung Lee et al. “Comparison of hot spot stress evaluation methods for welded structures”. In: *International Journal of Naval Architecture and Ocean Engineering* 2.4 (2010), pp. 200–210.

[28] Ding Liao et al. “Probabilistic framework for fatigue life assessment of notched components under size effects”. In: *International Journal of Mechanical Sciences* 181 (2020), p. 105685.

[29] Zwiep M B. “The useability of small-scale specimen fatigue tests in the design of full-scale marine structures”. In: (2023).

[30] Total Materia. *Fracture Mechanics: Part Three*. 2024.

[31] Chitoshi Miki and Kazuo Tateishi. “Fatigue strength of cope hole details in steel bridges”. In: *International journal of fatigue* 19.6 (1997), pp. 445–455.

[32] Yukitaka Murakami et al. “Essential structure of SN curve: Prediction of fatigue life and fatigue limit of defective materials and nature of scatter”. In: *International Journal of Fatigue* 146 (2021), p. 106138.

[33] Eeva Nyk Nen and Eeva Nykänen. *Fragmented state power and forced migration: a study on non-state actors in refugee law*. Martinus Nijhoff Publishers, 2012.

[34] Offshore Network. *Petrobras marks strategy refocus by awarding letter of intent for FPSO lease to SBM Offshore*. 2021. URL: https://offsnet.com/content/latin-america/petrobras-marks-strategy-refocus-by-awarding-letter-of-intent-for-fpso-lease-to-sbm-offshore-and-sale-of-onshore-assets.

[35] E Niemi and P Tanskanen. “Hot Spot Stress Determination for Welded Edge Gussets, The International Institute of Welding-IIW Doc”. In: (1999).

[36] Erkki Niemi. *Stress determination for fatigue analysis of welded components*. Woodhead Publishing, 1995.

[37] Erkki Niemi et al. *The structural hot-spot stress approach to fatigue analysis*. Springer, 2018.

[38] E Oanta, V Hreniuc, and P Brice. “Analytical Model of a Bulb Flat”. In: *IOP Conference Series: Materials Science and Engineering*. Vol. 444. 6. IOP Publishing. 2018, p. 062006.

[39] Sayantan Pandit. “Finite element modelling of open longitudinal stiffener to crossbeam connection in OSD bridges for hot-spot stress determination”. In: (2020).

[40] Ioannis V Papadopoulos and Vassilis P Panoskaltsis. “Invariant formulation of a gradient dependent multiaxial high-cycle fatigue criterion”. In: *Engineering Fracture Mechanics* 55.4 (1996), pp. 513–528.

[41] Mikkel Melters Pedersen. “Introduction to metal fatigue”. In: *Aarhus University* (2018).

[42] Constanze Przybilla et al. “A model allowing for the influence of geometry and stress in the assessment of fatigue data”. In: (2013).

[43] Yanxin Qin et al. “Fatigue design of welded double-sided T-joints and double-sided cruciform joints in steel marine structures: A total stress concept”. In: *Fatigue & Fracture of Engineering Materials & Structures* 42.12 (2019), pp. 2674–2693.

[44] Yanxin Qin et al. “Mid-and high-cycle fatigue of welded joints in steel marine structures: effective notch stress and total stress concept evaluations”. In: *International Journal of Fatigue* 142 (2021), p. 105822.

[45] Dieter Radaj, Cetin Morris Sonsino, and Wolfgang Fricke. *Fatigue assessment of welded joints by local approaches*. Woodhead publishing, 2006.

[46] Kasja Romijn. “Fatigue design investigation of the main-to cross-girder connection in steel railway bridges: A study on the beam railway bridges of the Oostertoegang in Amsterdam”. In: (2023).

[47] Philippe Rucho. “Fatigue Analysis of Floating Offshore Steel Structures-BATTELLE Structural Stress Methodology–”. In: *BV draft guidance note* (2007).

[48] Dikshant Singh Saini, Debasis Karmakar, and Samit Ray-Chaudhuri. “A review of stress concentration factors in tubular and non-tubular joints for design of offshore installations”. In: *Journal of Ocean Engineering and Science* 1.3 (2016), pp. 186–202.

[49] Jaap Schijve. *Introduction to fatigue of structures and materials*. Springer, 2001.

[50] P Selvakumar and JK Hong. “Robust mesh insensitive structural stress method for fatigue analysis of welded structures”. In: *Procedia Engineering* 55 (2013), pp. 374–379.

[51] M Shirani and G Härkegård. “Large scale axial fatigue testing of ductile cast iron for heavy section wind turbine components”. In: *Engineering Failure Analysis* 18.6 (2011), pp. 1496–1510.

[52] Toru Shiratsuchi and Naoki Osawa. “Investigation of thickness and bead profile effects on fatigue strength of welded joints based on relative stress gradient”. In: *International Journal of Fatigue* 134 (2020), p. 105520.

[53] Cetin Morris Sonsino. “Course of SN-curves especially in the high-cycle fatigue regime with regard to component design and safety”. In: *International Journal of Fatigue* 29.12 (2007), pp. 2246–2258.

[54] Cetin Morris Sonsino and Gerhard Fischer. “Local assessment concepts for the structural durability of complex loaded components”. In: (2005).

[55] CM Sonsino. “Effect of residual stresses on the fatigue behaviour of welded joints depending on loading conditions and weld geometry”. In: *International Journal of Fatigue* 31.1 (2009), pp. 88–101.

[56] British Steel. *Bulb Flat British Steel*. 2021.

[57] David Taylor. “The theory of critical distances”. In: *Engineering Fracture Mechanics* 75.7 (2008), pp. 1696–1705.

[58] George Totten. “Fatigue crack propagation.” In: *Advanced Materials & Processes* 166.5 (2008), pp. 39–42.

[59] D Turlier, P Klein, and F Bérard. “Seam Sim” method for seam weld structural assessment within a global structure FEA”. In: *Proc. Int. Conf. IIW2010 Istanbul (Turkey). AWST*. 2010, pp. 651–658.

[60] West Virginia University. *Solid element slide*. 2021.

[61] Kevin Walker. “The effect of stress ratio during crack propagation and fatigue for 2024-T3 and 7075-T6 aluminum”. In: *Effects of environment and complex load history on fatigue life* (1970), pp. 1–14.

[62] Zezhong Wei et al. “A simplified approach to estimate the fatigue life of full-scale welded cast steel thin-walled tubular structures”. In: *Thin-Walled Structures* 160 (2021), p. 107348.

[63] Farshid Zamiri Akhlaghi. “Fatigue life assessment of welded bridge details using structural hot spot stress method”. In: (2009).

[64] Shun-Peng Zhu et al. “Recent advances on size effect in metal fatigue under defects: a review”. In: *International Journal of Fracture* (2021), pp. 1–23.

[65] Shun-Peng Zhu et al. “Stress gradient effect in metal fatigue: Review and solutions”. In: *Theoretical and Applied Fracture Mechanics* 121 (2022), p. 103513.

A

Unweld FSM shell model

To determine authenticity, the output of the FEM simulation will be shown in the appendix so that the reader can calculate it for himself. Due to the large number of APDL codes, they are not displayed here. This appendix mainly shows the contour diagram of the FEM model, nodal force and stress in reference nodes.
Nodal force value extracted from element solution. The two output values correspond to the adjacent elements. The last node only contains one value, because the contribution of next element will not be considered. Virtual thickness t'_p is defined as 20mm.

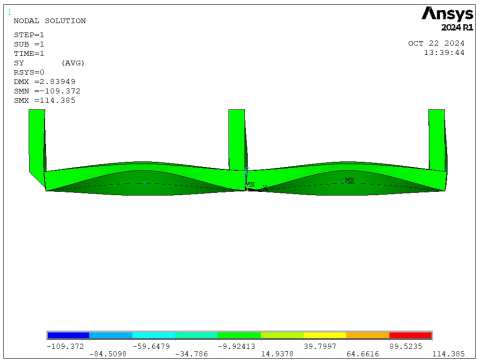

Figure A.1: Unweld FSM front view

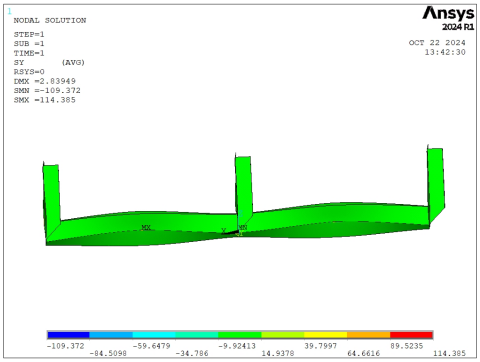

Figure A.2: Unweld FSM back view

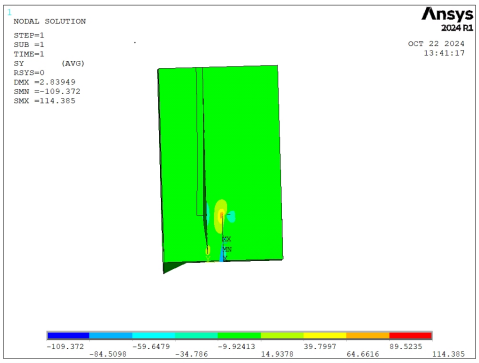

Figure A.3: Unweld FSM left view

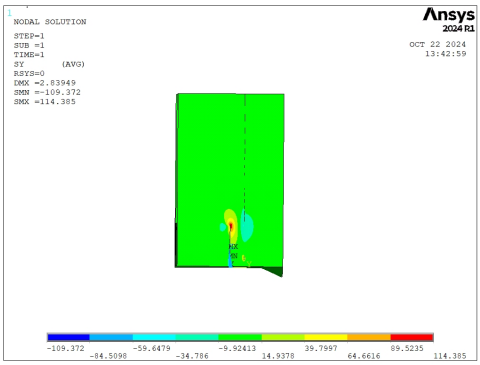

Figure A.4: Unweld FSM right view

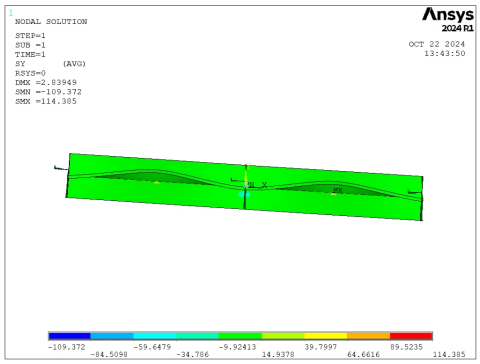

Figure A.5: Unweld FSM top view

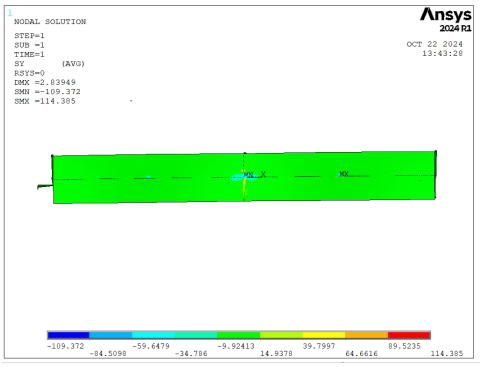

Figure A.6: Unweld FSM bottom view

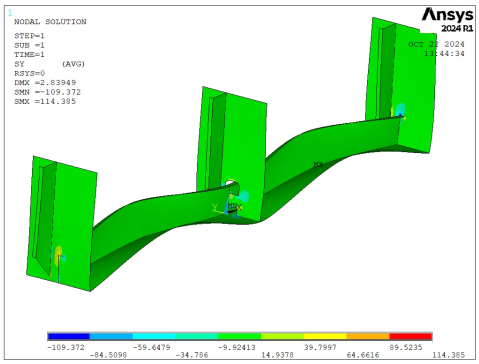

Figure A.7: Unweld FSM oblique view

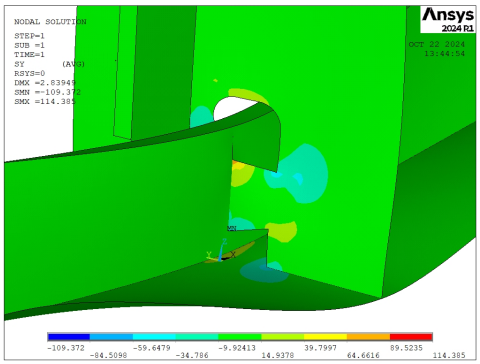

Figure A.8: Unweld FSM zoom in

A.1. Reference node data output

The normal stress value in this section extracted from nodal solution, thus the output for one node will be 2 values with respect to front and back sides. In case that no nodes locate at 4mm, 8mm, 12mm directly, linear interpolating the value with adjacent nodes.

Node number	Y coordinates(mm)	σ_y front(MPa)	σ_y back(MPa)	σ_y average(MPa)
427	4	105.19	113.17	109.18
423	8	89.41	67.263	78.3365
419	12	75.423	52.185	63.804

Table A.1: Unweld FSM extrapolation method reference nodes outcome(ES=1mm)

Node number	Y coordinates(mm)	σ_y front(MPa)	σ_y back(MPa)	σ_y average(MPa)
287	2.985507246	138.36	105.08	121.72
286	4.47826087	104.55	100.26	102.405
284	7.463768116	90.374	71.329	80.8515
283	8.956521739	85.158	62.864	74.011
281	11.94202899	75.462	52.503	63.9825

Table A.2: Unweld FSM extrapolation method reference nodes outcome(ES=1.5mm)

Node number	Y coordinates(mm)	σ_y front(MPa)	σ_y back(MPa)	σ_y average(MPa)
215	3.961538462	115.15	103.06	109.105
213	7.923076923	89.292	69.491	79.3915
211	11.88461538	76.071	53.203	64.637

Table A.3: Unweld FSM extrapolation method reference nodes outcome(ES=2mm)

Node number	Y coordinates(mm)	σ_y front(MPa)	σ_y back(MPa)	σ_y average(MPa)
174	2.452380952	150.2	101.95	126.075
173	4.9	93.434	98.229	95.8315
172	7.357142857	72.975	87.576	80.2755
171	9.80952381	80.448	59.744	70.096
170	12.26190476	51.821	73.504	62.6625

Table A.4: Unweld FSM extrapolation method reference nodes outcome(ES=2.5mm)

Node number	Y coordinates(mm)	σ_y front(MPa)	σ_y back(MPa)	σ_y average(MPa)
146	2.942857143	135.4	97.809	116.6045
145	5.885714286	86.569	89.694	88.1315
144	8.828571429	82.531	64.563	73.547
143	11.77142857	53.385	74.461	63.923

Table A.5: Unweld FSM extrapolation method reference nodes outcome(ES=3mm)

Node number	Y coordinates(mm)	σ_y front(MPa)	σ_y back(MPa)	σ_y average(MPa)
124	3.433333333	122.45	93.585	108.0175
123	6.866666667	85.696	77.452	81.574
122	10.3	77.458	58.207	67.8325
121	13.73333333	68.867	48.445	58.656

Table A.6: Unweld FSM extrapolation method reference nodes outcome (ES=3.5mm)

Node number	Y coordinates(mm)	σ_y front(MPa)	σ_y back(MPa)	σ_y average(MPa)
108	3.961538462	112.26	90.136	101.198
107	7.923076923	81.862	70.101	75.9815
106	11.88461538	72.687	53.058	62.8725

Table A.7: Unweld FSM extrapolation method reference nodes outcome (ES=4mm)

Node number	Y coordinates(mm)	σ_y front(MPa)	σ_y back(MPa)	σ_y average(MPa)
74	5.722222222	81.618	88.446	85.032
73	11.44444444	54.328	71.156	62.742
72	17.16666667	59.903	41.729	50.816

Table A.8: Unweld FSM extrapolation method reference nodes outcome (ES=6mm)

Node number	Y coordinates(mm)	σ_y front(MPa)	σ_y back(MPa)	σ_y average(MPa)
2	0	93.478	81.343	87.4105
54	7.923076923	71.458	75.006	73.232
53	15.84615385	61.401	43.011	52.206

Table A.9: Unweld FSM extrapolation method reference nodes outcome (ES=8mm)

Node number	Y coordinates(mm)	σ_y front(MPa)	σ_y back(MPa)	σ_y average(MPa)
2	0	75.343	74.224	74.7835
38	11.44444444	66.421	55.986	61.2035
37	22.88888889	49.196	32.438	40.817

Table A.10: Unweld FSM extrapolation method reference nodes outcome (ES=12mm)

Node number	Z coordinates(mm)	Nodal force 1	Nodal force 2	Nodal force summation
540	210.55	-3392.6	0	-3392.6
618	206.5660714	-2193.1	-1515	-3708.1
617	202.5821429	-720.09	-1569.4	-2289.49
616	198.5982143	-834	-1169.2	-2003.2
615	194.6142857	-432.67	-1083.2	-1515.87
614	190.6303571	-404.36	0	-404.36

Table A.11: Unweld FSM traction force based method reference nodes outcome(ES=4mm)

Node number	Z coordinates(mm)	Nodal force 1	Nodal force 2	Nodal force summation
428	210.55	-3864.4	0	-3864.4
450	205.7	-2418.4	-1740.8	-4159.2
449	200.85	-713.41	-1777.9	-2491.31
448	196	-821.88	-1305.3	-2127.18
447	191.15	-349.68	0	-349.68

Table A.12: Unweld FSM traction force based method reference nodes outcome(ES=5mm)

Node number	Z coordinates(mm)	Nodal force 1	Nodal force 2	Nodal force summation
302	210.55	-4352.1	0	-4352.1
320	204.6789474	-2703.9	-1932.7	-4636.6
319	198.8078947	-716.54	-1961.1	-2677.64
318	192.9368421	-817.23	0	-817.23

Table A.13: Unweld FSM traction force based method reference nodes outcome(ES=6mm)

Node number	Z coordinates(mm)	Nodal force 1	Nodal force 2	Nodal force summation
207	210.55	-4838.9	0	-4838.9
222	203.578125	-2933.9	-2159.1	-5093
221	196.60625	-674.98	-2141.2	-2816.18
220	189.634375	-751.99	0	-751.99

Table A.14: Unweld FSM traction force based method reference nodes outcome(ES=7mm)

Node number	Z coordinates(mm)	Nodal force 1	Nodal force 2	Nodal force summation
137	210.55	-5818.5	0	-5818.5
148	201.2541667	-3348.4	-2527.9	-5876.3
147	191.9583333	-482.84	0	-482.84

Table A.15: Unweld FSM traction force based method reference nodes outcome(ES=10mm)

Node number	Z coordinates(mm)	Nodal force 1	Nodal force 2	Nodal force summation
109	210.55	-6450.2	0	-6450.2
118	199.395	-3584	-2811.4	-6395.4
117	188.24	-301.56	0	-301.56

Table A.16: Unweld FSM traction force based method reference nodes outcome(ES=12mm)

B

Aswelded FSM shell model

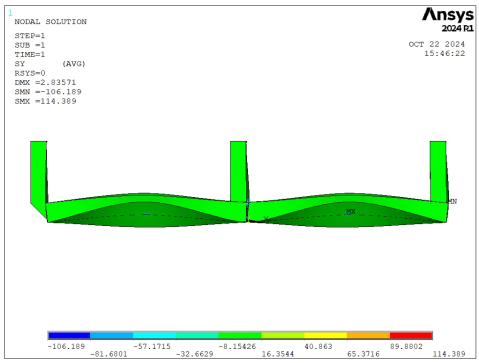

Figure B.1: Asweld FSM front view

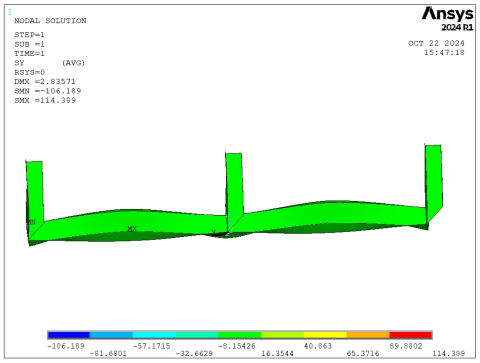

Figure B.2: Asweld FSM back view

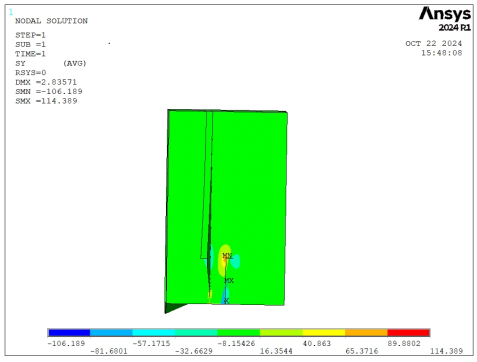

Figure B.3: Asweld FSM left view

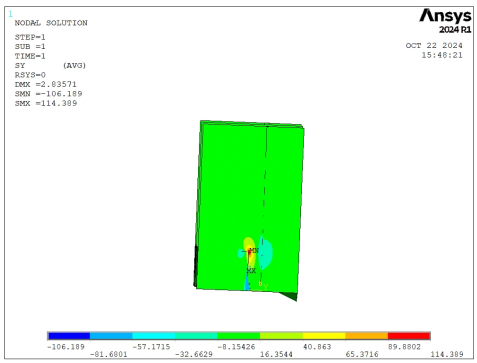

Figure B.4: Asweld FSM right view

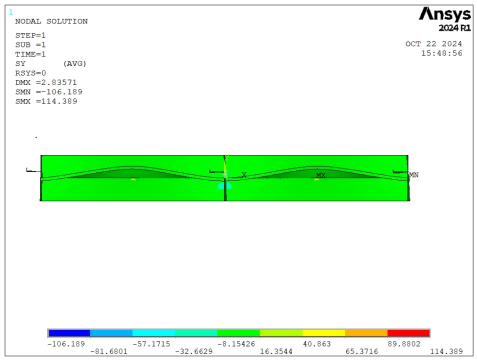

Figure B.5: Asweld FSM top view

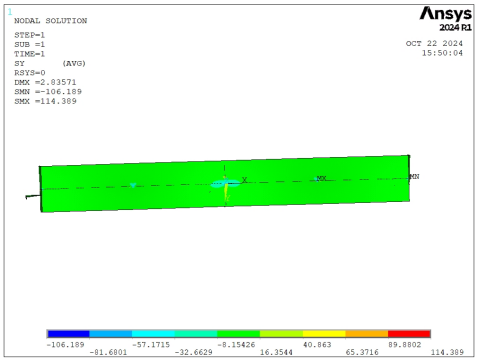

Figure B.6: Asweld FSM bottom view

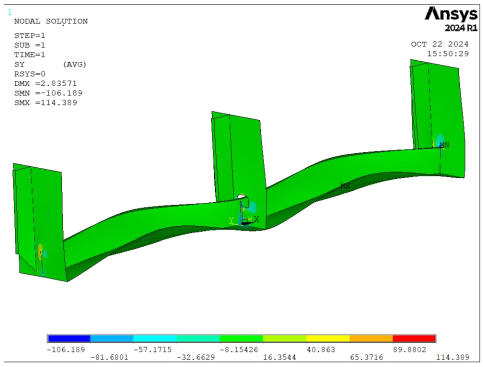

Figure B.7: Asweld FSM oblique view

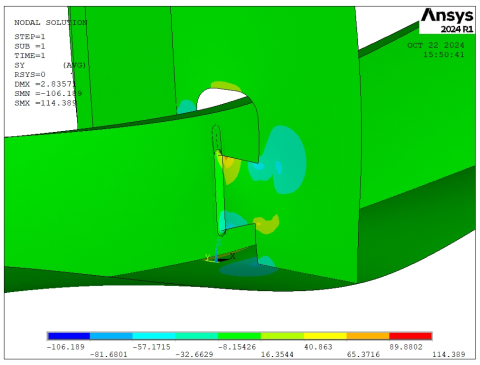

Figure B.8: Asweld FSM zoom in

B.1. Reference node data output

Node number	Y coordinates(mm)	σ_y front(MPa)	σ_y back(MPa)	σ_y average(MPa)
9689	16	88.817	87.788	88.3025
9685	20	51.897	89.547	70.722
9681	24	79.641	40.434	60.0375

Table B.1: Asweld FSM extrapolation method reference nodes outcome(ES=1mm)

Node number	Y coordinates(mm)	σ_y front(MPa)	σ_y back(MPa)	σ_y average(MPa)
4605	14.98360656	109.14	80.321	94.7305
4604	16.47540984	82.63	87.627	85.1285
4602	19.45901639	55.759	88.953	72.356
4601	20.95081967	48.956	86.366	67.661
4599	23.93442623	79.282	40.891	60.0865

Table B.2: Asweld FSM extrapolation method reference nodes outcome(ES=1.5mm)

Node number	Y coordinates(mm)	σ_y front(MPa)	σ_y back(MPa)	σ_y average(MPa)
2547	15.95652174	84.459	90.57	87.5145
2545	19.91304348	86.804	54.344	70.574
2543	23.86956522	78.702	41.409	60.0555

Table B.3: Asweld FSM extrapolation method reference nodes outcome(ES=2mm)

Node number	Y coordinates(mm)	σ_y front(MPa)	σ_y back(MPa)	σ_y average(MPa)
174	2.452380952	150.2	101.95	126.075
1780	14.45945946	115.31	79.458	97.384
1779	16.91891892	85.822	78.008	81.915
1778	19.37837838	86.224	57.91	72.067
1777	21.83783784	82.355	47.222	64.7885
1776	24.2972973	77.048	40.865	58.9565

Table B.4: Asweld FSM extrapolation method reference nodes outcome(ES=2.5mm)

Node number	Y coordinates(mm)	σ_y front(MPa)	σ_y back(MPa)	σ_y average(MPa)
1248	14.93548387	81.76	104.45	93.105
1247	17.87096774	85.708	69.037	77.3725
1246	20.80645161	83.401	51.42	67.4105
1245	23.74193548	42.372	77.684	60.028

Table B.5: Asweld FSM extrapolation method reference nodes outcome(ES=3mm)

Node number	Y coordinates(mm)	σ_y front(MPa)	σ_y back(MPa)	σ_y average(MPa)
976	15.5	94.602	84.22	89.411
975	19	61.158	84.89	73.024
974	22.5	79.797	45.895	62.846
973	26	72.422	38.137	55.2795

Table B.6: Asweld FSM extrapolation method reference nodes outcome (ES=3.5mm)

Node number	Y coordinates(mm)	σ_y front(MPa)	σ_y back(MPa)	σ_y average(MPa)
749	15.95652174	87.668	84.52	86.094
748	19.91304348	83.164	56.137	69.6505
747	23.86956522	76.431	42.43	59.4305

Table B.7: Asweld FSM extrapolation method reference nodes outcome (ES=4mm)

Node number	Y coordinates(mm)	σ_y front(MPa)	σ_y back(MPa)	σ_y average(MPa)
323	12	85.04	87.966	86.503
390	17.6875	81.618	88.446	85.032
389	23.375	54.328	71.156	62.742
388	29.0625	59.903	41.729	50.816

Table B.8: Aasweld FSM extrapolation method reference nodes outcome (ES=6mm)

Node number	Y coordinates(mm)	σ_y front(MPa)	σ_y back(MPa)	σ_y average(MPa)
205	12	83.423	73.405	78.414
254	19.58333333	78.777	57.037	67.907
253	27.16666667	66.971	35.403	51.187

Table B.9: Asweld FSM extrapolation method reference nodes outcome (ES=8mm)

Node number	Y coordinates(mm)	σ_y front(MPa)	σ_y back(MPa)	σ_y average(MPa)
120	12	80.798	57.59	69.194
143	23.375	71.477	43.903	57.69
142	34.75	52.842	25.999	39.4205

Table B.10: Asweld FSM extrapolation method reference nodes outcome (ES=12mm)

Node number	Z coordinates(mm)	Nodal force 1	Nodal force 2	Nodal force summation
622	210.55	-2601.9	0	-2601.9
649	206.5660714	-1975	-1885.2	-3860.2
648	202.5821429	-1075.3	-1660.1	-2735.4
647	198.5982143	-824.35	-1392.4	-2216.75
646	194.6142857	-493.16	-1188.7	-1681.86
645	190.6303571	-348.11	0	-348.11

Table B.11: Asweld FSM traction force based method reference nodes outcome(ES=4mm)

Node number	Z coordinates(mm)	Nodal force 1	Nodal force 2	Nodal force summation
454	210.55	-3048.7	0	-3048.7
476	205.7	-2239.9	-2168.5	-4408.4
47	5 200.85	-1116.3	-1875.3	-2991.6
474	196	-792.16	-1521.8	-2313.96
473	191.15	-400.43	0	-400.43

Table B.12: Asweld FSM traction force based method reference nodes outcome(ES=5mm)

Node number	Z coordinates(mm)	Nodal force 1	Nodal force 2	Nodal force summation
323	210.55	-3559.7	0	-3559.7
341	204.6789474	-2534.3	-2450.7	-4985
340	198.8078947	-1146.8	-2113.4	-3260.2
339	192.9368421	-714.46	0	-714.46

Table B.13: Asweld FSM traction force based method reference nodes outcome(ES=6mm)

Node number	Z coordinates(mm)	Nodal force 1	Nodal force 2	Nodal force summation
225	210.55	-4092.3	0	-4092.3
240	203.578125	-2773	-2747.1	-5520.1
239	196.60625	-1075.9	-2304.2	-3380.1
238	189.634375	-578.14	0	-578.14

Table B.14: Unweld FSM traction force based method reference nodes outcome(ES=7mm)

Node number	Z coordinates(mm)	Nodal force 1	Nodal force 2	Nodal force summation
137	210.55	-5018.5	0	-5018.5
148	201.2541667	-3270.7	-3212.6	-6483.3
147	191.9583333	-931.21	0	-931.21

Table B.15: Asweld FSM traction force based method reference nodes outcome(ES=10mm)

Node number	Z coordinates(mm)	Nodal force 1	Nodal force 2	Nodal force summation
120	210.55	-5733.4	0	-5733.4
129	199.395	-3528.7	-3649.8	-7178.5
128	188.24	-637.75	0	-637.75

Table B.16: Asweld FSM traction force based method reference nodes outcome(ES=12mm)

C

FSM solid model

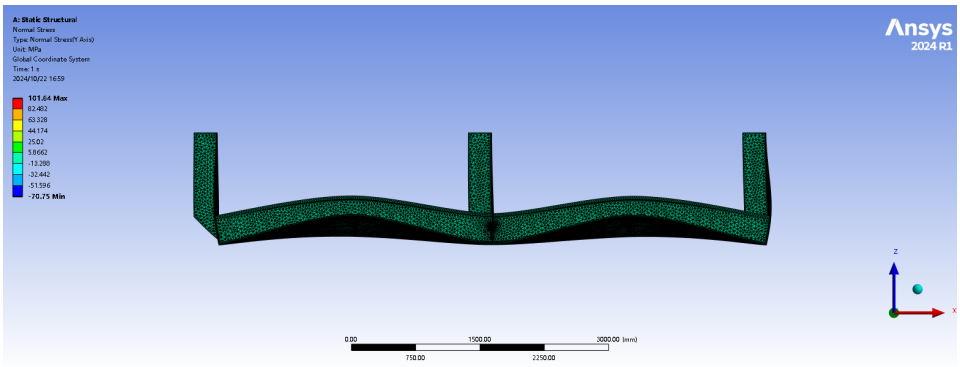

Figure C.1: FSM solid model front view

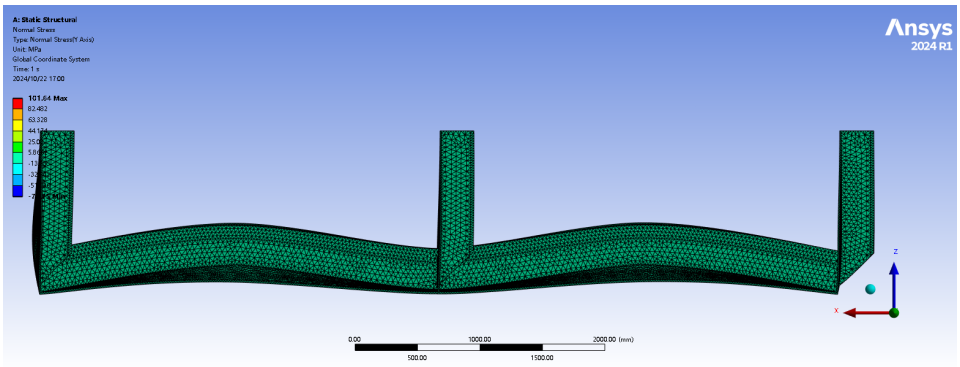

Figure C.2: FSM solid model back view

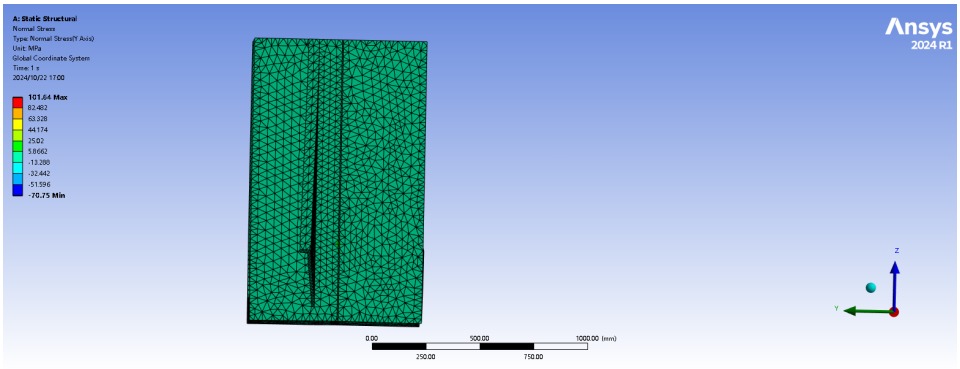

Figure C.3: FSM solid model left view

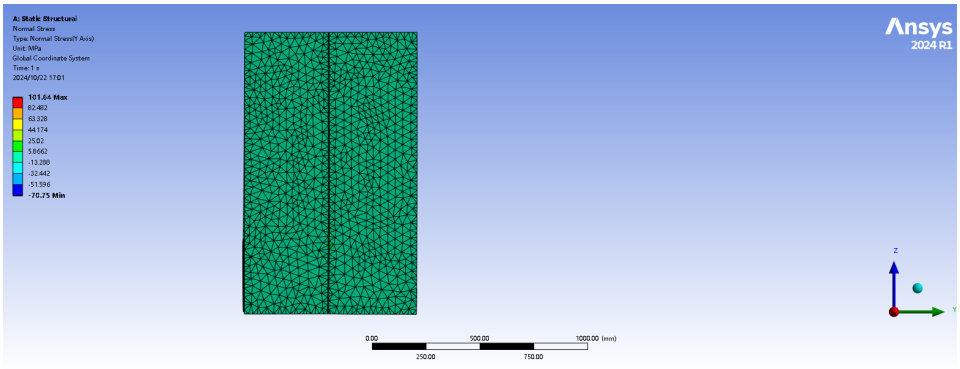

Figure C.4: FSM solid model right view

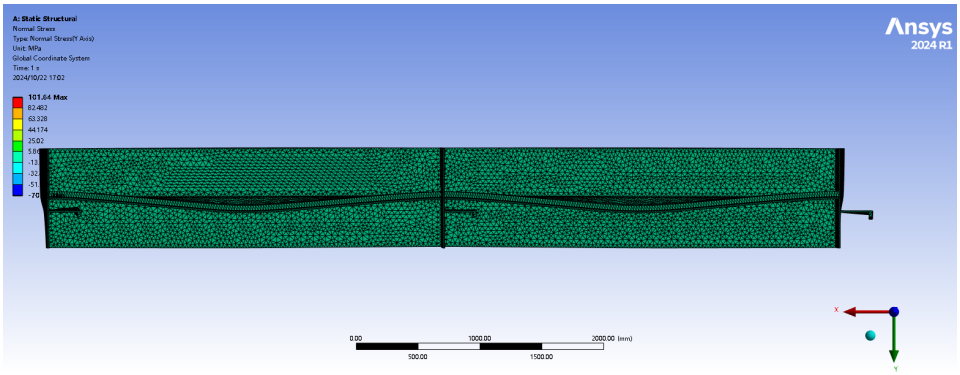

Figure C.5: FSM solid model top view

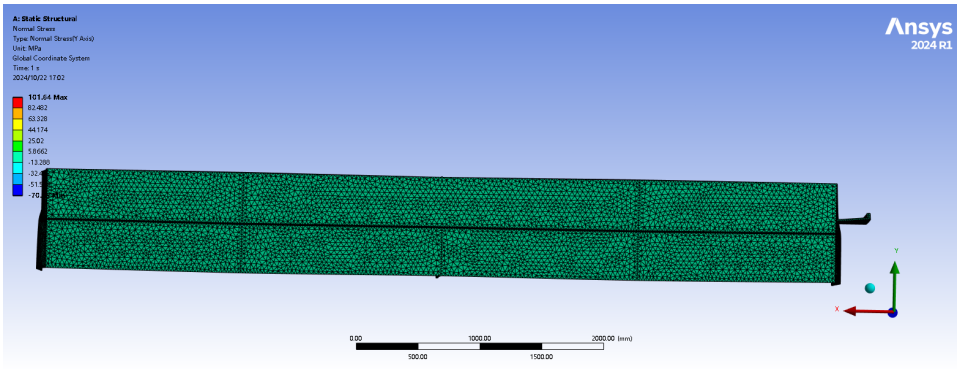

Figure C.6: FSM solid model bottom view

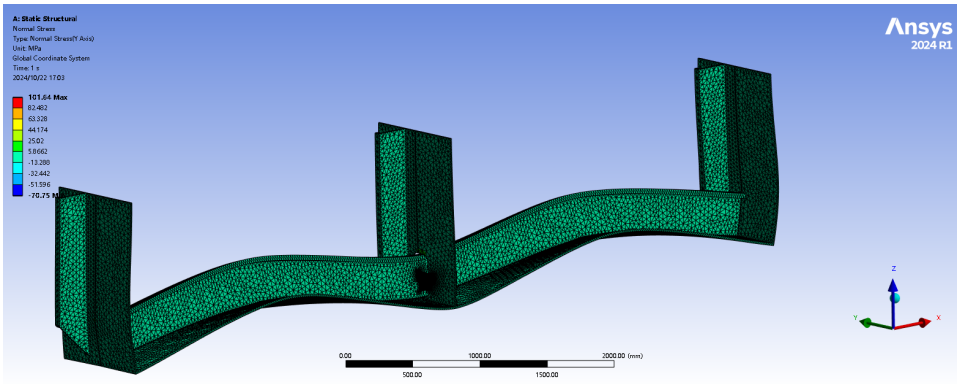

Figure C.7: FSM solid model oblique view

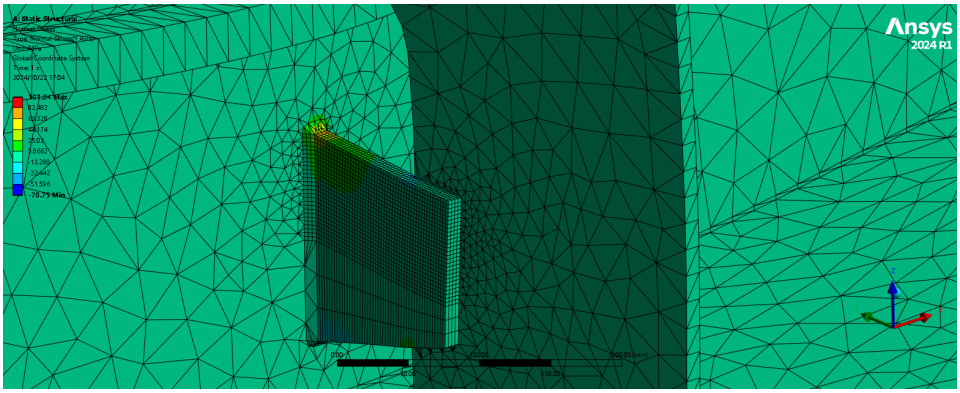

Figure C.8: FSM solid model zoom in

C.1. Reference node data output

Node number	6911	6863	6864	6865	6910
Zloc	210.55	210.55	210.55	210.55	210.55
Nfsum	237.62	375.94	344.13	341.29	221.09
Xloc	-6	-9	-12	-15	-18

Table C.1: Solid FSM reference nodes outcome(Row1)

Node Nr	6912	6860	6861	6862	6909
Zloc	207.07	207.07	207.07	207.07	207.07
Nfsum	268	324.57	294.25	322.14	251.16
Xloc	-6	-9	-12	-15	-18

Table C.2: Solid FSM reference nodes outcome(Row2)

Node Nr	6913	6857	6858	6859	6908
Zloc	203.59	203.59	203.59	203.59	203.59
Nfsum	181.19	220.33	199.58	219.03	171.48
Xloc	-6	-9	-12	-15	-18

Table C.3: Solid FSM reference nodes outcome(Row3)

Node Nr	6914	6854	6855	6856	6907
Zloc	200.12	200.12	200.12	200.12	200.12
Nfsum	149.94	173.2	157.3	168.43	134.64
Xloc	-6	-9	-12	-15	-18

Table C.4: Solid FSM reference nodes outcome(Row4)

Node Nr	6915	6851	6852	6853	6906
Zloc	196.65	196.65	196.65	196.65	196.65
Nfsum	130.2	145.99	127.43	128.94	116.28
Xloc	-6	-9	-12	-15	-18

Table C.5: Solid FSM reference nodes outcome(Row5)

Node Nr	6916	6848	6849	6950	6905
Zloc	193.17	193.17	193.17	193.17	193.17
Nfsum	33.487	25.26	20.23	22.23	27.17
Xloc	-6	-9	-12	-15	-18

Table C.6: Solid FSM reference nodes outcome(Row6)

D

SPM S1 shell model

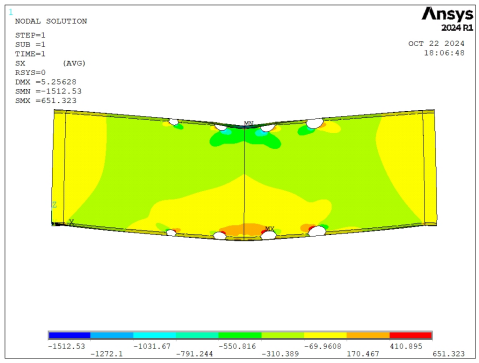

Figure D.1: SPM specimen1 shell model front view

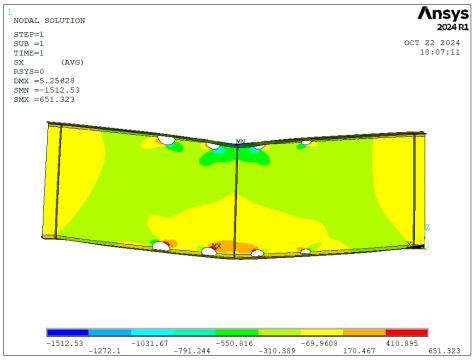

Figure D.2: SPM specimen1 shell model back view

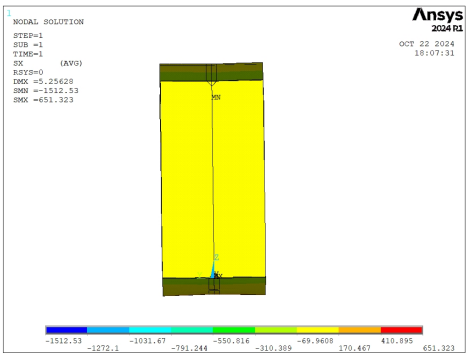

Figure D.3: SPM specimen1 shell model left view

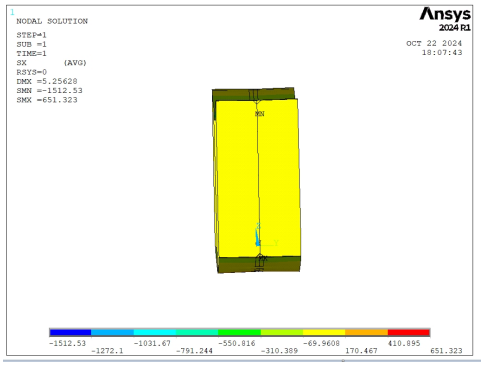

Figure D.4: SPM specimen1 shell model right view

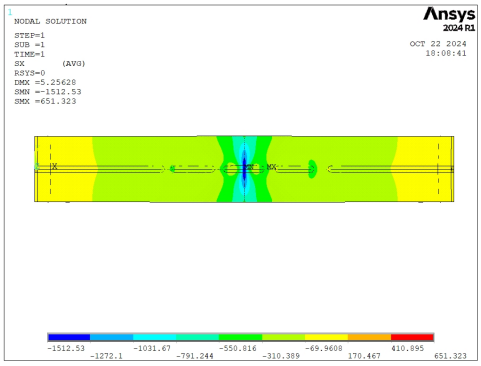

Figure D.5: SPM specimen1 shell model top view

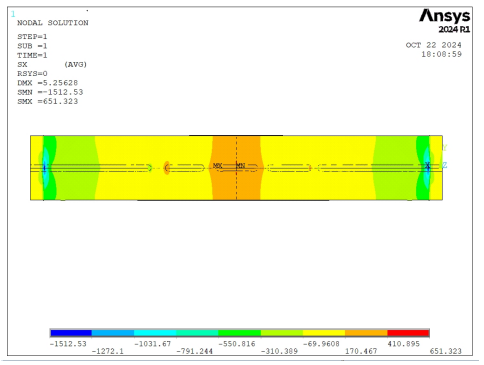

Figure D.6: SPM specimen1 shell model bottom view

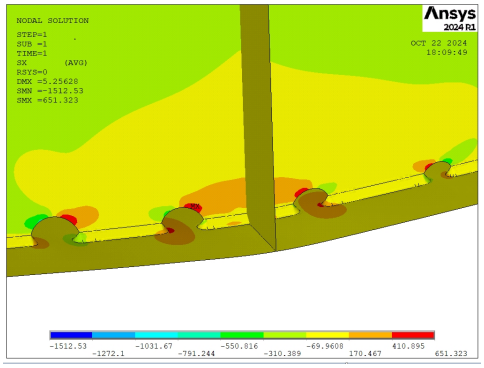

Figure D.7: SPM specimen1 A shell model zoom in

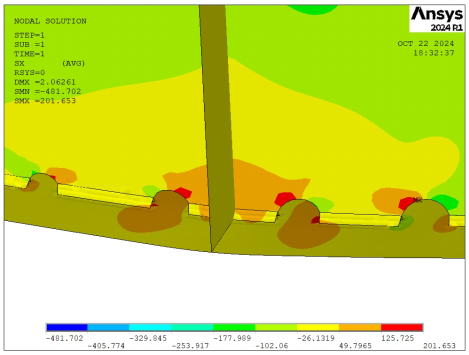

Figure D.8: SPM specimen1 B shell model zoom in

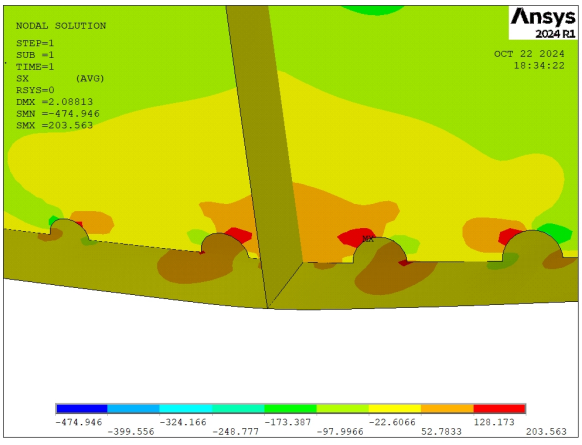

Figure D.9: SPM specimen1 unweld shell model zoom in

D.1. Reference node data output

Node number	Nodal force X	Nodal force Y	Nodal moment X	Nodal moment Y
39660	2861.25	-247.625	-927.1	962.2
39659	2818	-290	-1646	1239
39658	5431.4	-556.86	-5266.6	3095.1
39657	5295.4	-467.22	-7754.7	3614.5
39656	5090.2	-185.24	-10577.	3841.0
31518	6069.0	644.87	-14961.	6310.5
31520	7650.2	1790.9	-18934.	14711
31521	9274.0	2276.1	-18206.	27476
31522	10248.	1585.1	-12766.	41659
31519	10825.	-6.1094	-30.107	47356
31688	10273.	-1585.7	12764	41741
31687	9280.8	-2273.2	18298	27492
31686	7639.9	-1791.7	18878	14634
31685	5823.4	-637.44	14471	6120.3
44905	4689.3	134.54	9953.7	3731.0
44906	4794.4	396.44	7472.9	3242.0
44907	4979.7	516.26	5329.2	3040.4
44908	2552	260.5	1791	1239.5
44909	2610.65	244.325	1102.3	988.95

Table D.1: SPM S1A shell model r25 reference nodes outcome

Node number	Nodal force X	Nodal force Y	Nodal moment X	Nodal moment Y
45023.	2559.95	567	3679.35	1032.25
45022.	2535	635.5	4486	1628
45021.	4936.0	1329.0	10953	4028.8
45020.	4878.8	1301.4	13499	4789.2
45019.	4849.3	1090.8	16602	5543.0
32332.	7410.8	310.56	22577	8734.3
32333.	12827	-486.64	29069	17955
32334.	18854	-749.48	29592	34119
32335.	22690	-522.38	20086	51307
32120.	24109	-10.827	-99.826	58322
32123.	22607	528.12	-19964	51170
32122.	18827	790.34	-29315	34000
32121.	12968	498.49	-29327	18431
32119.	7645.8	-412.63	-23383	9021.3
40351.	5256.8	-1221.5	-17759	5679.5
40352.	5377.8	-1459.0	-14398	5110.6
40353.	5477.7	-1452.5	-11378	4159.3
40354.	2807	-676.5	-4536	1624
40355.	2814.5	584.5	-3706	1258

Table D.2: SPM S1A shell model r30 reference nodes outcome

Node number	Nodal force X	Nodal force Y	Nodal moment X	Nodal moment Y
45177	-2772	389	3152.8	-921.5
45178	-2775	464	3656	-1174
45179	-5488.5	1070.8	8717.3	-2995.7
45180	-5428.6	1211.5	10618.	-3766.6
45181	-5247.9	1264.5	13040.	-4634.8
45182	-5170.9	1199.1	16061.	-5430.6
45183	-5096.8	978.60	19476.	-6080.2
33484	-7849.3	162.57	26573.	-10102
33485	-13467.	-780.85	33733.	-21787
33486	-19337.	-1055.9	33119.	-39535
33487	-23322.	-679.00	22416.	-59236
33291	-24903.	-3.2325	-6.8398	-67183
33293	-23324.	687.96	-22394.	-59232
33294	-19353.	1038.4	-33163.	-39530
33295	-13438.	788.41	-33669.	-21669
33292	-8145.8	-227.42	-27716.	-10441
41221	-5684.8	-1103.4	-21254.	-6893.9
41220	-5727.6	-1359.5	-17036.	-5659.8
41219	-5911.7	-1397.5	-13567.	-4837.5
41218	-6070.3	-1289.5	-10789.	-3767.57
41217	-3076	-548	-4328	-1434
41216	-3076	-460.16	-3657.75	-1096.8

Table D.3: SPM S1A shell model r35 reference nodes outcome

Node number	Nodal force X	Nodal force Y	Nodal moment X	Nodal moment Y
45281	-2601.8	382	1064	-1352.5
45282	-2524	407	2026	-1681
45283	-4892.7	833.02	6634.5	-4064.8
45284	-4656.2	755.46	9609.5	-4726.7
45285	-4519.4	570.96	13034.	-5168.4
45286	-4453.6	237.17	16772.	-5343.4
34370	-5833.8	-582.67	22939.	-8998.4
34371	-8153.6	-1591.3	28775.	-21614
34372	-11006.	-2018.9	29099.	-42116
34373	-12397.	-1466.9	18345.	-58415
34152	-13131.	-4.4917	-366.43	-66040
34155	-12362.	1411.1	-18458.	-59029
34154	-10737.	2046.0	-27689.	-40382
34153	-8305.9	1664.3	-29239.	-22177
34151	-6214.1	542.67	-24363.	-9626.1
41795	-4987.2	-332.88	-18241.	-6166.7
41794	-5113.7	-702.32	-13679.	-5498.1
41793	-5326.6	-884.02	-9568.7	-5085.9
41792	-2798	-473	-2990	-2070
41791	-2901	-444	-1600.9	-1617

Table D.4: SPM S1A shell model r40 reference nodes outcome

Node Nr	5724	1	5764
Nodal force	8824	10421	3484.3
Nodal moment	26979	32439	6834.5

Table D.5: SPM S1B shell model r25 reference nodes outcome

Node Nr	5828	130	5878
Nodal force	19838	21787	9330.8
Nodal moment	28567	33320	10634

Table D.6: SPM S1B shell model r30 reference nodes outcome

Node Nr	5944	311	6012
Nodal force	-20333	-22593	9521.7
Nodal moment	-35473	-41891	12238

Table D.7: SPM S1B shell model r35 reference nodes outcome

Node Nr	6090	429	6168
Nodal force	-9956.2	-11787	4222.2
Nodal moment	-40484	-47449	10054

Table D.8: SPM S1B shell model r40 reference nodes outcome

Node Nr	5724	1	5764
Nodal force	8141	13032	3605.2
Nodal moment	21318	32664	2532.5

Table D.9: SPM S1 unweld shell model r25 reference nodes outcome

Node Nr	5828	130	5878
Nodal force	17731	22829	8827
Nodal moment	21184	31543	6768.9

Table D.10: SPM S1 unweld shell model r30 reference nodes outcome

Node Nr	5944	311	6012
Nodal force	-18274	-23907	9173.1
Nodal moment	-26675	-39458	7826.8

Table D.11: SPM S1 unweld shell model r35 reference nodes outcome

Node Nr	6090	429	6168
Nodal force	-9579.7	-14600	4584.7
Nodal moment	-32522	-46481	5054.1

Table D.12: SPM S1 unweld shell model r40 reference nodes outcome

E

SPM S1 solid model

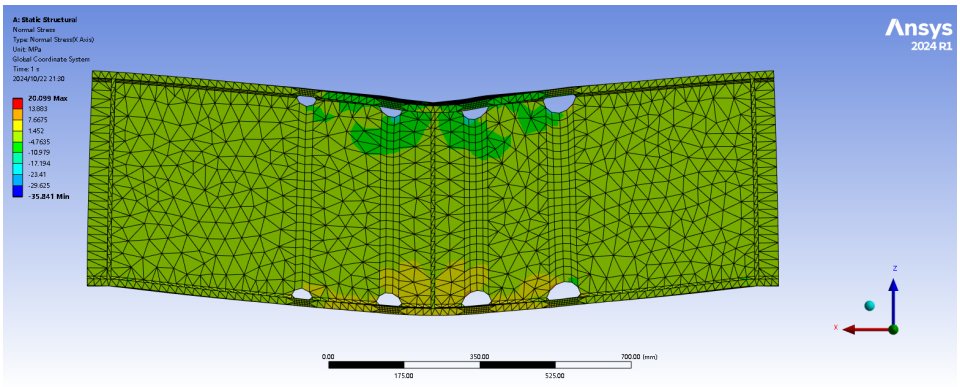

Figure E.1: SPM specimen1 solid model front view

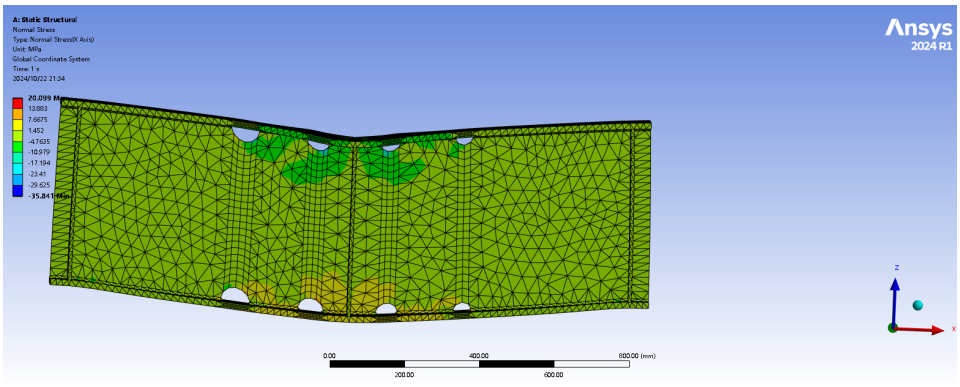

Figure E.2: SPM specimen1 solid model back view

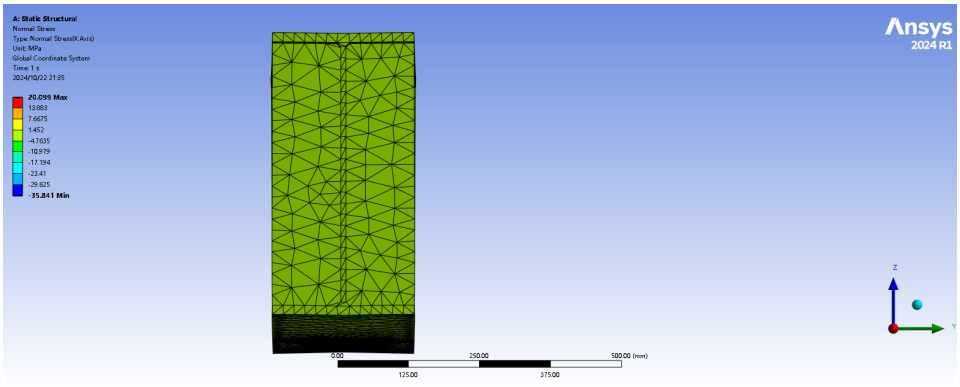

Figure E.3: SPM specimen1 solid model left view

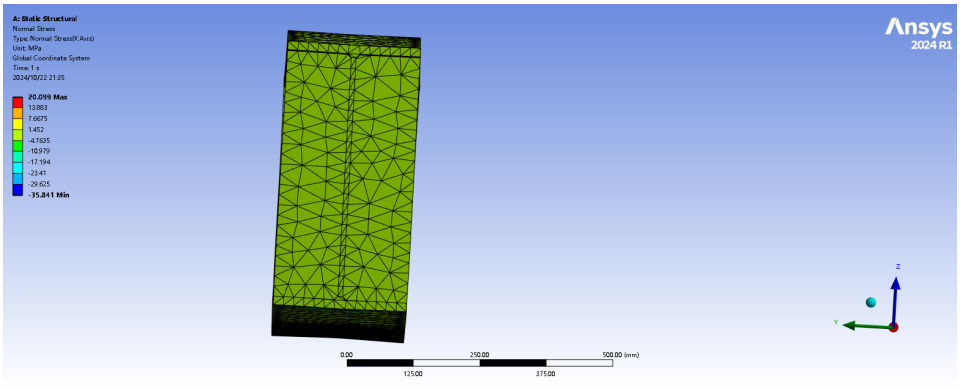

Figure E.4: SPM specimen1 solid model right view

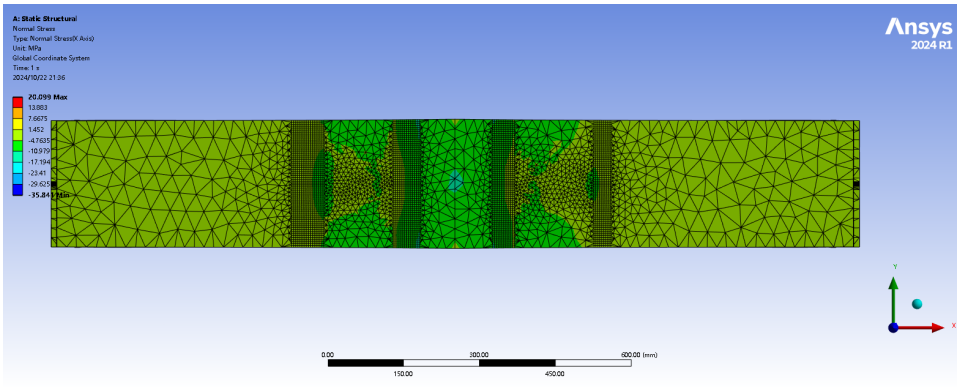

Figure E.5: SPM specimen1 solid model top view

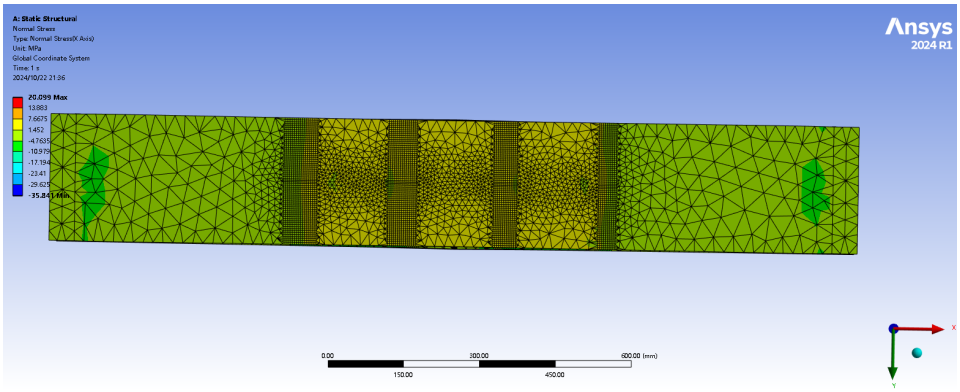

Figure E.6: SPM specimen1 solid model bottom view

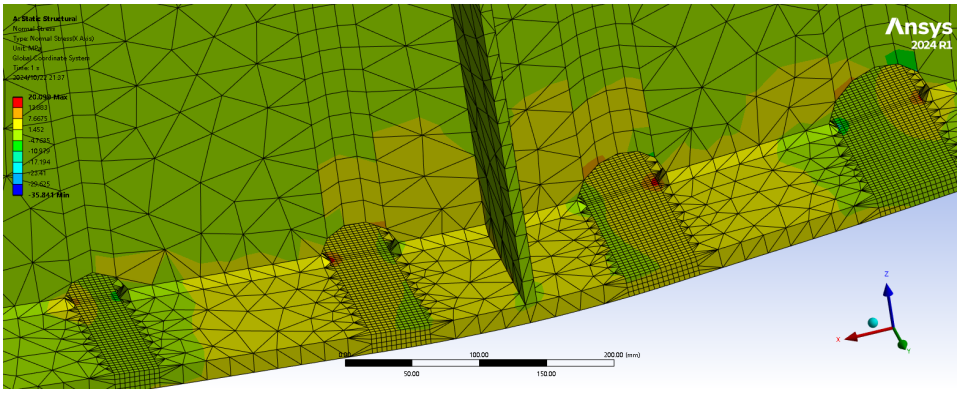

Figure E.7: SPM specimen1A solid model zoom in

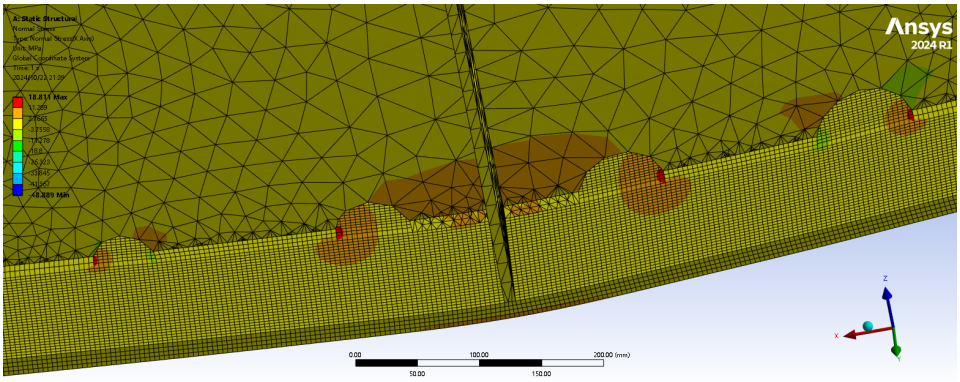

Figure E.8: SPM specimen1B solid model zoom in

E.1. Reference node data output

Node Nr	Z coordinates	Nodal force summation
20026	16	-67.447
20017	12	-54.044
20015	8	-23.143
20013	4	-2.1929
20031	0	6.1548

Table E.1: SPM S1A solid model r25 reference nodes outcome

Node Nr	Z coordinates	Nodal force summation
20130	16	-88.893
20121	12	-80.493
20119	8	-49.948
20117	4	-30.83
20135	0	-6.9501

Table E.2: SPM S1A solid model r30 reference nodes outcome

Node Nr	Z coordinates	Nodal force summation
20656	16	97.086
20644	12	86.271
20642	8	47.095
20640	4	26.284
20652	0	4.2597

Table E.3: SPM S1A solid model r35 reference nodes outcome

Node Nr	Z coordinates	Nodal force summation
20800	16	86.327
20786	12	67.417
20787	8	24.906
20788	4	-4.6032
20796	0	-14.137

Table E.4: SPM S1A solid model r40 reference nodes outcome

Node Nr	Z coordinates	Nodal force summation
114871	16	-128.32
115730	12	-87.889
115731	8	-38.866
115732	4	-9.3208
114832	0	6.6064

Table E.5: SPM S1B solid model r25 reference nodes outcome

Node Nr	Z coordinates	Nodal force summation
109549	16	-145.22
109830	12	-127.47
109831	8	-80.451
109832	4	-52.955
109504	0	-15.998

Table E.6: SPM S1B solid model r30 reference nodes outcome

Node Nr	Z coordinates	Nodal force summation
100133	16	161.02
104305	12	137.12
104306	8	82.631
104307	4	49.736
104288	0	12.339

Table E.7: SPM S1B solid model r35 reference nodes outcome

Node Nr	Z coordinates	Nodal force summation
85268	16	151.63
99621	12	105.01
99620	8	44.034
99619	4	4.2755
85268	0	-13.043

Table E.8: SPM S1B solid model r40 reference nodes outcome

F

SPM S2 shell model

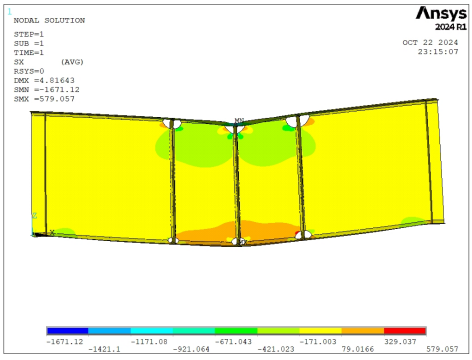

Figure F.1: SPM specimen2 shell model front view

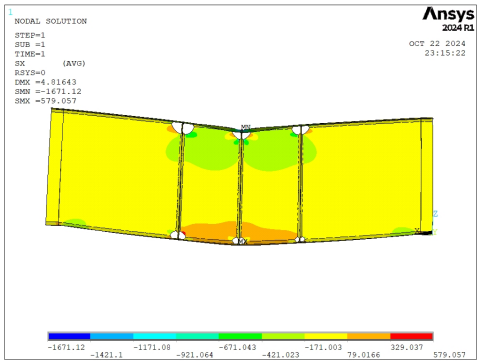

Figure F.2: SPM specimen2 shell model back view

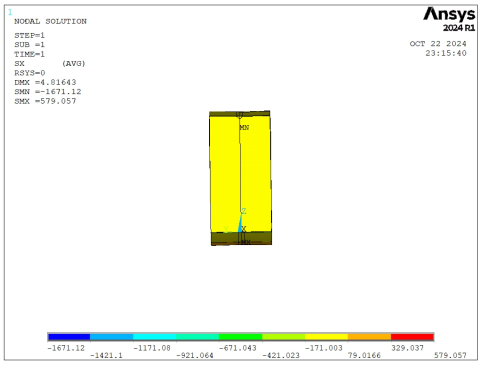

Figure F.3: SPM specimen2 shell model left view

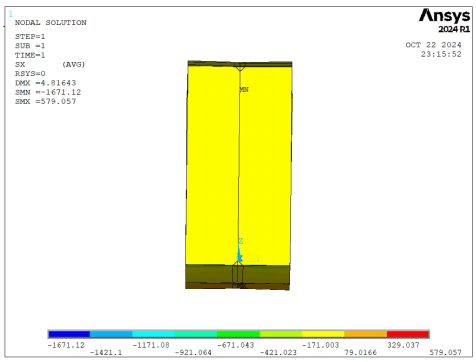

Figure F.4: SPM specimen2 shell model right view

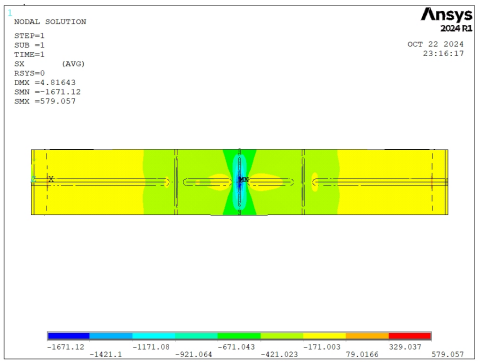

Figure F.5: SPM specimen2 shell model top view

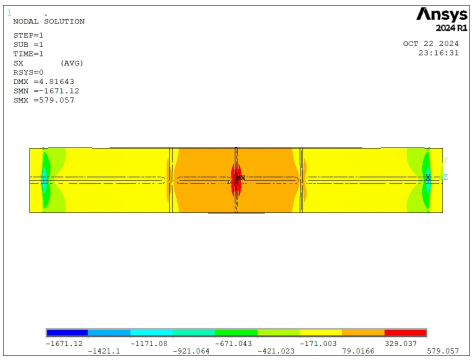

Figure F.6: SPM specimen2 shell model bottom view

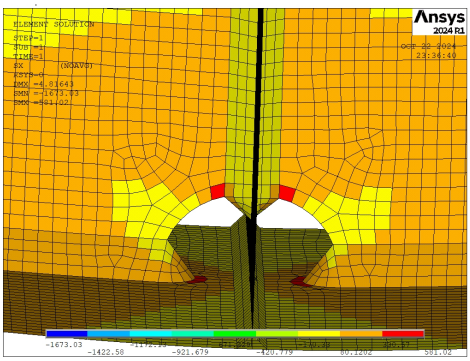

Figure F.7: SPM specimen2 A shell model zoom in

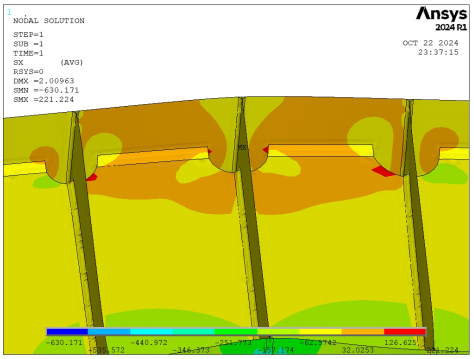

Figure F.8: SPM specimen2 B shell model zoom in

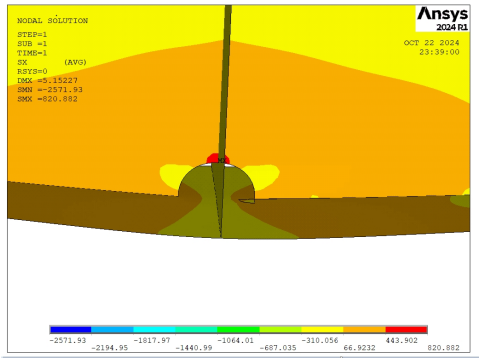

Figure F.9: SPM specimen2 unweld HS type B shell model zoom in

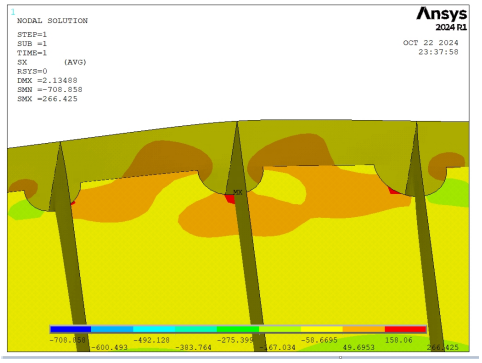

Figure F.10: SPM specimen2 unweld HS type A shell model zoom in

F.1. Reference node data output

Node number	Z coordinates(mm)	Nodal force 1	Nodal force 2	Nodal force summation
642	-28.618	-14316	0	-14316
658	-33.28909091	-4156.8	-11113	-15269.8
657	-37.96018182	1383.6	-10560	-9176.4
656	-42.63127273	919.77	0	919.77

Table F.1: SPM S1A reference nodes outcome

Node Nr	6036	373	6067
Nodal force	11386	13160	11386
Nodal moment	30343	36886	30343

Table F.2: SPM S1B r40 reference nodes outcome

Node Nr	6203	492	6244
Nodal force	23245	25305	23245
Nodal moment	24612	32234	24613

Table F.3: SPM S1B r45 reference nodes outcome

Node Nr	6506	680	6555
Nodal force	-12173	-13948	-12173
Nodal moment	-39536	-47003	-39533

Table F.4: SPM S1B r50 reference nodes outcome

Node number	Z coordinates(mm)	Nodal force 1	Nodal force 2	Nodal force summation
860	-30	-19935	0	-19935
863 -	34.54545455	-12946	-12957	-25903
864	-39.09090909	-4712.4	-10368	-15080.4
865	-48.18181818	-3251.2	0	-3251.2

Table F.5: SPM S1 unweld HSB reference nodes outcome

Node Nr	6036	373	6067
Nodal force	10956	15891	10956
Nodal moment	27795	41742	27796

Table F.6: SPM S1 unweld HSA r40 reference nodes outcome

Node Nr	6203	492	6244
Nodal force	20634	25640	20634
Nodal moment	18256	33483	18259

Table F.7: SPM S1 unweld HSA r45 reference nodes outcome

Node Nr	6506	680	6555
Nodal force	-11606	-16695	-11606
Nodal moment	-35283	-50625	-35280

Table F.8: SPM S1 unweld HSA r50 reference nodes outcome

G

SPM S2 solid model

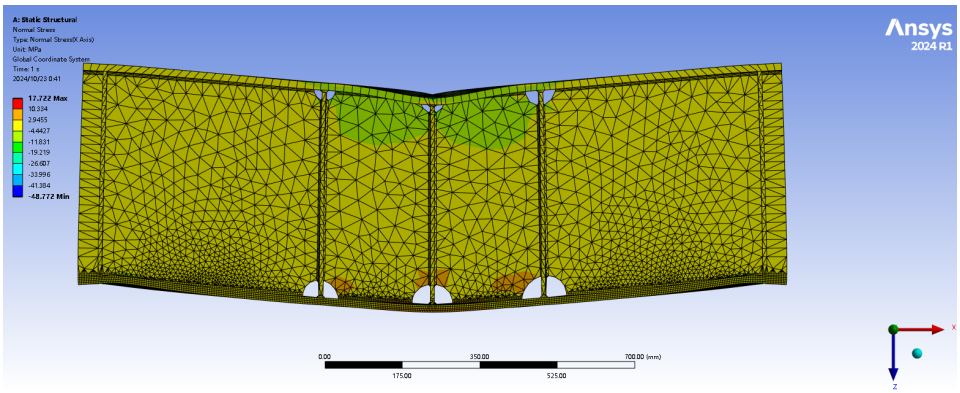

Figure G.1: SPM specimen2 solid model front view

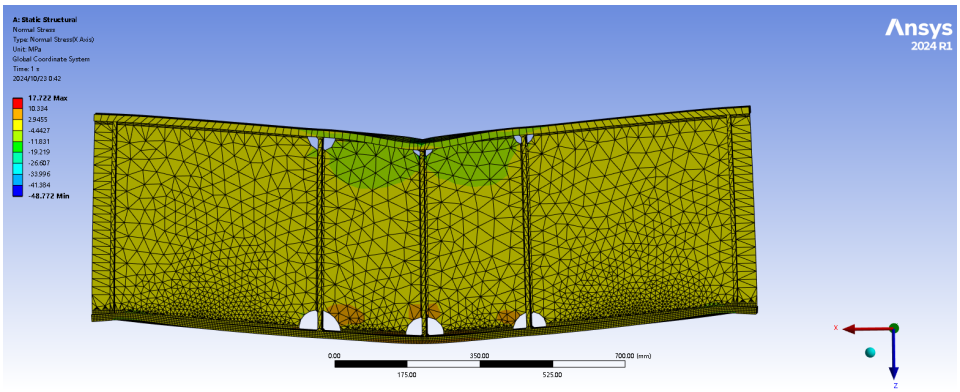

Figure G.2: SPM specimen2 solid model back view

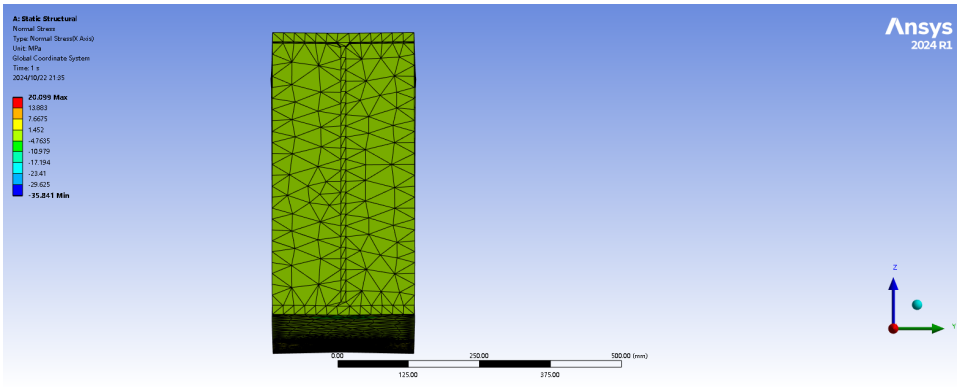

Figure G.3: SPM specimen2 solid model left view

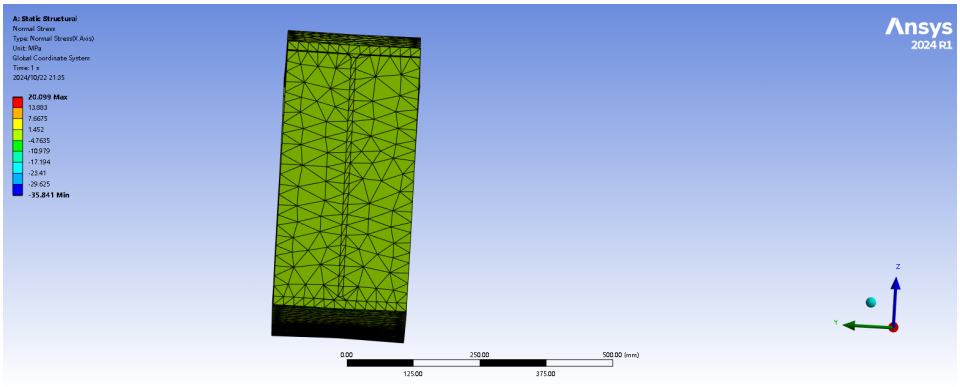

Figure G.4: SPM specimen2 solid model right view

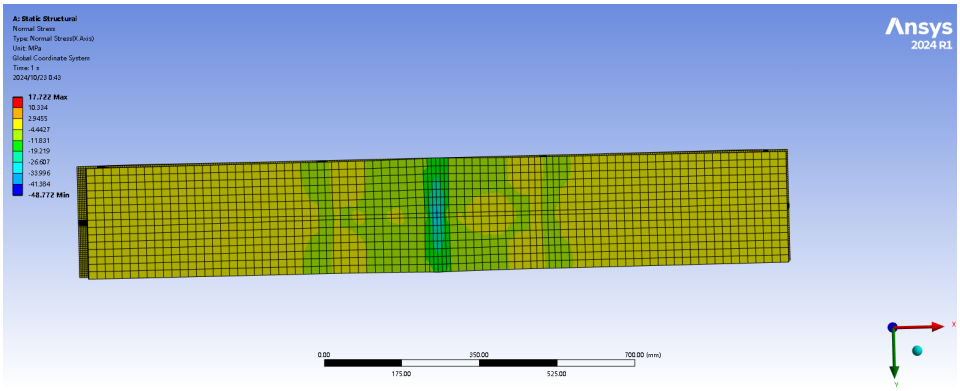

Figure G.5: SPM specimen2 solid model top view

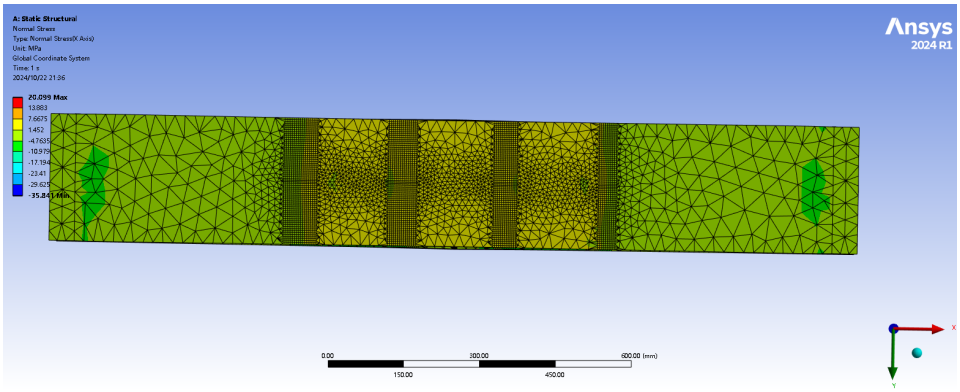

Figure G.6: SPM specimen2 solid model bottom view

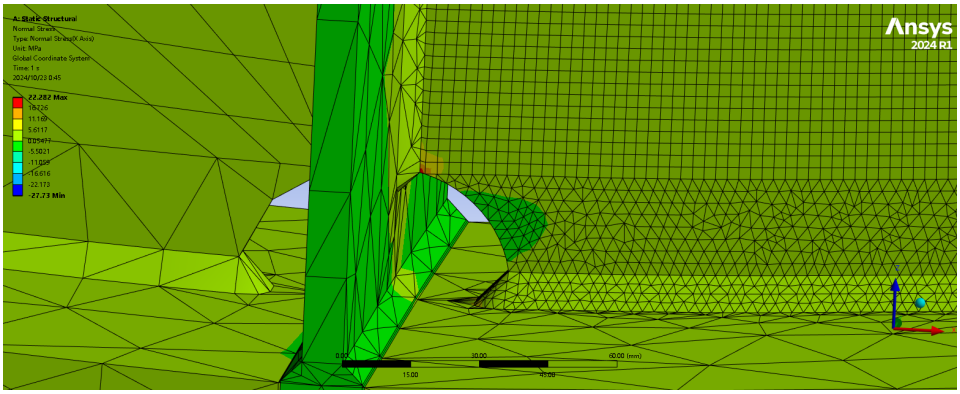

Figure G.7: SPM specimen2A solid model zoom in

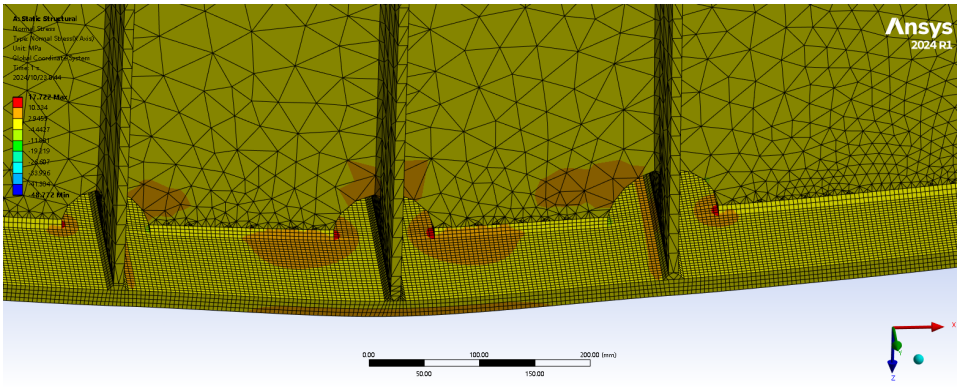

Figure G.8: SPM specimen2B solid model zoom in

G.1. Reference node data output

Node Nr	42663	51962	51963	51965	51964
Zloc	36.61817604	36.61817604	36.61817604	36.61817604	36.61817604
Nfsum	28.782	47.576	50.307	47.614	28.306
Yloc	-4.5	-2.25	0	2.25	4.5

Table G.1: Solid SPM S2A reference nodes outcome(Row1)

Node Nr	42664	51882	51901	51920	51939
Zloc	39.20526724	39.20526724	39.20526724	39.20526724	39.20526724
Nfsum	24.46	33.603	35.247	36.037	25.35
Yloc	-4.5	-2.25	0	2.25	4.5

Table G.2: Solid SPM S2A reference nodes outcome(Row2)

Node Nr	42665	51883	51902	51921	51940
Zloc	41.79235844	41.79235844	41.79235844	41.79235844	41.79235844
Nfsum	16.212	22.602	21.834	24.561	16.633
Yloc	-4.5	-2.25	0	2.25	4.5

Table G.3: Solid SPM S2A reference nodes outcome(Row3)

Node Nr	42666	51884	51903	51922	51941
Zloc	44.37944964	44.37944964	44.37944964	44.37944964	44.37944964
Nfsum	14.462	19.784	19.056	21.84	14.62
Yloc	-4.5	-2.25	0	2.25	4.5

Table G.4: Solid SPM S2A reference nodes outcome(Row4)

Node Nr	42667	51885	51904	51923	51942
Zloc	46.96654083	46.96654083	46.96654083	46.96654083	46.96654083
Nfsum	3.5707	4.6627	4.35	4.8723	3.8068
yloc	-4.5	-2.25	0	2.25	4.5

Table G.5: Solid SPM S2A reference nodes outcome(Row5)

Node Nr	Z coordinates	Nodal force summation
92675	16	133.66
92721	12	93.689
92722	8	45.86
92723	4	17.366
92720	0	-2.6519

Table G.6: SPM S2B solid model r40 reference nodes outcome

Node Nr	Z coordinates	Nodal force summation
88165	16	150.5
88167	12	133.93
88168	8	91.168
88169	4	68.502
88126	0	24.865

Table G.7: SPM S2B solid model r45l reference nodes outcome

Node Nr	Z coordinates	Nodal force summation
84069	16	-156.54
88075	12	-136.97
88074	8	-91.785
88073	4	-67.117
88064	0	-23.366

Table G.8: SPM S2B solid model r45r reference nodes outcome

Node Nr	Z coordinates	Nodal force summation
76017	16	-152.69
83805	12	-106.93
83804	8	-48.931
83803	4	-11.699
74639	0	8.7739

Table G.9: SPM S2B solid model r50 reference nodes outcome